

Stony Brook University



OFFICIAL COPY

The official electronic file of this thesis or dissertation is maintained by the University Libraries on behalf of The Graduate School at Stony Brook University.

© All Rights Reserved by Author.

Radiolabelling and Pharmacokinetics of Antibacterial Agents Using Positron

Emission Tomography

A Dissertation Presented

by

Hui Wang

to

The Graduate School

in Partial Fulfillment of the

Requirements

for the Degree of

Doctor of Philosophy

in

Chemistry

Stony Brook University

May 2015

Stony Brook University
The Graduate School

Hui Wang

We, the dissertation committee for the above candidate for the
Doctor of Philosophy degree, hereby recommend
acceptance of this dissertation.

Peter J. Tonge – Dissertation Advisor
Professor, Department of Chemistry

Francis Johnson – Chairperson of Defense
Professor, Department of Chemistry

Isaac Carrico – Third Committee Member of Defense
Associate Professor, Department of Chemistry

Peter M. Smith-Jones – Outside Committee Member of Defense
Professor, Department of Psychiatry, Stony Brook University

This dissertation is accepted by the Graduate School

Charles Taber
Dean of the Graduate School

Abstract of the Dissertation

Radiolabelling and Pharmacokinetics of Antibacterial Agents Using Positron Emission

Tomography

by

Hui Wang

Doctor of Philosophy

in

Chemistry

Stony Brook University

2015

Target tissue pharmacokinetics (PK) is the link between plasma PK and pharmacodynamic (PD) effects. Tissue PK can be determined noninvasively using positron emission tomography (PET), which images molecules labelled with positron emitting isotopes and is an important tool for studying drug action in animals and humans. In applying this technology to infectious diseases, we have synthesized several antibacterial agents and determined their biodistribution in models of *Staphylococcus aureus* and *Mycobacterium tuberculosis* infection. Not only do these studies inform PK-PD relationships, but they also serve as the first steps in developing novel tracers for imaging bacterial infection *in vivo*.

PT119 is a potent long residence time inhibitor of the *Staphylococcus aureus* enoyl-ACP reductase with antibacterial activity (PD) in two *S. aureus* infection models. To correlate the observed PD with plasma PK, PT119 was radiolabeled with carbon-11 to evaluate its

biodistribution and PK in both healthy and *S. aureus* infected mice using PET. The biodistribution of [^{11}C]PT119 and/or its labeled metabolites did not differ significantly between the healthy group and the infected group, and PT119 was found to distribute equally between serum and tissue during the ~1 h of analysis permitted by the carbon-11 half life. These data suggest that the *in vivo* efficacy of PT119 is not due to accumulation of the drug at the site of infection and supports the importance of drug-target residence time in this system.

Pyrazinamide (PZA) is a first-line tuberculosis drug whose mechanism of action still remains to be fully elucidated. To explore the biodistribution of this important drug, PZA was labeled with fluorine-18 and 5- ^{18}F fluoropyrazinamide (5- ^{18}F]PZA) was imaged in *M. tuberculosis* infected mice using PET. The imaging was rapid, noninvasive, and simultaneously allowed multiple tissues to be visualized simultaneously. Compared to uninfected animals, *M. tuberculosis*-infected mice had a higher PET signals within the lungs (ratio: 1.6:1). The results indicate that the accumulation of the probe in infected lungs, due to pathogen-specific metabolism, contributes to the *in vivo* efficacy of PZA, and suggests that 5- ^{18}F]PZA may be able to monitor pathogen burden in infected patients.

Furthermore, *para*-amino benzoic acid (PABA) from tetrahydrofolate (THF) biosynthesis pathway has been proposed as a promising candidate to detect bacterial infection *in vivo*, due to its ability to accumulate selectively in bacterial cells over mammalian cells. A three-step radiolabelling strategy for 2- ^{18}F]PABA has been successfully developed.

Table of Contents

Chapter 1 Introduction: Positron Emission Tomography and Its Applications in Diagnosis of Infectious Diseases and Drug Development	1
Overview	1
Principles of PET	1
The contribution of PET in the diagnosis of infectious diseases	4
Role of ¹⁸ F-FDG-PET for the diagnosis of infectious diseases.....	7
Other radiolabeled compounds for the diagnosis of infectious and inflammatory diseases .	14
The role of PET in drug discovery & development	20
Drug tissue distribution	21
Determine target engagement using PET	25
Production and incorporation of radionuclides	26
Radiolabelling with carbon-11	27
Radiolabelling with fluorine-18	29
Summary	31
Chapter 2 Radiolabelling and Biological Evaluation of Time-Dependent Diaryl Ether Inhibitors of InhA, the Enoyl-ACP Reductase from <i>Mycobacterium tuberculosis</i>	32
Background	32
Results and Discussion.....	37
Organic Synthesis	37
Radiosynthesis of [¹¹ C]PT70.....	39
Radiosynthesis of [¹⁸ F]PT161	40
Alternative strategy for radiolabelling diaryl ethers with fluorine-18.....	42
Biodistribution of [¹¹ C]PT70 in mice	43
Pharmacokinetics (PK) of PT70	44
PET imaging of [¹¹ C]PT70 in baboon	46
Materials and Methods	49
Organic Synthesis	49
Radiosynthesis of [¹¹ C]PT70.....	54

Radiosynthesis of [¹⁸ F]PT161	54
Pharmacokinetics of PT70.....	55
Conclusions	56
Chapter 3 Radiosynthesis, Pharmacokinetics and Pharmacodynamics of a Novel Enoyl-ACP Inhibitor in <i>Staphylococcus aureus</i>-infected Mice	57
Introduction	57
Materials and Methods	61
General.....	61
Chemistry.....	62
Radiosynthesis of [¹¹ C]-PT119.....	63
Uptake of [¹¹ C]PT119 in <i>S. aureus</i> cells	64
Infection models	64
In vivo antibacterial efficacy of PT119	65
PK of PT119	66
Biodistribution of [¹¹ C]-PT119.....	67
Results	68
Radiosynthesis of [¹¹ C]PT119.....	68
Uptake of [¹¹ C]PT119 in <i>S. aureus</i> cells	68
Validation of <i>S. aureus</i> thigh infection model for PET imaging.....	70
Biodistribution of [¹¹ C]PT119 in thigh infected mice	72
Biodistribution of [¹¹ C]PT119 in systemic infected and healthy mice.....	74
PT119 has efficacy in the <i>S. aureus</i> infected mice.....	75
PK and subcutaneous bioavailability of PT119.....	78
Discussion	81
Conclusions	84
Acknowledgement.....	85
Chapter 4 Noninvasive Imaging of 5-[¹⁸F]-Pyrazinamide in <i>Mycobacterium tuberculosis</i>-infected Mice Using Positron Emission Tomography.....	86
Introduction	86

Results	90
Chemistry.....	90
Characterization of 5-F-PZA.....	91
Radiochemistry	94
PET Imaging.....	95
Organ compartment pharmacokinetics of 5-[¹⁸ F]-PZA.....	97
<i>Ex vivo</i> biodistribution.....	98
Microsomal Stability Assay.....	99
Discussions.....	101
Conclusions	104
Experimental Section	105
Synthesis of Reference 5-Fluoropyrazinamide (2).....	105
PZase assay.....	105
Radiosynthesis of 5-[¹⁸ F]F-pyrazinamide (3).....	106
Microsomal Stability Assay.....	107
Animal Experiment.....	108
Chapter 5 Synthesis, Characterization, and Radiolabelling of 2-(¹⁸F)fluoro-4-aminobenzoic acid ([¹⁸F]-PABA) for PET imaging	111
Introduction	111
Methods and Materials	115
Chemistry.....	115
Radiochemistry	123
MIC screen	127
Results and Discussions	128
Chemistry.....	128
Radiochemistry	130
MIC screen result.....	131
Conclusion.....	134
Bibliography	135

List of Figures

Figure 1. 1 Schematic representation of the principles behind PET.....	4
Figure 1. 2 ¹⁸ F-FDG-PET and MRI images of a patient with diabetic foot and suspected bone infection.....	9
Figure 1. 3 Proposed structured diagnostic protocol for ¹⁸ F-FDG-PET/CT in patients presenting with fever of unknown origin (FOV).....	11
Figure 1. 4 PET/CT images of ¹⁸ F-FDS in <i>E. coli</i> myositis mice model.....	15
Figure 1. 5 The links between serum pharmacokinetics and drug effect.....	21
Figure 1. 6 Peripheral organ distribution of [¹⁸ F]-travafloxacin determined by PET in a healthy male volunteer.....	23
Figure 1. 7 MALDI-MS images of moxifloxacin distributions in the tuberculosis infected rabbit lung biopsy.....	24
Figure 1. 8 Measuring target engagement in humans using PET.	26
Figure 1. 9 Important ¹¹ C precursors used in syntheses that are made from [¹¹ C]CO ₂ and [¹¹ C]CH ₄	27
Figure 1. 10 Examples of important PET tracers labeled with carbon-11 and fluorine-18.....	30
Figure 2. 1 Structures of the diaryl ether scaffold, PT70, and PT161.	34
Figure 2. 2 Biodistribution of [¹¹ C]PT70 in healthy mice.	44
Figure 2. 3 <i>In vivo</i> Pharmacokinetics parameters for PT70.....	45
Figure 2. 4 PET imaging of [¹¹ C]PT70 in baboon.....	47
Figure 3. 1a Fatty acid biosynthesis pathway in <i>S. aureus</i>	59
Figure 3. 2 [¹¹ C]PT119 and [¹⁸ F]FDG uptake of <i>S. aureus</i> cells, experimental group (blue) and competition group (red).	69
Figure 3. 3 [¹⁸ F]FDG imaging of <i>S. aureus</i> thigh infection model (slice, not projection, summed from 0-120 min).....	71
Figure 3. 4 Quantitative analysis of T/NT ratio (infected/uninfected) for [¹⁸ F]FDG in <i>S. aureus</i> thigh infected model.	71
Figure 3. 5 Biodistribution of [¹¹ C]PT119 in <i>S. aureus</i> thigh infection model.	73
Figure 3. 6 Biodistribution of [¹¹ C]PT119 in <i>S. aureus</i> systemic infection model.....	75
Figure 3. 7 <i>In vivo</i> efficacy of PT119 in two different models.....	77
Figure 3. 8 Bioavailability and <i>in vivo</i> pharmacokinetics of PT119.....	80
Figure 4. 1 Wayne's Modified Pyrazinamidase Assay.....	93
Figure 4. 2 Analytical and semi-preparation HPLC chromatography of 5- ¹⁸ F]fluoropyrazinamide.	95
Figure 4. 3 5- ¹⁸ F]-PZA in <i>M. tuberculosis</i> infected mouse 30 min post injection. Images were slices from mice at 30 min, not summed images.....	96
Figure 4. 4 [¹⁸ F]NaF in <i>M. tuberculosis</i> infected mouse 30 min post-injection. Images were slices from mice at 30 min, not summed images.....	97

Figure 4. 5 Lung compartment pharmacokinetics of 5-[¹⁸ F]-PZA.	98
Figure 4. 6 <i>Ex vivo</i> tissue biodistribution of 5-[¹⁸ F]-PZA in <i>M. tuberculosis</i> infected and uninfected mice.	99
Figure 4. 7 Metabolic stability of 5-F-PZA in mouse liver microsomes.	100
Figure 5. 1 Structures of PABA, PAS, and 2-F-PABA	113
Figure 5. 2 PAS is an alternative substrate for DHPS and the product analog inhibits DHFR. Reproduced from (246).	114
Figure 5. 3 Radio TLC result for formation of intermediate 11.	125
Figure 5. 4 Radio TLC result for formation of intermediate 12.	126
Figure 5. 5 Two analytical HPLC system, each shows the formation of final product 2-[¹⁸ F]-PABA with different retention time.	130

List of Tables

Table 1. 1 Physical properties of the most commonly used short-lived radionuclides.....	2
Table 1. 2 Summary of radiolabeled compounds for infection/inflammation imaging.....	19
Table 2. 1 Reaction condition screening using compound 10 as precursor.....	41
Table 2. 2 Biodistribution of [¹¹ C]PT70 in healthy mice.....	43
Table 2. 3 <i>In vivo</i> Pharmacokinetics parameters for PT70	46
Table 3. 1 Quantitative analysis of T/NT ratio for [¹⁸ F]FDG in <i>S. aureus</i> thigh infected model.	72
Table 3. 2 Biodistribution in thigh infection model.....	73
Table 3. 3 Biodistribution in systemic infection model	74
Table 3. 4 <i>In vivo</i> pharmacokinetic parameters for PT119 delivered iv and sc.....	79
Table 4. 1 Metabolic stability of 5-F-PZA in mouse liver microsomes.	100
Table 5. 1 Comparison of trapping efficiency for intermediate 12 using two different solid-phase extraction products.....	131
Table 5. 2 MIC screen results for PABA, PAS, and 2-F-PABA	133

List of Schemes

Scheme 2. 1 Formation of INH-NAD adduct.	33
Scheme 2. 2 Kinetic scheme for time dependent inhibition.	35
Scheme 2. 3 Synthesis of precursor for [¹¹ C]PT70.....	38
Scheme 2. 4 Synthesis of precursor for [¹⁸ F]PT161	38
Scheme 2. 5 Radiosynthesis of [¹¹ C]PT70.....	39
Scheme 2. 7 Proposed scheme for radiolabelling dirayl ether compounds with click ¹⁸ F-fluorination strategy	42
Scheme 3. 1 Synthesis of reference PT119.....	62
Scheme 3. 2 Radiosynthesis of [¹¹ C]PT119.....	63
Scheme 4. 1 Original proposed 2-step synthesis route for 5-F-PZA	90
Scheme 4. 2 Synthesis of 5-F-PZA.....	91
Scheme 4. 3 Radiosynthesis of 5-[¹⁸ F]-PZA.....	94
Scheme 5. 1 Synthesis of 2-F-PABA from 2, 4-dinitrobenzotrile.....	115
Scheme 5. 2 Synthesis of 2-F-PABA from 2, 4-dinitrobenzaldehyde.....	118
Scheme 5. 3 Synthesis of 2-F-PABA from 2, 4-dinitrobenzoic acid.....	120
Scheme 5. 4 Radiosynthesis of 2-[¹⁸ F]-PABA	124

List of Abbreviations

% ID/cc	% of injected dose per cubic centimeter
2-F-PABA	2-fluoro- <i>para</i> -amino-benzoic acid
5-F-PZA	5-fluoro-pyrazinamide
5-Cl-PZA	5-chloro-pyrazinamide
ACP	Acyl carrier protein
AUC	Area under curve
BBB	Blood-brain barrier
Calcd	Calculated
CFU	Colony forming unit
CT	X-ray computed tomography
CIED	Cardiovascular implantable electronic devices
CDC	U.S. Centers for Disease Control and Prevention
CNS	Central nervous system
DCY	Decay-corrected yield
DMSO	Dimethyl sulfoxide
DCM	Dichloromethane
DMF	Dimethylformamide
EMB	Ethambutol
EI	Enzyme-inhibitor complex
EOB	End of bombardment
EtOH	Ethanol

<i>E. coli</i>	<i>Escherichia coli</i>
FOV	Fever of unknown origin
FDA	Food and Drug Administration
FDG	2-[¹⁸ F]-fluorodeoxy-D-glucose
FDS	¹⁸ F-fluorodeoxysorbitol
FAS	Fatty acid biosynthesis pathway
HIV	Human immunodeficiency virus
HPLC	High performance liquid chromatography
HNP	Human neutrophil peptide
HCl	Hydrochloric acid
InhA	Enoyl-ACP reductase from <i>M. tuberculosis</i>
INH	Isoniazid
KatG	Mycobacterial catalase-peroxidase
KOH	Potassium hydroxide
<i>M. tuberculosis</i>	<i>Mycobacterium tuberculosis</i>
MDR	Multidrug resistance
MIC	Minimum inhibitory concentration
MHz	Megahertz
MS	Mass spectrum
MRI	Magnetic resonance imaging
MALDI	Matrix-assisted laser desorption/ionization
MSI	Mass spectrometric imaging
MRSA	Methicillin-resistant <i>S. aureus</i>

NAD ⁺	Nicotinamide adenine dinucleotide (oxidized form)
NADH	Nicotinamide adenine dinucleotide (reduced form)
NaOH	Sodium hydroxide
NAM	Nicotinamide
NMR	Nuclear magnetic resonance
N.D.	Not determined
PET	Positron emission tomography
PK	Pharmacokinetics
PD	Pharmacodynamics
PABA	<i>Para</i> -amino benzoic acid
PAS	<i>Para</i> -amino salicylic acid
PZA	Pyrazinamide
POA	Pyrazinoic acid
PZase	Mycobacterial pyrazinamidase
PVE	Prosthetic valve endocarditis
RBF	Round bottom flask
RIF	Rifampicin
RT	Room temperature
<i>S. aureus</i>	<i>Staphylococcus aureus</i>
SPECT	Single photon emission computed tomography
SUV	Standardized uptake values
THF	Tetrahydrofuran
TLC	Thin layer chromatography

TB	Tuberculosis
UBI	Ubiquicidin
VRSA	Vancomycin-resistant <i>S. aureus</i>
WHO	World health organization
XDR	Extensively drug resistant

Acknowledgments

I would like to express my most sincere gratitude to my advisor, Prof. Peter J. Tonge, for his continuous guidance, support, and encouragement for the past few years. It is fortunate for me to have the opportunity to conduct my PhD research in Prof. Tonge's research group, and on such an exciting project. This dissertation would not be possible without his enthusiasm, patience, support, and guidance.

I would also like to thank Prof. Francis Johnson, the chairperson of my dissertation committee, for his knowledgeable advice and kind help in guiding my research. I am grateful to Prof. Isaac Carrico, the third member of my dissertation committee, for his insightful advice. It is my great pleasure to thank Prof. Peter M. Smith-Jones, the outside member of my dissertation committee, for sharing his expertise and resources with me over the past year. In addition, I would like to thank Prof. Joanna Fowler, Prof. Jacob Hooker, and Prof. Sanjay Jain, as well as their teams, for all the productive collaborations.

I want to thank all the current members and alumni members of Tonge group, for all your stimulating discussions, generous help, and heartwarming friendship. I also want to thank my other friends especially my roommates here in Stony Brook, for brightening my life.

Finally, I want to thank my family members. Their precious and unconditional love has brought me this far, and will keep me motivated and happy for the rest of my life.

List of Publications

- **Wang, H.**; Lu, Y.; Liu, L.; Alexoff, D.; Kim, S. W.; Hooker, M. J.; Fowler, J. S., and Tonge, P. J. “Radiosynthesis of Novel Enoyl-ACP Reductase Inhibitor for Pharmacokinetics Determination in *Staphylococcus aureus* Infected Mice Using PET”. *Eur. J. Med. Chem.* 2014, 88(17), 66-73.
- **Wang, H.**; Liu, L.; Lu, Y.; Pan, P.; Hooker, M. J.; Fowler, J. S., and Tonge, P. J. “Radiolabelling and Biological Evaluation of a Time-Dependent Diaryl Ether Inhibitor of InhA, the Enoyl-ACP Reductase from *Mycobacterium tuberculosis*”. *Bioorg. Med. Chem. Letter.* 2015. (*in preparation*).
- Weinstein, E. A.; Liu, L.; Ordonez, A. A.; **Wang, H.**; Hooker, J. M.; Tonge, P. J., and Jain, S. K. “Noninvasive Determination of 2-[¹⁸F]-Fluoroisonicotinicacid Hydrazide Pharmacokinetics by Imaging *Mycobacterium tuberculosis* Infected Mice.” *Antimicrob. Agents Chemother.* 2012, 56(12), 6284.
- DeMarco, V. P.; Ordonez, A. A.; Klunk, M. W.; Holt, D. P.; Weinstein, E. A.; Tonge, P. J.; **Wang, H.**; Zhang, Z.; Lee, C. K.; Dooley, K. and Jain, S. K. “Multi-compartment Pharmacokinetics of 11C-Rifampin in Mice infected with *Mycobacterium tuberculosis* Using Dynamic Positron Emission Tomography”. 2015. (*in preparation*).
- Cummings, J. E.; Beaupre, A. J.; Knudson, S. E.; Liu, N.; Yu, W.; Neckles, C.; **Wang, H.**; Khanna, A.; Bommineni, G. R.; Trunck, L. A.; Schweizer, H. P.; Tonge, P. J. and Slayden, R. A. “Substituted Diphenyl Ethers as a Novel Chemotherapeutic Platform against *Burkholderia pseudomallei*”. *Antimicrob Agents Chemother.* 2014;58(3):1646-51.

Chapter 1 Introduction: Positron Emission Tomography and Its Applications in Diagnosis of Infectious Diseases and Drug Development

Overview

Positron Emission Tomography (PET) is a non-invasive molecular imaging technique for measuring the spatial and temporal distribution of the positron emitters in the human body by coincidence detection of the annihilation photons resulting from positron decays (1, 2). Unlike magnetic resonance imaging (MRI) or X-ray computerized tomography (CT), which mainly provides anatomical information, PET, as well as single-photon emission computed tomography (SPECT), have the ability to monitor metabolic processes in living systems, namely functional imaging. PET and SPECT rely on the use of exogenous radioactive probes which provide a detectable signal. These biologically active probes can be designed to be tissue or receptor-specific and provide valuable information about metabolism, receptor/enzyme function, and biochemical mechanisms in living systems (3).

Principles of PET

PET is an analytical imaging technology developed to use molecules labeled with positron emitting radioisotopes as probes at the molecular level to image human biological process in real time (4-7). Carbon-11, nitrogen-13, oxygen-15, and fluorine-18, are the most commonly used positron emitting radioisotopes (**Table 1.1**). Positron emitters of Cu, Zn, Br, Rb, I, Fe, Ga are also used.

Table 1. 1 Physical properties of the most commonly used short-lived radionuclides in PET (2, 3)

Isotope	Half-life (min)	Specific activity^a (Ci/mmol)	Maximum energy (MeV)	Range (mm) in H₂O^b	Product	Decay product
¹¹ C	20.4	9.22×10^6	0.96	4.1	[¹¹ C]CO ₂ [¹¹ C]CH ₄	¹¹ B
¹³ N	9.97	1.89×10^7	1.19	5.4	[¹³ N]NO _x [¹³ N]NH ₃	¹³ C
¹⁵ O	2.04	9.08×10^7	1.72	8.2	[¹⁵ O]O ₂	¹⁵ N
¹⁸ F	110	1.71×10^6	0.635	2.4	[¹⁸ F]F ⁻ [¹⁸ F]F ₂	¹⁸ O

^aTheoretical maximum; in reality the measured specific activities are 5000 times lower because of unavoidable dilution with the stable element. ^bMaximum linear range.

In a typical PET imaging study, a positron-labeled probe (radiotracer) is administered (most of times intravenously) into the subject, and then PET scans are performed to provide real time measurements of multi-compartment radiotracer concentration and also radiolabeled metabolites concentration. In PET, the radionuclide decays within the body by positron emission, and the emitted positron (β^+) travels a short distance (0.5 – 2.0 cm, depending on its specific kinetic

energy), after which it collides with an electron in the surrounding tissues, which results in an annihilation event. The energy equivalent ($E = mc^2$) of the annihilation event is emitted through two 511 keV gamma ray photons (γ) that travel at 180° to each other (**Figure 1.1**) (3). The two gamma ray photons are detected simultaneously and also electrically when they strike two opposing detectors (8). During a PET scan, the system counts the number of times each detector pair is hit simultaneously, thus the raw data generated from a PET scan are simply the list of counts obtained along each line of response (9). With the sophisticated three-dimensional (3D) or two-dimensional (2D) reconstruction algorithms, raw projection data can be converted into high quality images to provide quantitative measurements of radiotracer concentration in a subject at spatial resolutions of a few millimeters. In recent years, an important advance in imaging instrumentation is the integration of PET and CT into one device (10-12), providing valuable insight by combining functional information from PET images to detailed anatomical images from CT scans (13).

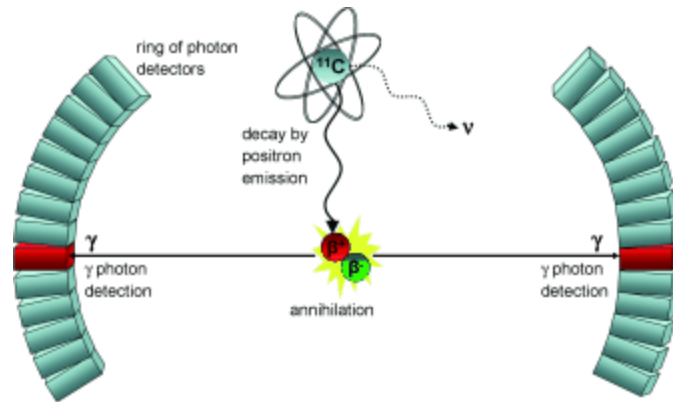


Figure 1. 1 Schematic representation of the principles behind PET.

Figure is reproduced from (3). A biologically active molecule is labeled with a positron emitting radioisotope (radiotracer) such as ^{11}C . Positrons emitted from the radiotracer are antielectrons that travel a short distance and collide with an electron in the surrounding tissue. As a result, annihilation occurs through the emission of two 511 keV gamma ray photons 180° apart. The two gamma rays photons are both detected simultaneously and electronically when they strike two opposing detectors.

In summary, there are four components of a typical PET study: production of radionuclides, incorporation of radionuclides and purification of the probe, quality control, data acquisition and reconstruction. The first two components will be discussed in detail at the end of this chapter.

The contribution of PET in the diagnosis of infectious diseases

Early detection and diagnosis of infection and inflammation is crucial for the optimal management of patients with infectious diseases. Traditional diagnostic method starts from

obtaining medical history and performing physical exam. Additionally, a more detailed test would include the culture of infectious agents isolated from a patient, typically blood or urine sample. Several tests such as microbial culture, microscopy, biochemical tests and molecular diagnostics can be performed with cultured samples to identify the infectious organism. In some cases, when occult infection is suspected to be present, a biopsy is performed followed by tests that are similar to blood and urine test to identify the pathogen (14). However, clinicians encounter substantial challenges in detecting and localizing the exact sites of infection using traditional techniques.

In order to complement the current diagnostic techniques for infectious diseases, several different modern nuclear imaging modalities have emerged as important tools for clinicians over the past decades. Modern anatomical imaging techniques such as x-ray computed tomography (CT), ultrasonography (US) and magnetic resonance imaging (MRI) can provide excellent structural resolution for visualizing different important diseases including those related to infection and inflammation (15), but these anatomical imaging techniques are restricted to those diseases associated with structural abnormalities, which usually would not happen at early stage of diseases. Additionally, a lesion after the cure of infectious disease has minimal anatomical difference compared to the active infection, which also makes it difficult for clinicians to evaluate the status of the disease using anatomical imaging modalities (16). However, metabolic and functional imaging techniques, such as Positron Emission Tomography (PET) and Single Photon Emission Computed Tomography (SPECT), have the capacity to visualize cellular functions and molecular processes of living systems through an exogenous biologically active probe. These biologically active probes interact with the molecular target of interest in the living

subject and ideally could identify the localization of infection and also quantify inflammation foci (17). These molecular imaging modalities have the potential to complement the role of anatomic imaging modalities in most clinical settings (18).

Among these very useful molecular imaging modalities, the most widely used one is PET, which utilizes the radiotracer ^{18}F -fluorodeoxyguucose (FDG). The concept of Positron Emission Tomography (PET) with ^{18}F -fluorodeoxyguucose (FDG) was born in mid-1970s, when ^{18}F -FDG was developed in Brookhaven National Laboratory by the team led by Dr. Al Wolf and Dr. Joanna Fowler (19). In 1976, the first human PET study with [^{18}F]-FDG was performed at the University of Pennsylvania. The study included imaging of both the brain and the whole body using very primitive techniques. During the elementary stage of [^{18}F]-FDG-PET imaging, the focus was to determine the difference in brain function between normal subjects and subjects with neuropsychiatric disorders (20-23). However, a major extension of [^{18}F]-FDG-PET usefulness from brain function imaging to oncology occurred in the 1980s. Based on the knowledge that malignant cells have significantly elevated glycolysis activity (24, 25), coupled with the introduction of whole-body PET imaging techniques, whole-body [^{18}F]-FDG-PET imaging became the methodology for the diagnosis, staging, treatment planning, and treatment monitoring of malignant disease (26-30). Furthermore, the integration of PET and CT technology added another dimension to the [^{18}F]-FDG-PET imaging and further enhanced its role in oncology. The advantages of [^{18}F]-FDG-PET/CT include but are not limited to: optimal spatial resolution, accurate anatomical localization of abnormalities, rapid diagnostic results, whole-body analysis, and lack of metallic hardware artifacts (18, 31, 32). Due to the inherent nature of ^{18}F -FDG to detect elevated glycolysis activity, organs such as kidneys, bladder, brain, and

meninges that have a high metabolism under normal conditions will be difficult to interpret on ^{18}F -FDG-PET/CT images (18). In a typical ^{18}F -FDG-PET study, ^{18}F -FDG is injected intravenously, and then the PET detector can identify hypermetabolic foci. A semi-quantitative analysis is performed by determining the standardized uptake value (SUV), which is related to the concentration of ^{18}F -FDG in the corresponding tissue or organs (33).

Role of ^{18}F -FDG-PET for the diagnosis of infectious diseases

Despite the great success of ^{18}F -FDG-PET/CT in oncology, it was also observed that inflammatory cells involved in host response to infectious diseases could take up ^{18}F -FDG. The increased uptake of ^{18}F -FDG in activated inflammatory cells, such as lymphocytes or macrophages, is related significantly to increased levels of glycolysis. This is a result of increased numbers of cell surface glucose transporters, particularly after cellular stimulation by multiple cytokines (34-37). In addition, a fraction of FDG uptake in malignant tissues is a result of increased glycolysis in the large numbers of inflammatory cells that are present (38). It has also been reported that standardized uptake values (SUVs) of inflammatory and non-neoplastic lesions tend to remain stable or decrease, while those of malignant lesions tend to increase overtime (39-41). In order to differentiate between malignant and inflammatory processes, dual-time-point ^{18}F -FDG-PET/CT has been proposed based on the discovery. Moreover, in recent years, systemic assessment of the value of ^{18}F -FDG-PET/CT in the diagnosis of infectious and inflammatory diseases has been conducted. Therefore, in this chapter, the contribution of ^{18}F -FDG-PET/CT in the diagnosis of musculoskeletal infection, soft tissue infection, cardiovascular diseases and tuberculosis will be briefly introduced.

Musculoskeletal Infections

Osteomyelitis. Osteomyelitis is a bone infection caused by bacterial, fungal, or bacterial microorganisms. The diagnosis of sub-acute or chronic osteomyelitis is problematic especially in the case of pre-existing alterations of osseous structures due to previous surgery or trauma. In this clinical setting, ^{18}F -FDG-PET/CT is very effective (33). De Winter et al. conducted prospective studies on the usefulness of ^{18}F -FDG-PET/CT for the diagnosis of chronic skeletal infections in 60 patients who have undergone recent surgery. The authors reported a sensitivity, specificity, and overall accuracy of 100%, 86%, and 93%, respectively (42).

Diabetic foot. Five to 10% of diabetic patients have foot ulcers that evolve to osteomyelitis, and peripheral neuropathy is common in patients with diabetes mellitus (DM) (43). Osteomyelitis compromises up to 33% of the diabetic foot infections, which is often due to direct, contiguous contamination from the soft tissue lesions (44). In this clinical setting, because systemic symptoms or signs of infection are often absent in patients with osteomyelitis in the setting of DM (45), and also a large portion of diabetic patients with deep foot infection do not have leukocytosis in spite of active disease (46), detecting elevated markers for inflammation using ^{18}F -FDG-PET/CT has become useful in this clinical setting (**Figure 1.2**) (47).

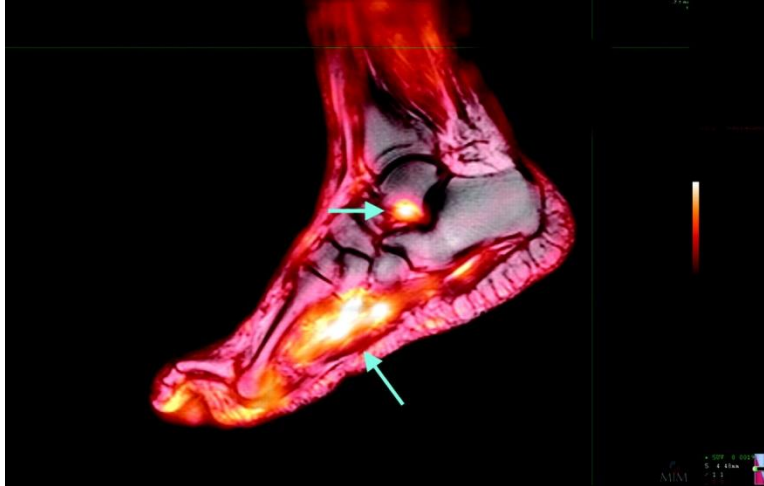


Figure 1. 2 ^{18}F -FDG-PET and MRI images of a patient with diabetic foot and suspected bone infection. The FDG-PET image shows significant uptake in the soft tissue in the plantar aspect of the foot, and also reveals a focus of abnormal activity in the talus. Image reproduced from (47).

Infected prosthesis. ^{18}F -FDG-PET/CT also has a great potential for diagnosing of patients with suspected orthopedic prosthetic infection, because the procedure is weakly affected by artifacts from metallic implants. A preliminary prospective study including 62 patients evaluated the accuracy of ^{18}F -FDG-PET for the investigation of painful lower limb prostheses. A final diagnosis was made by surgical exploration or clinical follow-up for one year. The sensitivity, specificity, and accuracy for PET were 90.9%, 72%, and 77.8% respectively to detect infection in knee prosthesis (48).

Soft Tissue Infection

Fever of unknown origin (FOV). FOV is defined as a body temperature higher than 38.3 °C, lasting for at least three weeks, without any diagnosis after three days of investigations for inpatient or three outpatient consultations (49, 50). Infections, malignancies, collagen vascular diseases, and autoimmune disorders account for the majority of cases of FOV. No diagnosis can be made in up to 50% of cases (51), so accurate localization and characterization of the cause of FOV will substantially improve the management of these patients who suffered from the symptoms and signs (18). ^{18}F -FDG-PET has been shown to be superior than ^{67}Ga SPECT in patients with FUO (52). In a prospective study with ^{18}F -FDG-PET, Stumpe et al. studied 45 ^{18}F -FDG-PET scans from 39 patients with suspected infectious foci and reported 40 true-positive, 4 false-positive, and 1 false-negative result (53). A structured diagnostic protocol relying on ^{18}F -FDG-PET/CT procedure is proposed in **Figure 1.3** (33) to enrich the tool box of physicians to manage FOV.

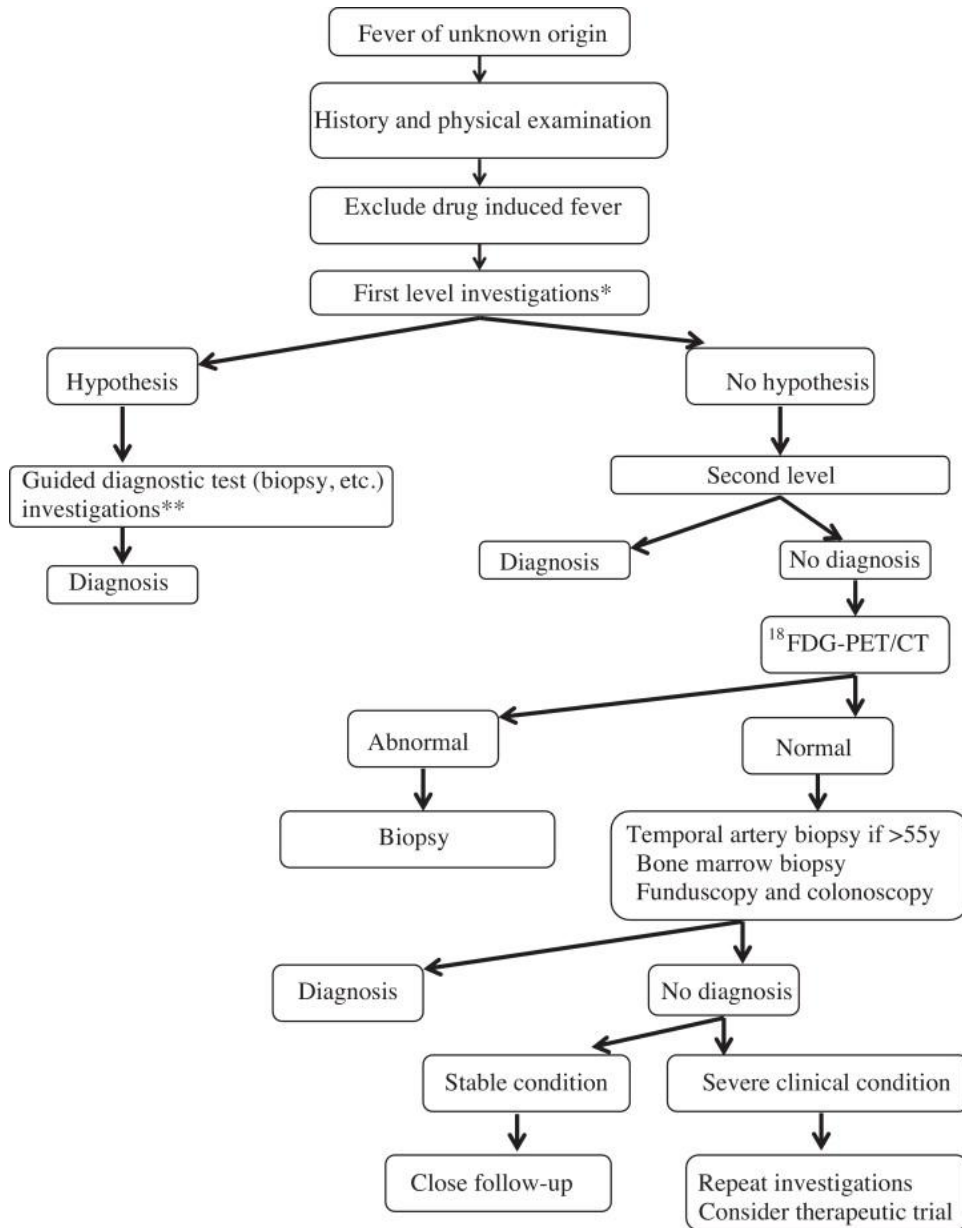


Figure 1. 3 Proposed structured diagnostic protocol for ^{18}F -FDG-PET/CT in patients presenting with fever of unknown origin (FOU). Image reproduced from (33).

Other soft tissue infections. ^{18}F -FDG-PET is a valuable tool for the evaluation of other soft tissue infections such as possible infection of vascular grafts (54), even if the CT results are

negative (55). In addition to this, ^{18}F -FDG-PET has the potential for the evaluation of other uncommon entities, such as various stages of malarial infection (56), cystic fibrosis (57), and chronic granulomatous disease (58, 59).

Cardiovascular diseases

Infective endocarditis. The gold standard for the diagnosis of infective endocarditis (IE) is considered to be the modified Duke criteria (60). However, this diagnosis can still be challenging, especially in the case of prosthetic valve endocarditis (PVE), for which echocardiography can be inconclusive in almost 30% of all cases (61). The usefulness of ^{18}F FDG-PET/CT in this clinical setting is reported in a very important prospective study in which the authors recruited 72 patients with suspected PVE and applied both ^{18}F FDG-PET/CT and modified Duke criteria to make diagnosis (62). When abnormal FDG uptake around the prosthetic valve was added as a new major criterion, the sensitivity of these new modified Duke criteria at admission increased from 70% to 97% ($p = 0.008$), without any decrease of specificity (62). This study suggests that ^{18}F FDG-PET/CT is a promising tool in the diagnosis of PVE, when using the modified Duke criteria cannot be used to make a final diagnosis.

Infection of cardiovascular implantable electronic devices. Infection of cardiovascular implantable electronic devices (CIED) is a serious complication and can lead to complete removal of the device. The diagnosis of infection remains very challenging. Consequently, ^{18}F FDG-PET/CT could be useful in the management of patients suspected of having a CIED

infection, to assess the extent of the infectious process and to help restrict lead removal to the appropriate patients (63).

Tuberculosis

Tuberculosis (TB) is a global health threat and one of the most lethal infectious diseases worldwide. In 2011, nearly 9 million people fell ill from TB and 1.4 million died (64). The World Health Organization (WHO) has estimated that one-third of the world's population is infected with this pathogen. Therefore, a prompt diagnosis of TB is critical for infection controls and patients management. Diagnosis of TB infection, especially extra-pulmonary disease, is confounded by limited current diagnostic strategies, which include radiological and bacteriological tests, the tuberculin skin test (TST), and the interferon-gamma release assays (IGRAs) (65). In the last two decades, the functional imaging technique that monitors glucose metabolism in tissues (^{18}F -FDG PET/CT) has emerged as a novel diagnostic tool for fevers of unknown origin (FOU) and occult infections. In the case of TB, active granulomatous inflammation could induce accumulation of ^{18}F -FDG. Several case reports have evaluated the use of ^{18}F -FDG PET/CT in a small number of TB patients to evaluate therapeutic response, and concluded that ^{18}F -FDG PET/CT can be used as an early non-invasive marker for therapeutic response (66-70).

Other radiolabeled compounds for the diagnosis of infectious and inflammatory diseases

Despite the fact that ^{18}F -FDG-PET/CT is a highly sensitive and widely used imaging tracer in many different clinical settings, the inherent nature of ^{18}F -FDG makes it difficult to differentiate among oncologic, inflammatory, and infectious processes. ^{18}F -FDG-PET/CT is dependent on host inflammatory responses. But these host inflammatory responses might be reduced or missing in immunosuppressed patients such as those undergoing cancer chemotherapy, those with HIV/AIDS, and organ transplant patients. Therefore, there is a pressing need for a rapid, whole-patient imaging technique that targets the pathogen directly instead of the host immune response so that direct localization of the pathogen is possible.

Imaging enterobacteriaceae infection with ^{18}F -fluorodexoysorbitol

Enterobacteriaceae, including pathogens such as *Escherichia coli* and *Klebsiella pneumoniae*, are the most common cause of Gram-negative bacterial infections in humans, and also are a cause of serious multidrug-resistant (MDR) nosocomial infections. In addition to this, several enterobacteriaceae species are formally recognized as biothreat pathogens by the U.S. Centers for Disease Control and Prevention (CDC) (71). Pathogenic Enterobacteriaceae are differentiated from other organisms through their use of selective metabolism of sorbitol as a metabolic substrate. Weinstein et al hypothesized that a positron-emitting analog of sorbitol, 2- ^{18}F -fluorodeoxysorbitol (^{18}F -FDS), would be a potentially useful radiotracer to selectively visualize and localize these bacteria *in vivo*. Adopting the radiosynthesis methods described in reference (72), the authors derived ^{18}F -FDS from commercial ^{18}F -FDG for use as a diagnostic tool with broad utility (73). The results showed that ^{18}F -FDS-PET rapidly differentiated true infection

from sterile inflammation in an *Escherichia coli* murine myositis model while ^{18}F -FDG could not distinguish the infected thigh from the sterile, inflamed thigh qualitatively (**Figure 1.4**) (73). Furthermore, the result showed that ^{18}F -FDS-PET was able to distinguish *Escherichia coli* infection from Gram-positive bacteria *Staphylococcus aureus* infection in a mixed infection murine myositis model (73). Probes such as ^{18}F -FDS would allow noninvasive monitoring of disease progression or regression, without repeated time-consuming cultures.

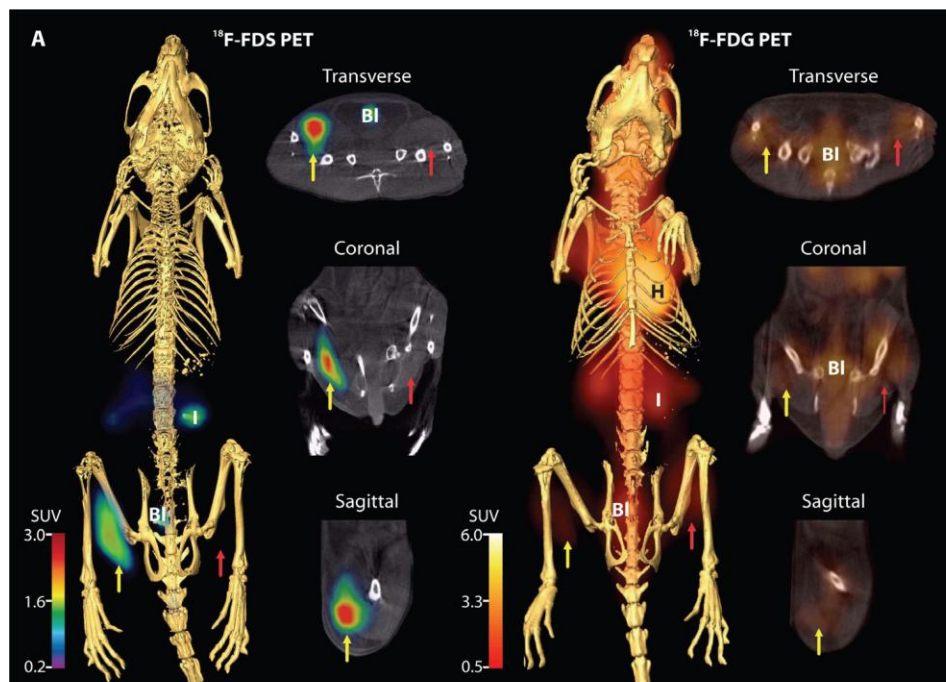


Figure 1. 4 PET/CT images of ^{18}F -FDS in *E. coli* myositis mice model.

^{18}F -FDS signal is observed in the infected (yellow arrow) but not in the inflamed (control) sterile thigh (red arrow), while ^{18}F -FDG signal was observed in both infected and inflamed thighs.

Image reproduced from (73). H, heart; I, intestine; BI, bladder.

Radiolabelled antibiotics

In an effort to circumvent the dependence of radioactive probes on host inflammatory responses to detect infection, various antibiotics and peptides, inherently designed to specifically target infectious agents instead of host inflammation, have been radiolabelled and evaluated. The radiolabelling of antibiotics was pioneered by Solanki et al (74) in late 1980s. In the next two decades, the radiolabelled antibiotics extended to ciprofloxacin (Infecton), sparfloxacin, ceftizoxime, isoniazid, ethambutol, fluconazole, entofloxacin (75). Of these probes, ^{99m}Tc -ciprofloxacin is the one that has been studied most extensively. It is a synthetic broad spectrum fluoroquinolone antibiotic that binds to prokaryotic topoisomerase IV and DNA gyrase (76, 77). In a large multi-center study of using [^{99m}Tc]-ciprofloxacin for diagnosis of osteomyelitis infection, Britton et al reported that the overall sensitivity and specificity were 85.5% and 81.6% for a total of 879 patients (78, 79). However, when it comes to the knee prosthesis animal model, the specificity of [^{99m}Tc]-ciprofloxacin is much lower (80, 81). Ciprofloxacin, in addition to fleroxacin and trocafloxacin, have also been radiolabelled with fluorine-18 for PET imaging (82). The evaluation of [^{18}F]-ciprofloxacin and [^{18}F]-fleroxacin in an infected animal model (rat and rabbit model) concluded that: (1) sufficiently high concentrations were achieved to deliver antibacterial activity; (2) CNS toxicity is unlikely because of low distribution in brain; and (3) uptake of radiolabelled probe at infection site was not significantly higher than in the control site (83, 84). These results indicate that the low specific activity of the radiolabelled antibiotics are diluted to therapeutic dose by co-injected cold standard drugs (83, 84). From a synthetic point of view, the specific activities of [^{18}F]-ciprofloxacin and [^{18}F]-fleroxacin are limited by the fluorine exchange labelling method, which is about 1000 times lower than nucleophilic substitution (15). To date, radiolabelled antibiotics represent a promising methodology for determining

pharmacokinetics *in vivo* using PET, but requires further clinical studies before they can be used as infection/inflammation probes.

Radiolabelled antimicrobial peptides

Antimicrobial peptides are part of the innate immunity, and are produced by different cell types such as phagocytes, epithelial cells, and endothelial cells (85). Radiolabelled antimicrobial peptides were evaluated as infection probes based on their ability to kill a variety of pathogens (bacteria, fungi, virus), and also based on the presumption that radiolabelled antibiotics which might provide false-negative results because of emerging drug resistance. The basic common mechanism of antimicrobial peptides is that the electrostatic interaction of cationic domains with the negatively charged surface of the micro-organisms (86).

Human neutrophil peptide-1 (HNP-1). Human neutrophil peptide (HNP)-1, a member of the family of defensins, is one of the most extensively studied antimicrobial peptides (87). [^{99m}Tc]-HNP-1 was able to visualize *Staphylococcus aureus* and *Klebsiella pneumonia* infection in mice model rapidly, and the signal was from the accumulation of [^{99m}Tc]-HNP-1 at the site of infection (88). However, the T/NT (infected/uninfected) was low (~1.3) and decreased over time (88).

Ubiquicidin UBI. Ubiquicidin 29-41 (UBI 29-41, Thr-Gly-Arg-Ala-Lys-Arg-Arg-Met-Gln-Tyr-Asn-Arg-Arg, MW 1.693 kDa), was originally isolated from mouse macrophage cells, has been radiolabeled with ^{99m}Tc and evaluated for the purpose of detecting infection. [^{99m}Tc]-UBI 29-41

allowed rapid visualization of both Gram-positive and Gram-negative bacteria infection with very little accumulation in sterile inflammatory tissues (89). In another imaging study in *S. aureus* infected rabbits undergoing ciprofloxacin treatment, the uptake of [^{99m}Tc]-UBI 29-41 decreased after antibiotic treatment (90), implying the potential use of this probe for chemotherapy monitoring.

Inflammation Probes

Inflammation is “the response of tissues to any injury in order to bring serum molecules and cells of the immune system to the site of damage” (16), while infection means “contaminations with microorganisms” (91). Characteristic processes of inflammation include locally increased blood supply, enhanced vascular permeability, enhanced transudation of plasma proteins and influx of leukocytes (16). Meanwhile, powerful defense mechanisms, consisting of leukocytes and plasma proteins are also activated (92). Correspondingly, one of the strategies to non-specifically image inflammation is to utilize the increased vascular permeability and blood supply, such as ⁶⁷Ga-citrate and radiolabelled non-specific immunoglobulins. On the contrary, the specific strategy is to utilize the influx of leukocytes, including radiolabeled leukocytes, anti-granulocyte monoclonal antibodies or leukocyte receptor-binding ligands (16).

Table 1. 2 Summary of radiolabeled compounds for infection/inflammation imaging (16).

Physiological Process	Targeting mechanisms	Tracer category	Examples
			[⁶⁷ Ga]-citrate (93, 94)
Enhanced vascular permeability	Non-specific		non-specific immunoglobulins (95, 96) Liposomes (97-99) Avidin/[¹¹¹ In]-biotin (100)
Endothelial activation	Antigen binding	Antibodies	F(ab') ₂ -anti-E-selectin (101) Anti-ICAM-1 Mab (102, 103)
Enhanced influx of granulocytes	Granulocyte influx		Radiolabeled granulocytes (104, 105)
Increased metabolic requirements	Enhanced glucose uptake		[¹⁸ F]-FDG (18, 33)
Presence of microorganisms	Affinity for microorganisms	Antimicrobial agents	Ciprofloxacin (16, 78) Antimicrobial peptides (79, 86)

The role of PET in drug discovery & development

Pharmacokinetics (PK) refers to the time-course study of drug absorption, distribution, metabolism, and excretion (ADME), whereas pharmacodynamics (PD) refers to the biological effects that the drugs exert on the subjects. Historically, due to various limitations associated with technology and also the knowledge gap, anti-infective therapy (dose and duration of treatment) is established using plasma PK data together with drug efficacy data once the treatment is initiated. However, most drugs exert their efficacy not within the plasma compartment, but at the site of infection. Once the drug is distributed to the target tissue from central compartment (plasma), then it binds to binding targets such as enzymes, ion channels, receptor proteins. Therefore, target tissue concentrations and target occupancy are the gaps between plasma PK and PD effect (**Figure 1.5**). Because of its ability to obtain direct quantitative information of the radiolabelled drugs in vivo non-invasively, PET has been creatively applied to lab animals and humans to address critical questions in drug discovery and development, including measuring target tissue concentration and target engagement.

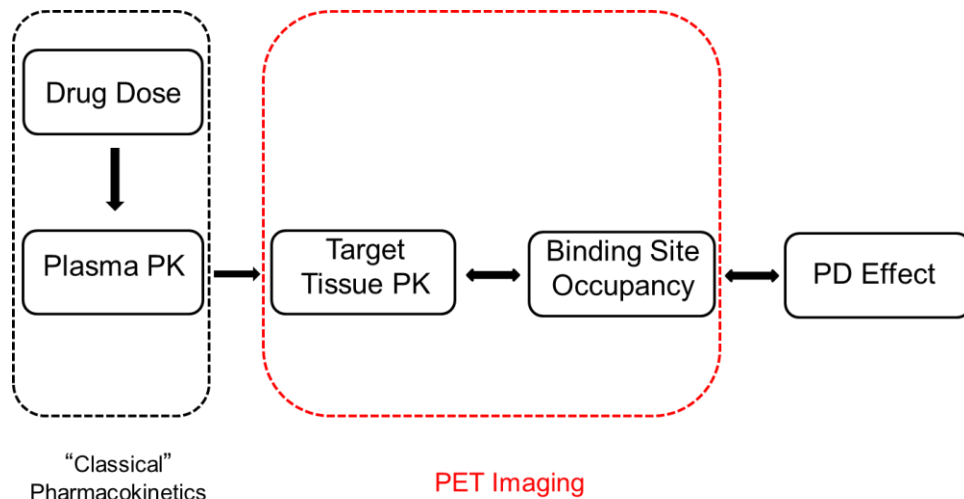


Figure 1. 5 The links between serum pharmacokinetics and drug effect.

PET is used to measure both target tissue PK and target engagement. Image is adapted from reference (106).

Drug tissue distribution

As discussed above, often the drugs do not exert their effects from plasma compartment, but at the target tissue, which in the case of antibiotics is the site of infection. The assumption of the equilibrium between plasma drug concentration and tissue concentration does not always hold true (106). Actually the drug concentrations in the target compartment could be substantially different from the plasma compartment. Of the many factors that restrict drug distribution into tissue, the blood-brain barrier is the best example (107). If the drug fails to reach optimal concentrations in the target tissue, consequences such as failed therapy will occur, and also the triggering of bacteria resistance in the case of antibiotics (108-110). As a result, considering impaired drug distribution is recommended for current medical treatment (111). Now that people

realize that the drug concentration at the infection site is a better predictor than plasma concentration when it comes to clinical outcome (112), regulatory authorities such as Food and Drug Administration (FDA) in the United States and European Medicines Evaluation Agency (EMA) in Europe require tissue concentrations of drugs in the development of new antibiotics (113).

Measuring drug tissue distribution using PET

Non-invasive imaging techniques, such as PET and Single Photon Emission Computed Tomography (SPECT), have the capacity to image drugs and other bioactive molecules labelled with positron emitters, and to provide an advanced methodology to acquire information of drug absorption, distribution, metabolism, and excretion quantitatively *in vivo* in real time. With the rapid expansion in innovative radiochemistry, PET imaging has emerged as a powerful tool in the field of drug discovery and development, especially in the phase of determining drug tissue distribution, and the reliability has been established and compared to direct measurements (114). Another advantage that sets PET imaging from other techniques is that the methodology developed for laboratory animals can be readily translated to human studies. In a pioneering study, Fischman et al have evaluated the PK of ^{18}F -travafloxacin in healthy human subjects using PET. Inter-tissue and inter-subject variability have been characterized (**Figure 1.6**) (115).

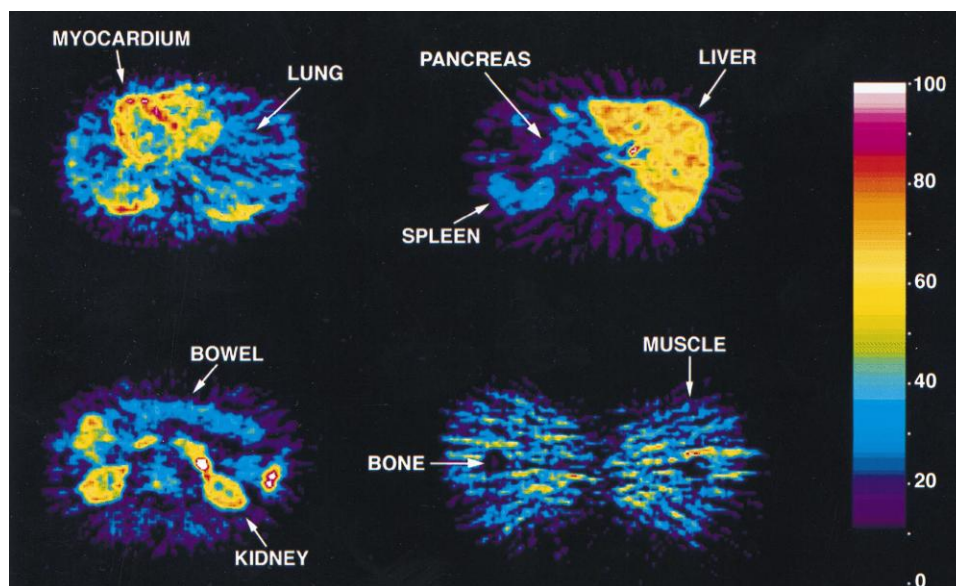


Figure 1. 6 Peripheral organ distribution of [¹⁸F]-travafloxacin determined by PET in a healthy male volunteer. The area of maximum concentration on each image is represented as 100% of the color scale. Image reproduced from (115).

Measuring drug tissue distribution using other methods

Another very important method of localization of drug molecules in biological tissues is mass spectrometric imaging (MSI). A number of different MSI technologies are available depending on the ionization method, detection mode. (116). One of the most widely used techniques is Matrix-Assisted Laser Desorption/Ionization mass spectrometric imaging (MALDI - MSI) (116-118). In a typical MALDI-MSI study, sections of selected tissues or dosed whole animals are coated with an UV-absorbing matrix. The analytes are then extracted from the tissue by organic solvent and co-crystallized with the matrix when the solution dries. A laser is irradiated across the surface of the tissue sample causing ionization of the matrix and analyte at the same time (119). MALDI-MSI is the most sensitive method currently available, with the spatial resolution of 50 –

200 μm in single organs and 500 – 1000 μm in whole body rodents (119). Besides sensitivity, other key advantages of MALDI-MSI include label-free (the fact that it doesn't require the use of radioactive labels) and the ability to detect metabolites and endogenous species of the drug molecule. However, MALDI-MSI suffer the disadvantages of: (i) interference from matrix signal; (ii) the hypothesis that drug distribution in tissue is homogenous does not hold true all the time; (iii) the procedure is invasive, and the sample preparation is quite complicated; (iv) the extraction efficiency of drugs from tissue is another dimension of complexity (119, 120). Prideaux et al applied MALDI-MSI to image the second-line TB drug moxifloxacin in TB-infected rabbits. Moxifloxacin was found to be distributed in granulomatous lesions at higher concentrations (**Figure 1.7**) (121).

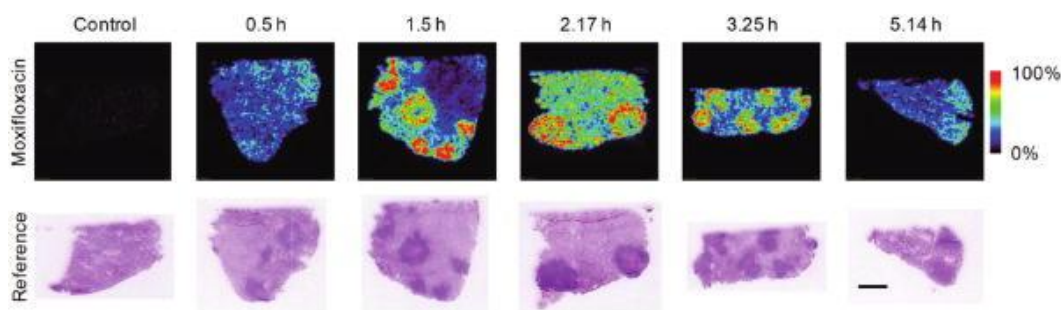


Figure 1. 7 MALDI-MS images of moxifloxacin distributions in the tuberculosis infected rabbit lung biopsy. The reference tissue is from H&E stain. Moxifloxacin remains higher concentration than surrounding lung tissues after 1.5 h. Scale bar = 5 mm. Image reproduced from (121).

Microdialysis (MD) is another promising tool to measure drug tissue distribution (122). The technology was initially designed to measure concentrations of various neurotransmitters in

rodents brain, then extended to the area of PK (123). The principle of MD is to implant a MD probe, which connects with a semi-permeable hollow fiber membrane, into the tissue of interest. Consequently, a concentration gradient is set up which drives the diffusion of the drug from the tissue to the probe. The dialysate is then collected and analyzed at different time points (124, 125). MD is the only feasible technique that allows continuous monitoring in any tissues. However, it suffers drawbacks associated with its invasive nature and recovery reliability limitation (126).

Determine target engagement using PET

In order to correlate drug efficacy and PK parameters, the ultimate question is: what percentage of drug targets (enzymes, ion channels, transporters) have to be occupied for therapeutic efficacy? To answer this question, there has been a growing appreciation of the value of biomarkers that can report on drug-target interactions in preclinical and clinical settings (127, 128). The importance of target occupancy in drug development is obvious, especially when it comes to explaining the lack of efficacy: is it because of insufficient target occupancy or because of the invalid target? There are several established methods to measure target engagement in different systems. PET represents a very promising method to measure target engagement in human, especially for those targets that cannot be easily measured in blood samples (**Figure 1.8**) (129). For example, PET has helped with the identification of histamine H₃ receptor antagonist GSK189254 by showing that the target occupancy of this drug candidate is 10-fold higher in humans than preclinical animal models, using a carbon-11 version of the drug (130).

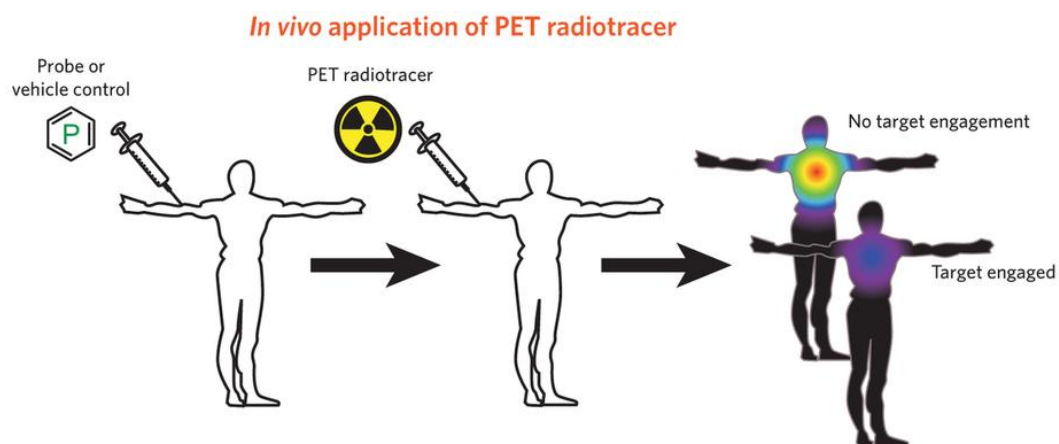


Figure 1. 8 Measuring target engagement in humans using PET.

Human subjects are pretreated with cold standard probe, then administered radiotracer. Engaged targets do not bind radiotracer while PET signal can be used to assess target engagement. Image reproduced from (129).

Production and incorporation of radionuclides

Short-lived positron emitters, generated from a cyclotron (a compact particle accelerator which is capable of producing proton or deuteron beams) during irradiation of various target elements depending on the desired radioisotope (^{11}C , ^{13}N , ^{15}O , and ^{18}F), are usually converted in synthetic precursor form either within cyclotron target or immediately after exiting the target. Among all the positron emission isotopes, carbon-11 and fluorine-18 are of particular interest for the following reasons: (i) carbon is present ubiquitously in natural products and drug molecules; (ii) ^{11}C -labelled molecules behave the same as their carbon-12 versions chemically and biologically; (iii) although there is a small pool of biologically active molecules with fluorine, the half-life of fluorine-18 (110 min) enables multiple step synthesis and transportation of the tracer to a

different site; (iv) fluorine-18 provides better resolution than carbon-11 because of the energy level (3).

Radiolabelling with carbon-11

Carbon-11 is usually generated by proton bombardment of nitrogen-14, followed by emission of an α particle (131, 132). The two most important carbon-11 precursors used in syntheses are: $[^{11}\text{C}]\text{CO}_2$, when small amounts of oxygen are present; or $[^{11}\text{C}]\text{CH}_4$, when hydrogen is present instead. From then, a wide range of precursors are generated (**Figure 1.9**) (3). The half-life of carbon-11 is 20.4 min, which restricts multiple step syntheses.

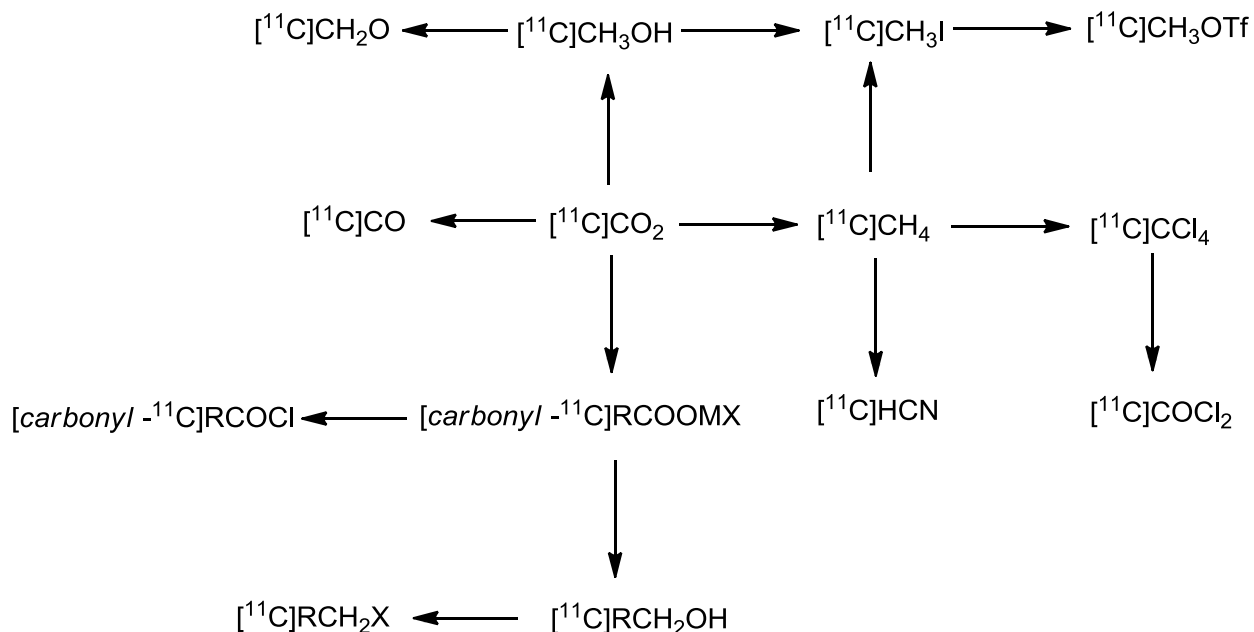


Figure 1. 9 Important ^{11}C precursors used in syntheses that are made from $[^{11}\text{C}]\text{CO}_2$ and $[^{11}\text{C}]\text{CH}_4$ (3).

The incorporation of a ^{11}C -methyl group ($[^{11}\text{C}]\text{CH}_3$), namely ^{11}C methylation, is the most widely used method for radiolabelling with carbon-11. $[^{11}\text{C}]\text{Methyl iodide}$ ($[^{11}\text{C}]\text{CH}_3\text{I}$) is the most common methylation agent, which is prepared by treating $[^{11}\text{C}]\text{CO}_2$ with LiAlH_4 , followed by gas-solid iodination at high temperature (133). A more reactive methylating agent is $[^{11}\text{C}]\text{methyl triflate}$ ($[^{11}\text{C}]\text{CH}_3\text{OTf}$). $[^{11}\text{C}]\text{CH}_3\text{OTf}$ is prepared by passing gaseous $[^{11}\text{C}]\text{CH}_3\text{I}$ through a silver triflate column at $200\text{ }^\circ\text{C}$ (134), and has gained more popularity because its higher reactivity can lead to more rapid reactions. The methylation reactions are generally carried out either by nucleophilic reactions with amine, alcohol or thiol precursors or by palladium-mediated methylation with stannane. A typical carbon-11 methylation reaction usually involves trapping of the methylation agent ($[^{11}\text{C}]\text{CH}_3\text{I}$ or $[^{11}\text{C}]\text{CH}_3\text{OTf}$) in solvent and then heating this for a very short time (usually less than 5 min). Important radiotracers generated by carbon-11 methylation include Pittsburgh Compound B ($[^{11}\text{C}]\text{PIB}$) for imaging amyloid plaques in Alzheimer's disease (135) and raclopride for imaging dopamine receptor (**Figure 1.10**) (136, 137).

$[^{11}\text{C}]\text{HCN}$ is the precursor for ^{11}C -cyanation reactions, which is of great interest because the nitrile group exists in a number of important drug molecules as well as biologically active molecules. $[^{11}\text{C}]\text{HCN}$ is prepared by reducing $[^{11}\text{C}]\text{CO}_2$ to $[^{11}\text{C}]\text{CH}_4$ in a nickel furnace, followed by reaction with NH_3 over platinum (138). Examples of tracers generated by ^{11}C -cyanation reactions include $[^{11}\text{C}]\text{metergoline}$ (serotonin receptor antagonist) and $[^{11}\text{C}]\text{RPR-72840A}$ (serotonin reuptake inhibitor) (**Figure 1.10**) (139, 140).

The carbonyl group also widely exists in drug molecules and biologically active molecules. Labelling precursors for carbonyl group include $[^{11}\text{C}]\text{CO}$, which is prepared from $[^{11}\text{C}]\text{CO}_2$ through heated zinc; $[^{11}\text{C}]\text{RCOCl}$, prepared from corresponding Grignard reagents; and $[^{11}\text{C}]\text{COCl}_2$, prepared from reaction between $[^{11}\text{C}]\text{CCl}_4$ and Fe_2O_3 powder (3, 141).

Radiolabelling with fluorine-18

Fluorine-18 ($t_{1/2} = 110\text{min}$) is the most widely used radioisotope in PET imaging. Its favorable half-life enables sufficient time for multiple step synthesis. In addition to this, fluorine-18 has a short positron linear range in tissue (2.3 mm) which results in the highest resolution of PET images. Furthermore, fluorine-18 tracers are able to be transported to different sites because of its long half-life, as in the case of FDG these days, where commercially produced FDG gets distributed to hospitals hours away for routine clinical use.

The strategies for introducing fluorine-18 into compounds of interest are limited when compared to carbon-11 labelling, and are divided into two main categories: nucleophilic and electrophilic fluorination. Nucleophilic $^{18}\text{F}^-$ is generated from a nuclear reaction using enriched $[^{18}\text{O}]\text{H}_2\text{O}$, and is then eluted from a cation-exchange column to yield K^{18}F . The principle of nucleophilic ^{18}F -fluorination reactions is to increase the reactivity by removing water from the reaction vial and also forming $\text{K}^{18}\text{F}\cdot\text{K}_{222}$ complex with azacryptand (K_{222}) to expose the fluoride ion. Many very important PET tracers are produced using this method, such as $[^{18}\text{F}]\text{FDG}$ and $[^{18}\text{F}]\text{FLT}$ (**Figure 1.10**), which are both used in oncology applications (142). Electrophilic fluorination is less favored because the use of $^{18}\text{F}_2$ could result in low specific-activity labeled compounds and could

also afford non-specific labeling. However, emerging innovative approaches such as utilizing palladium aryl complexes for late-stage electrophilic ^{18}F -fluorination represents a very promising methodology for combating these issues (143).

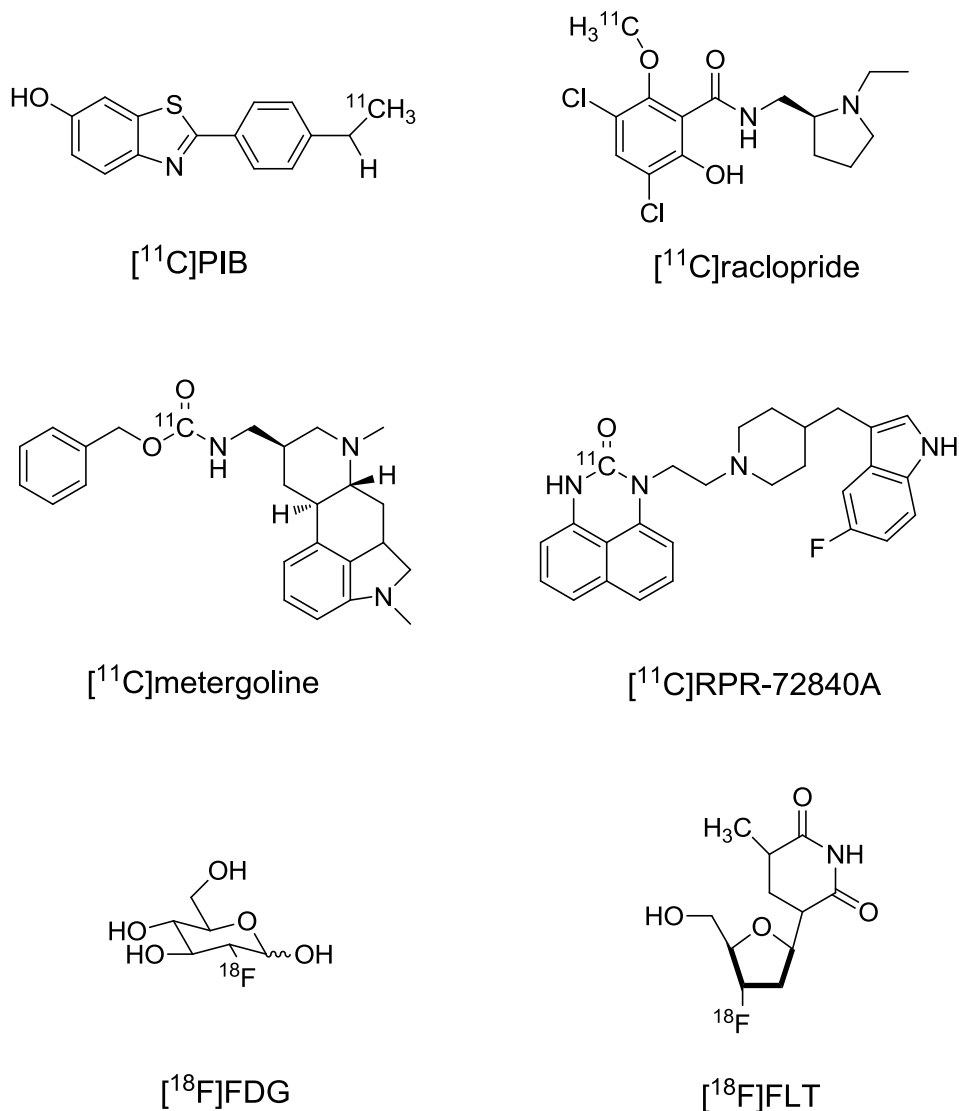


Figure 1. 10 Examples of important PET tracers labeled with carbon-11 and fluorine-18.

Summary

The introduction and advancement of PET instrumentation together with radioactive probes development (^{18}F -FDG, radiolabelled antibiotics, antimicrobial peptides, and other biologically active compounds) have made significant contribution in the early diagnosis of infectious diseases. Furthermore, PET has also enabled the quantitative measurements of tissue concentrations and target engagement of drug candidate molecules, therefore reducing the attrition rate in drug development. In this thesis study, we will develop radiolabelling strategies for novel antibacterial agents (long residence time enoyl-ACP reductase inhibitors, **Chapter 2 and 3**), currently prescribed antibiotics (pyrazinamide, **Chapter 4**), and also small molecules that target bacteria specifically (*para* – amino benzoic acid, **Chapter 5**), using positron emitting isotopes carbon-11 and fluorine-18. We have performed PET/CT scans, *ex vivo* analysis, cell uptake, PK/PD, and other methods to evaluate: (i) the tissue concentrations of radiolabelled compounds in living animals; (ii) their usefulness to detect and localize bacterial infection *in vivo*. The two clinical relevant pathogens, *Mycobacterium tuberculosis* and *Staphylococcus aureus* are used in this thesis study.

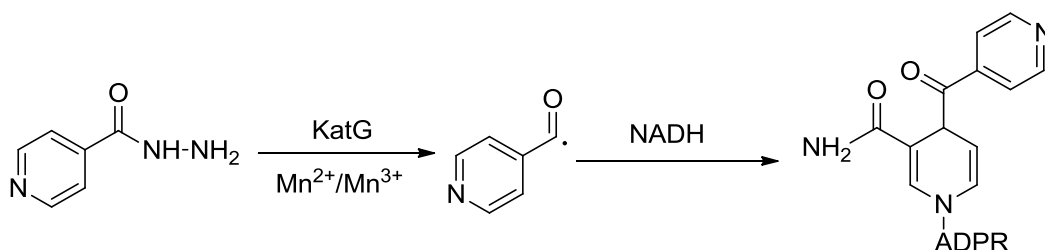
Chapter 2 Radiolabelling and Biological Evaluation of Time-Dependent Diaryl Ether Inhibitors of InhA, the Enoyl-ACP Reductase from *Mycobacterium tuberculosis*

Background

Mycobacterium tuberculosis is the causative agent of human tuberculosis (TB) (144), infects one-third of the world's population and is responsible for 9.0 million new infections and 1.5 million deaths in 2013 (145). The situation is complicated by HIV/AIDS infection, multidrug resistant TB (MDR-TB) and extensively drug resistant TB (XDR-TB) (146). In 2008, 22% of new TB cases were reported to be MDR-TB (147). The basic regimen recommended for TB treatment is comprised of the four front-line drugs: isoniazid (INH), rifampicin (RIF), pyrazinamide (PZA), and ethambutol (EMB). The regimen starts with two months initial phase, followed by INH and RIF for another four months (148). MDR-TB is resistant against INH or RIF, contributes to the spread and worsens the situation by lengthening the treatment from 6 months to nearly 2 years. XDR-TB is resistant to both front-line and second-line drugs and is extremely difficult to cure (149). Taken together, novel drugs with activity against drug-resistant TB are therefore urgently needed.

InhA, the enoyl-ACP reductase involved in the *M. tuberculosis* fatty acid biosynthesis (FAS II) pathway (150), catalyzes the last reaction in the elongation cycle, and is the target for INH, one of the most effective and widely used anti-tubercular drugs (150, 151). INH is a prodrug that is activated by the mycobacterial catalase-peroxidase enzyme KatG (**Scheme 2.1**) (150, 152-154). When NAD(H) is present, the activation of INH leads to the formation of covalent adducts with

the nicotinamide head group of NAD(H) forming the INH-NAD adduct, which is a slow, tight-binding inhibitor of InhA (151). Because a substantial fraction of all clinical isolates that are resistant to INH result from KatG mutations (155-158), compounds that target InhA, but that do not require activation by KatG, are promising candidates for drug-resistant *M. tuberculosis*.



Scheme 2. 1 Formation of INH-NAD adduct.

INH can be activated by either KatG or Mn^{2+} , Mn^{3+} , producing a radical intermediate which in turn forms a covalent adduct with the nicotinamide head group of NAD^+ .

Based on the above hypothesis, we developed a series of diaryl ethers (**Figure 2.1**) that are potent InhA inhibitors with minimum inhibitory concentrations (MICs) 1 – 2 $\mu\text{g/mL}$ against both drug-sensitive and drug-resistant strains of *M. tuberculosis* (159). However, all compounds reported in Ref. 16 are rapid reversible inhibitors of InhA. In our previous studies on enoyl-ACP reductase inhibitors in other pathogens, *in vivo* efficacy of diaryl ether inhibitors correlates with their residence time (t_R) on the enzyme target (160). The importance of incorporating residence time into lead optimization is also highlighted by the fact that INH-NAD adduct was shown to be a slow onset inhibitor of InhA (151). Additionally, slow onset inhibition is coupled to ordering of an active site loop, which leads to the closure of the substrate-binding pocket (161-163).

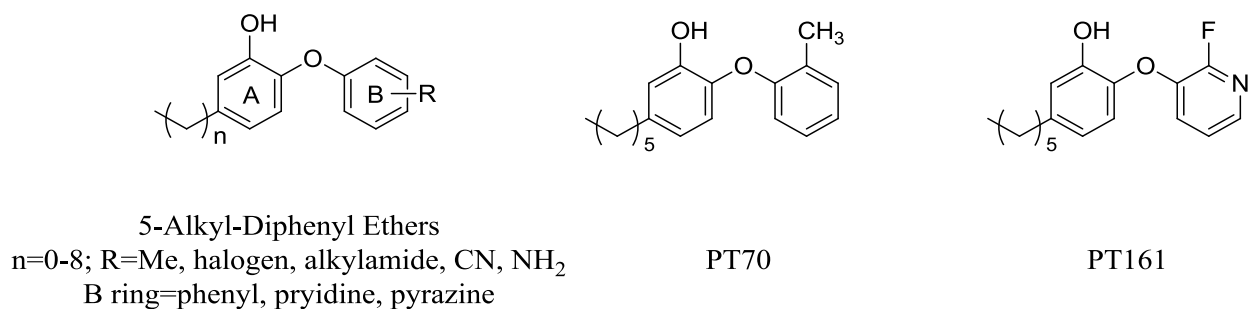
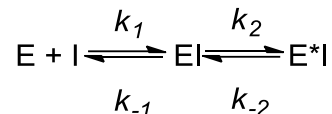


Figure 2. 1 Structures of the diaryl ether scaffold, PT70, and PT161.

The diaryl ethers share a scaffold consisting of an alkyl phenol-A ring and a B-ring with various substituents.

In the efforts of developing slow onset inhibitors of InhA, PT70 was discovered. PT70 binds preferentially to the InhA·NAD⁺ complex and has a residence time of 24 min on the target (161). It binds to the enzyme target through a two-step induced-fit mechanism, in which the rapid formation of the initial EI complex is followed by the slow formation of the final enzyme-inhibitor complex (EI^{*}) (**Scheme 2.2**). Furthermore, PT70 has antibacterial activity in a mouse model of TB infection when delivered by intraperitoneal injection (164). The *in vivo* efficacy of PT70 supports the importance of residence time in this system. PT161 is also a diaryl ether InhA inhibitor. It has a MIC value of 0.3 μM, and a residence time of 107 min (unpublished data). The other important reason to choose PT161 is that it bears a fluorine on its B ring.



Scheme 2. 2 Kinetic scheme for time dependent inhibition.

The time-dependent diaryl ether inhibitors bind through a two-step induced-fit mechanism, in which the rapid formation of the initial EI complex is followed by the slow formation of the final enzyme-inhibitor complex (E^{*}I).

Traditionally, due to the limitation of methodologies to access tissue pharmacokinetics (PK), plasma PK has been widely used as a surrogate to evaluate the exposure of candidate drugs and to compare with their corresponding minimum inhibition concentrations in the expectation to predict *in vivo* efficacies. However, the equilibrium between plasma and target tissue cannot always be taken for granted; drug levels in target tissues are often substantially different from the corresponding plasma levels (106, 113). In the case of antibacterial drugs, failure to reach optimal concentration at target site can not only cause failed therapy but also trigger resistance (165). In order to address these issues, the Food and Drug Administration (FDA) requires target tissue distribution studies at infected and uninfected sites (113).

Positron Emission Tomography (PET) has emerged as a powerful tool and been widely used in creative ways to study drug actions in humans and laboratory animals (166). PET images three-dimensional distribution of drugs non-invasively in real-time, and the methodology can be readily translated into humans (114). Another major benefit of PET imaging is that it is a

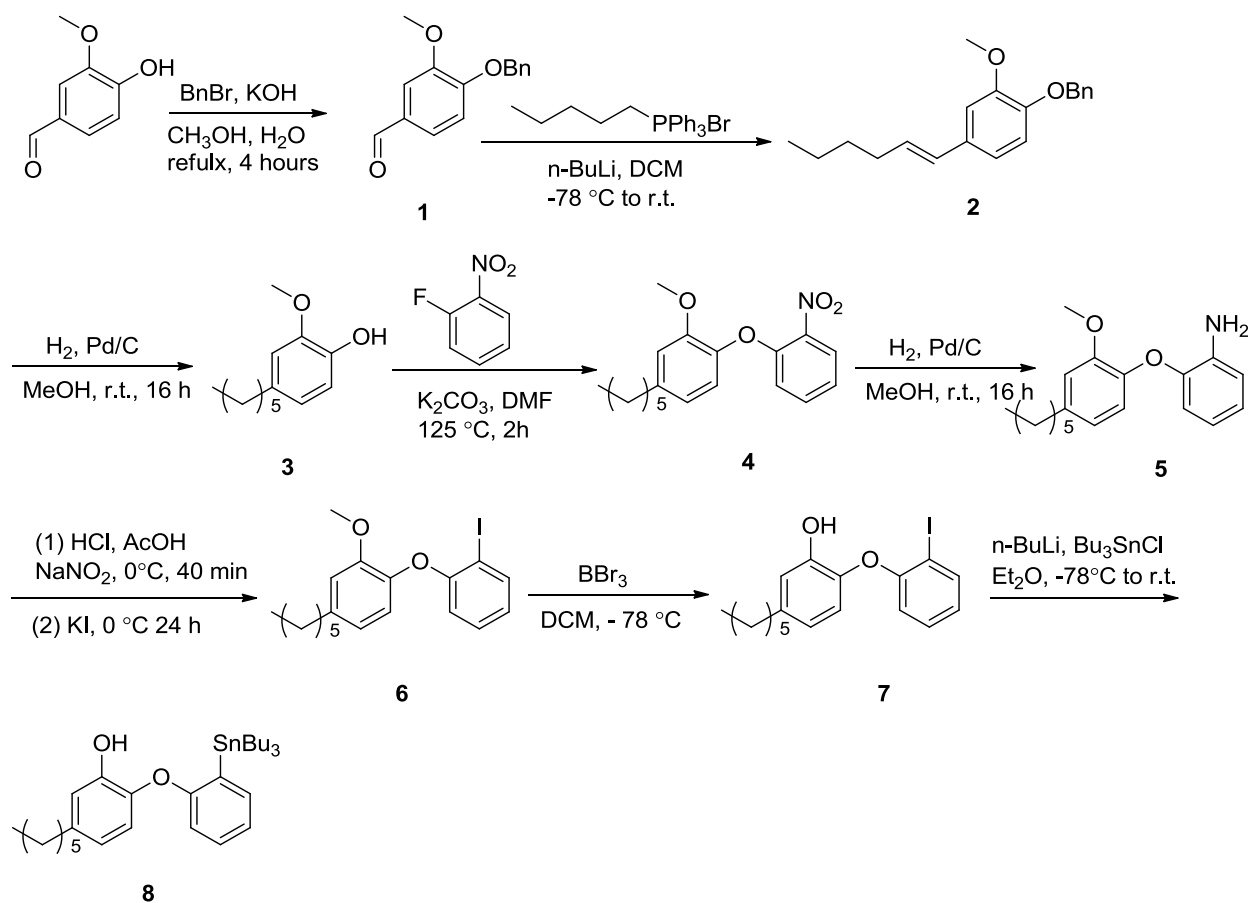
quantitative measurement. Besides the translational potential and quantitative potential, PET can also be used to determine target engagement in human subjects if specific binding of a radiotracer is observed. It is important to determine target engagement because the pharmacological validation of drug action requires verification that chemical probes engage their intended targets *in vivo* (129).

The goal of this study is to develop radiolabelling methods to incorporate short-lived radioisotopes, ^{11}C and ^{18}F , into our drug leads (PT70 and PT161, **Figure 2.1**), then to study their biodistribution and pharmacokinetics in mice using PET. Here we report the radiolabelling of PT70 using ^{11}C (half-life: 20.4 min) and its biodistribution in healthy mice. We also report our efforts to radiolabel PT161 using ^{18}F (half-life: 109.77 min), a more widely used isotope because of its longer half-life.

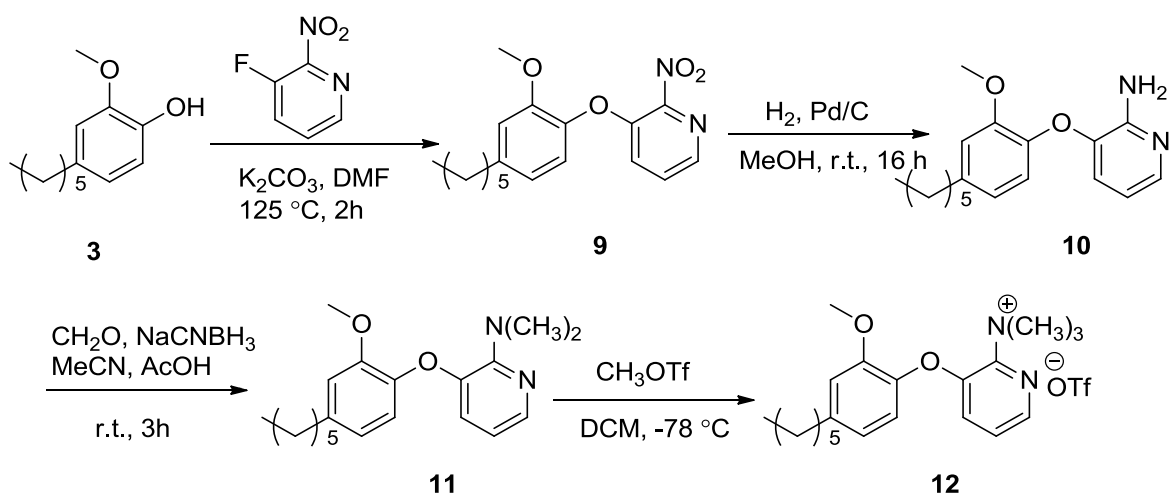
Results and Discussion

Organic Synthesis

The synthesis of the precursor for [^{11}C]PT70 (**8**) was adapted from methods previously described (164). Briefly, compound **3** was prepared from commercially available vanillin through three steps. Vanillin was protected with a benzyl group and coupled with a hexyl chain using a Wittig reaction to form compound **2** (159). Reduction of compound **2** with hydrogen generated compound **3**. Compound **4** was synthesized by nucleophilic aromatic substitution of **3** with 1-fluoro-2-nitrobenzene, and was converted to compound **5** by reduction with H_2 catalyzed by palladium on charcoal. Compound **6** was prepared from **5** by utilizing the Sandmeyer reaction, which went through a diazonium salt intermediate prior to iodide anion attack (167). The deprotection was carried out with tribromoborane in dichloromethane to form **7**, and compound **8** was prepared with additional treatment of tributylchlorostannane on **7** under strong basic condition in diethyl ether (**Scheme 2.3**). In order to synthesize precursor for labelling [^{18}F]PT161 - a trimethylated triflate salt (**12**), compound **3** was coupled to a very similar B ring to yield compound **9**, then compound **9** is reduced to compound **10**, using the same method when preparing for compound **5**. Finally, compound **10** was converted to compound **11** with formaldehyde and Sodium cyanoborohydride via a reductive amination reaction, then got methylated with methyl triflate to yield compound **12** (**Scheme 2.4**).



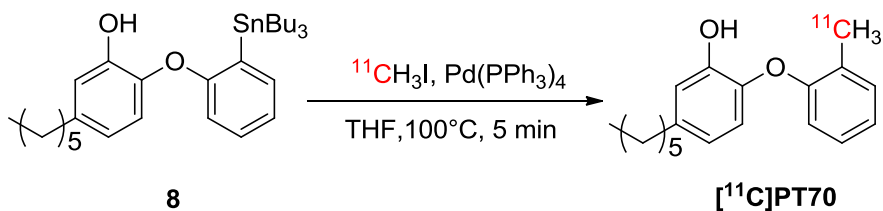
Scheme 2. 3 Synthesis of precursor for [¹¹C]PT70



Scheme 2. 4 Synthesis of precursor for [¹⁸F]PT161

Radiosynthesis of [¹¹C]PT70

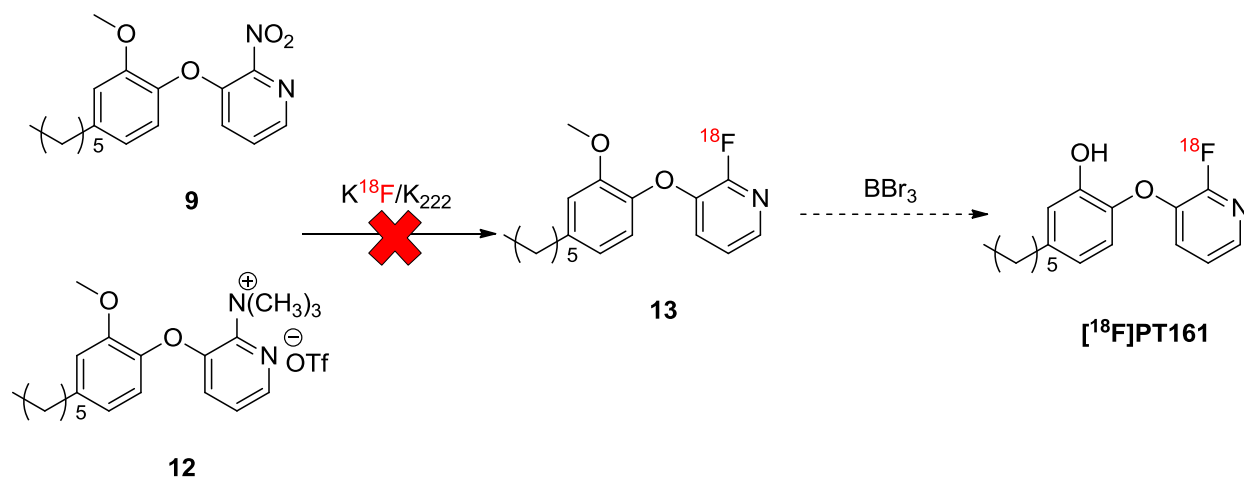
The radiosynthesis of [¹¹C]PT70 was accomplished by using the modified Stille reaction using precursor **8** as shown in **Scheme 2.5** (3). Initially, the reaction was successfully carried out in THF at 100 °C for 10 min. However, this involved a time consuming evaporation procedure before the chromatographic purification due to incompatible solvents and consequently we explored a range of solvent systems in order to identify conditions that would give the required rate, radiochemical yield and solvent compatibility. This screening approach resulted in the use of THF as the solvent with a 5 min reaction time. This reaction was also tolerant of the phenol group and no major side reactions were observed. The [¹¹C]PT70 was subsequently purified by high performance liquid chromatography (HPLC) and concentrated *in vacuo*. The average decay-corrected yield (DCY), calculated from [¹¹C]CH₃I, was 40% - 50% in a total synthesis time of 50 min. Analytical HPLC and TLC demonstrated that the radiolabeled product was over 98% radiochemically pure, with a specific activity of 7 – 13 Ci/μmol at the end of bombardment (EOB).



Scheme 2.5 Radiosynthesis of [¹¹C]PT70

Radiosynthesis of [¹⁸F]PT161

Compound **9** and **12** have both been proposed for use as precursors to radiolabel PT161 with fluorine-18 (**Scheme 2.6**), because both the nitro group and the trimethylammonium triflate salt have been widely used as leaving groups for fluorination reactions (3). In the case of compound **12**, different combinations of solvent and temperature were explored without yielding the desired intermediate compound **13** (**Table 2.1**). Besides conventional heating, microwave reactor also failed (data not shown). One possible reason is that the ether bond deactivates the second benzene ring for the nucleophilic substitution reaction even though the trimethylammonium triflate salt is known to be an excellent leaving group for similar reactions. Another problem is that, the temperature has to be raised in order to overcome the deactivation effect of the ether bond, and this in turn causes decomposition of the precursor. Furthermore, the utility of compound **9** as precursor was also explored (**Scheme 2.6**). In this case, due to the increased stability of compound **9** over **12**, we managed to elevate the reaction temperature to 180 °C and observed product formation with a very similar R_f value with intermediate **13** on TLC scanner. Unfortunately, the formed product was found not to be intermediate **13** on analytical HPLC equipped with both UV and RAD detector (data not shown).



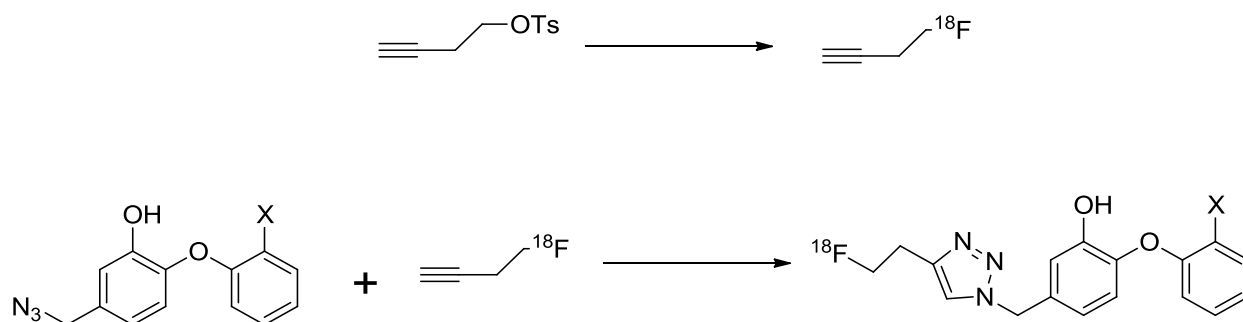
Scheme 2. 6 Proposed radiosynthesis of [^{18}F]PT161

Table 2. 1 Reaction condition screening using compound 10 as precursor

Solvent	Temperature	Yield@	Yield@	Yield@	Yield@	Yield@	Yield@	Decomposition/ byproduct
	(°C)	2min	5min	10min	20min	30min	1h	
DMSO	80			No Product.				No
DMSO	90	N.D.	N.D.	N.D.	1.1%	0.39%	1.79%	No
MeCN	105	0.16%	1.2%	0.73%	N.D.	N.D.	N.D.	Yes
MeCN	130	0.05%	0.04%		Evaporated			Yes
DMSO	130	N.D.	1.99%	2.03%	3.69%	N.D.	N.D.	Yes
DMSO	150	N.D.	0.9%	0.7%	0.6%	N.D.	N.D.	Yes

Alternative strategy for radiolabelling diaryl ethers with fluorine-18

A rapidly expanding methodology for incorporating fluorine-18 into biologically active molecules is to “click” fluorine-18 utilizing Cu-catalyzed azide-alkyne cycloaddition (CuAAC) and several copper-free click reactions (168). Lauren Spagnuolo from our lab designed and synthesized a series of triazole A ring diaryl ethers compounds. These triazole A ring diaryl ethers have long residence times on InhA and have promising MIC value against *M. tuberculosis* (data now shown). Lauren also designed a F18-fluorination method using click chemistry (**Scheme 2.7**) in order to circumvent the harsh conditions for directing fluorination as discussed previously. These fluorine-18 labelled molecules will not only enable the biodistribution determination of the parent compounds in living animals, but also provide promising tools to study drug-target interaction *in vivo*, such as target occupancy and *in vivo* residence time measurement.



Scheme 2. 7 Proposed scheme for radiolabelling diaryl ether compounds with click ^{18}F -fluorination strategy

Biodistribution of [¹¹C]PT70 in mice

Peripheral organ drug distribution was determined in healthy mice (**Table 2.2** and **Figure 2.2**).

For all tissues measured, the highest concentration of drug was measured at 20 min after

injection and decreased at later times. The distribution of [¹¹C]PT70 in blood was also measured.

The distribution of [¹¹C]PT70 in liver is much higher than in other peripheral organs, since the liver is where the drug metabolism occurs.

Table 2. 2 Biodistribution of [¹¹C]PT70 in healthy mice.

	Spleen	Kidney	Liver	Lung	Blood
20 min	1.82 ± 0.28	2.21 ± 0.01	N.D.	1.36 ± 0.17	1.70 ± 0.02
40 min	0.93 ± 0.14	1.45 ± 0.26	15.70 ± 1.22	1.26 ± 0.16	1.46 ± 0.17
60 min	0.21 ± 0.01	0.31 ± 0.03	14.09 ± 0.01	1.35 ± 0.05	0.55 ± 0.14

Values given are [%ID/cc], n = 3.

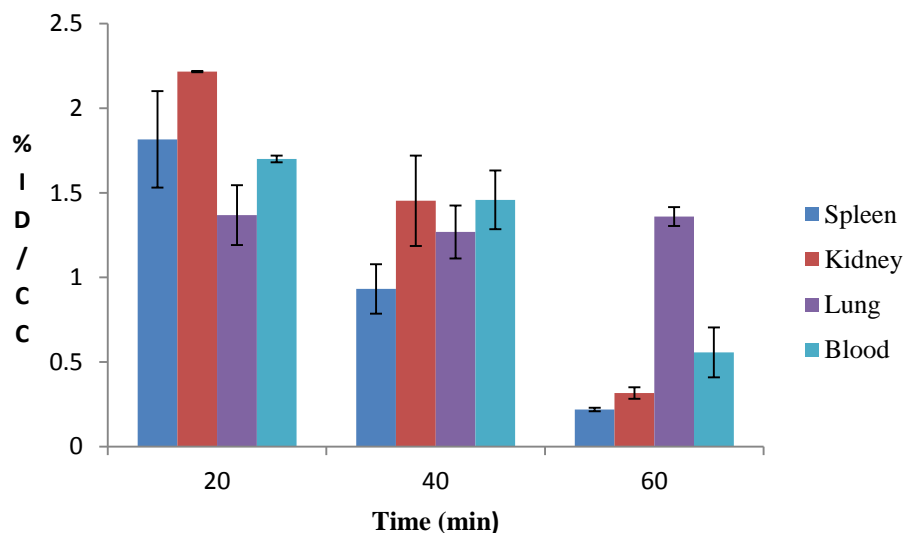


Figure 2. 2 Biodistribution of [¹¹C]PT70 in healthy mice.

Values given are % Injected dose/cc, n = 3. Radioactivity of each organ is counted using a gamma-counter.

Pharmacokinetics (PK) of PT70

The PK parameters that were determined included AUC, C_{max}, T_{max} and t_{1/2} for PT70 following dosing at 10 mg/kg intravenously (**Figure 2.3** and **Table 2.3**). The AUC of PT70, which evaluates drug exposure, was 6.12 h*mg/L when integrated to 24 h. Delivery of PT70 at 10 mg/kg iv resulted in a C_{max} value of 2.19µM with a T_{max} of 1 h. It has been reported that substituted diaryl ethers such as PT70, are subject to both Phase I and Phase II metabolism, including *O*-glucuronidation (169). This known metabolism contributes to the relatively low AUC and short t_{1/2} of PT70.

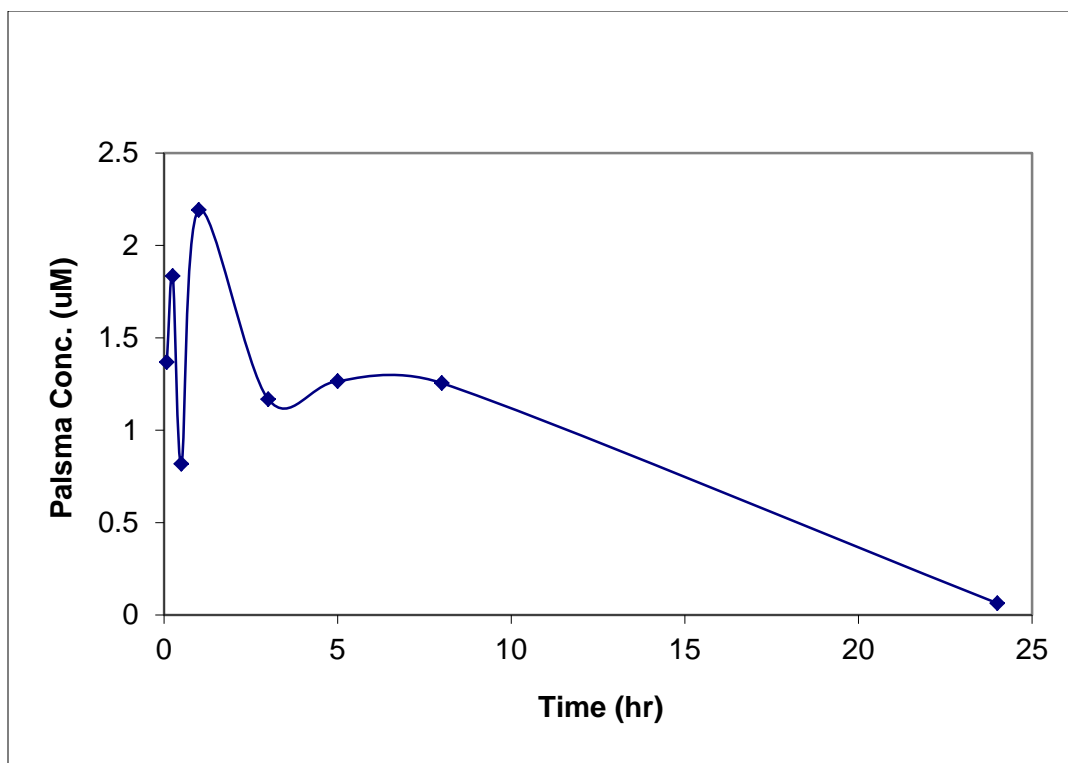


Figure 2. 3 *In vivo* Pharmacokinetics parameters for PT70

The route is i.v. and dose is 10 mg/kg. Plasma concentration ($\mu\text{mol/L}$) is plotted with different time points being measured.

Table 2. 3 *In vivo* Pharmacokinetics parameters for PT70

Parameter	PT70 iv 10 mg/kg
t_{1/2} (h)	4.14
T_{max} (h)	1
C_{max} (μM)	2.19
AUC_{0-t} (mg/L*h)	6.12
MRT_{0-inf_obs} (h)	6.59
Cl_{obs} (mL/min/kg)	26.67
V_{ss} (L/kg)	100

PET imaging of [¹¹C]PT70 in baboon

PET imaging studies in baboon were performed by Dr. Li Liu in Dr. Joanna Fowler's facility at Brookhaven National Laboratory with the help of Dr. Jacob Hooker, and assistance from Dr. Michael Schueller, Youwen Xu, and Colleen Shea. PET imaging studies were performed with [¹¹C]PT70 in baboons to determine their peripheral organ distributions. The time activity curves (TACs, **Figures 2.4**) were generated from the images acquired after i.v. administration to baboons by manually drawing the region of interests (ROIs). [¹¹C]PT70 was administered iv and monitored over the 90 min dynamic PET scan. The injected [¹¹C]PT70 cleared rapidly from the heart, lung and blood, with moderate accumulation in liver and kidney, while a large portion of radioactivity accumulated in the gallbladder (**Figure 2.4**).

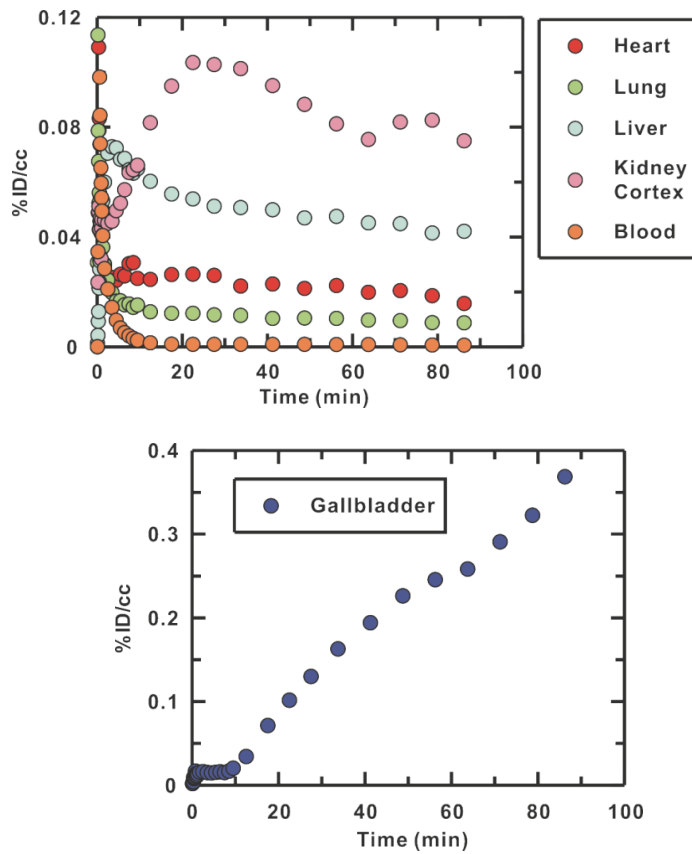


Figure 2.4a. Time-activity curves of [¹¹C]PT70 in major organs

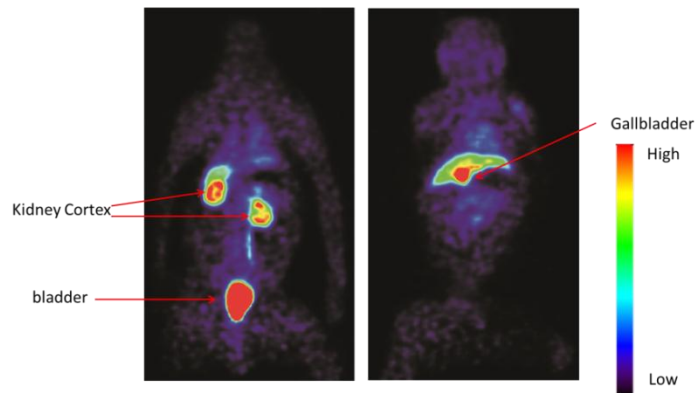


Figure 2.4b. Whole body scan of [¹¹C]PT70

Figure 2. 4 PET imaging of [¹¹C]PT70 in baboon

Images were slices of healthy baboon summed from 0-120 min.

In a prior study, PT70 decreased bacterial load in both primary and secondary site of TB infection (164) in mice, which is supported by the tissue drug distribution data in this study (**Table 2.2** and **Figure 2.2**), that the drug is rapidly distributed into lung and spleen.

Furthermore, the PK and drug distribution data in baboon provide valuable information on organ distribution of this important drug in non-human primates. This study presents a promising model to evaluate pharmacokinetics/pharmacodynamics relationships based on target tissue concentrations.

Materials and Methods

All chemicals were purchased from commercial vendors and used without further purification unless specified. Vanillin and benzyl bromide were purchased from Alfa Aesar. BBr₃, 1-fluoro-2-nitrobenzene, n-BuLi, and t-BuLi were purchased from Sigma-aldrich. Formaldehyde was purchased from Govt Sci.

Organic Synthesis

4-(Benzyloxy)-3-methoxybenzaldehyde (1)

A solution of benzyl bromide (3.93 ml, 33 mmol) was added to the mixture of 4.56 g vanillin (30 mmol) in 50 ml MeOH and 1.85 g KOH (33 mmol) in 50 ml H₂O dropwise and the whole mixture was heated to reflux for 4 hrs. After the completion of reaction, the product was extracted with DCM and H₂O, and the aqueous layer was further washed with DCM. The combined DCM layers were dried with MgSO₄, and concentrated *in vacuo*. The crude product **1** was purified by automated column chromatography with silica gel using 5% ethyl acetate/petroleum ether as the mobile phase. The product was obtained as a white solid with a yield of 52%. ESI-MS calculated for C₁₅H₁₄O₃ [M+H]⁺ m/z = 243, found 243.

1-((4-((E)-hex-1-enyl)-2-methoxyphenoxy)methyl)benzene (2)

A solution of n-BuLi (2M solution in cyclohexane, 6.7 ml, 13.4 mmol) was added dropwise to an solution of n-pentyltriphenylphosphonium bromide (13.4 mmol) in DCM at -78 °C. After 30 min, 2.5 g of **1** (10.3 mmol) was added to the mixture before the cooling bath was removed, and the reaction mixture was stirred overnight. The reaction was subsequently quenched by slowly adding 1M HCl, after which the pH was adjusted to 7 using NaHCO₃

solution. The aqueous layer was extracted with DCM twice and the combined organic layers were washed with brine before drying with MgSO₄. The crude product **2** was concentrated *in vacuo* prior to purification by automated column chromatography with silica gel using 5% ethyl acetate/petroleum ether as the mobile phase. The yield was 75%. ESI-MS calculated for C₂₀H₂₄O₂ [M+H]⁺ m/z = 297, found 297.

4-Hexyl-2-methoxyphenol (3)

Activated palladium on charcoal (200 mg) was added to 50 ml MeOH solution of compound **2** (2.28 g, 7.8 mmol). The reaction mixture was stirred under hydrogen overnight and then filtered through celite. The crude product **3** in the filtrate was concentrated *in vacuo* and purified by automatic column chromatography with silica gel using 5% ethyl acetate/petroleum ether as the mobile phase. The product was a colorless liquid and the yield was 91%. ESI-MS calculated for C₉H₁₂O₂ [M+H]⁺ m/z = 209, found 209.

1-(4-Hexyl-2-methoxyphenoxy)-2-nitrobenzene (4)

A solution of 1.484 g compound **3** (7.1 mmol) and 2.9 g K₂CO₃ dissolved in 5 ml DMF was stirred for 10 min prior to the addition of 1.303 g 1-fluoro-2-nitrobenzene (6.4 mmol). The reaction was heated to 120 °C under N₂ for 2 h before quenching with 50 ml H₂O. The aqueous layer was extracted 3 times with 30 ml diethyl ether and the combined organic layer was washed with 50 ml brine and dried with MgSO₄. The crude product was concentrated *in vacuo* and was used for the next step without purification.

2-(4-Hexyl-2-methoxyphenoxy)benzenamine (5)

Activated palladium on charcoal (200 mg) was added to a solution of compound **4** (2.0 g, 6.1 mmol) in 25 ml of MeOH. The reaction mixture was stirred under hydrogen overnight and then filtered through celite. The crude product **3** in the filtrate was concentrated *in vacuo* and purified by automated column chromatography with silica gel using 5% ethyl acetate/petroleum ether as the mobile phase. The product was colorless liquid and the yield was 89%. ESI-MS calculated for C₁₉H₂₅NO₂ [M+H]⁺ m/z = 300, found 300.

1-(4-Hexyl-2-methoxyphenoxy)-2-iodobenzene (6)

HCl (6M, 6.0 ml) and NaNO₂ (1.5 g) were added to a solution of compound **5** (2g, 6.7 mmol) in 50ml of 50% AcOH/50% H₂O at 0 °C, and the mixture was stirred for 40 min prior to the addition of 4.8 g of KI (28 mmol). After 24 hrs, the reaction quenched with 200 ml solution of 50% DCM/50% H₂O. The organic layer was obtained and the aqueous later was extracted 2 times with DCM. The combined organic layer was dried with MgSO₄ and concentrated *in vacuo*. 1.74 g of crude product was collected and used for next step without purification.

2-(2-Iodophenoxy)-5-hexylphenol (7)

6.3 ml BBr₃ solution (1M, 6.3 ml) was added dropwise to a solution of compound **6** (1.74g, 4.2 mmol) in 10 ml DCM at -78 °C, and the mixture was warmed to room temperature slowly. Before quenching the reaction with 10 ml MeOH, the reaction was cooled to -78 °C. The reaction was dried *in vacuo* and redissolved with 30 ml DCM. Organic layer was washed with NaHCO₃, water and brine sequentially prior to dry with MgSO₄. The crude product was concentrated *in vacuo* and purified by automated column chromatography with silica gel using 4% ethyl acetate/petroleum ether as the mobile phase. The product was yellow liquid and the yield was 81%. ¹H NMR (300 mHZ, = 8.1 Hz, 1H), 6.65 (dd, *J* = 8.1, 2.1 Hz, 1H), 5.51 (s, 1H),

2.56 (t, $J = 7.8$ Hz, 2H), 1.50- 1.62 (br, 2H), 1.21-1.40 (br, 6H), 0.89 (t, $J = 6.6$ Hz, 3H); ESI-MS for $C_{18}H_{21}IO_2$ $[M+H]^+$ $m/z = 395$, found 395.

2-(2-(Tributylstannyl)phenoxy)-5-hexylphenol (8)

t-BuLi (2M solution in cyclohexane, 1.14 ml, 2.28 mmol) was added dropwise to a solution of **7** (300mg, 0.76 mmol) in 10 ml dry diethyl ether at -78 °C. The mixture was stirred for 30 min prior to the dropwise addition of tributylchlorostannane (0.818 ml, 3.04 mmol). The reaction was stirred at -78 °C and allowed to warm to room temperature overnight. The reaction was then quenched with 0.1 M phosphate buffer (pH 7) at -78 °C, and 100 ml 50% diethyl ether/50% H_2O was added. The organic layer was collected and the aqueous layer was extracted with additional diethyl ether.. The combined organic layers were dried over $MgSO_4$, and the solvent was removed *in vacuo*. The crude product was purified by automated column chromatography with silica gel using 1% triethylamine/4% ethyl acetate/95% petroleum ether as the mobile phase. The product was a yellow oil and the recovered yield was 25%. 1H NMR (300 mHZ, $CDCl_3$) δ 7.48 (dd, $J = 7.2, 1.8$ Hz, 1H), 7.22-7.28 (m, 1H), 7.08-7.12 (m, 1H), 6.88 (d, $J = 2.1$ Hz, 1H), 6.74 (dd, $J = 7.5, 2.4$ Hz, 2H), 6.64 (dd, $J = 8.4, J = 2.1$, 1H), 5.35 (s, 1H), 2.56 (t, $J = 7.5$ Hz, 2H), 1.47-1.63 (br, 8H), 1.24-1.36 (br, 12H), 1.04-1.10 (br, 6H), 0.84-0.92 (br, 12H); ESI-MS for $C_{30}H_{48}O_2Sn$ $[M+H]^+$ $m/z = 599$, found 599.

3-(4-ethyl-2-methoxyphenoxy)-*N,N*-dimethylpyridin-2-amine (11)

Compound **10** (200 mg, 0.66 mmol) was dissolved in 20 mL acetonitrile. Then 600 μ L formaldehyde (37% in H_2O , 13.2 mmol) and sodium cyanoborohydride (280 mg, 4.4 mmol) were added to reaction mixture. After stirring at room temperature for 5 min, AcOH (300 μ L, 4.4

mmol) was added dropwise into the flask over 10 min. The reaction was stirred at room temperature for 3 h. The reaction was then stopped. The pH of the solution was adjusted to 8, and then 100 ml DCM/H₂O was added. The organic layer was collected and the aqueous layer was extracted with additional DCM. The combined organic layers were dried over MgSO₄, and the solvent was removed *in vacuo*. The crude product was purified by automated column. ¹H NMR (400 MHz, CDCl₃): δ 7.65 (dd, *J* = 3.0, *J* = 1.6, 1H), 7.21 (dd, *J* = 8.0, *J* = 1.5, 1H), 7.03 (d, *J* = 8.0, 1H), 6.86-6.94 (m, 1H), 6.74-6.83 (m, 2H), 3.74 (s, 3H), 2.9 (s, 6H), 2.6 (t, *J* = 8.0, 2H), 1.58-1.69 (br, 2H), 1.28-1.38 (br, 6H), 0.82-0.94 (br, 3H); ¹³C NMR(400MHZ, CDCl₃): δ = 156.1, 151.1, 140.6, 140.2, 138.3, 136.9, 125.2, 122.6, 120.5, 118.2, 112.8, 55.6, 42.5, 35.8, 31.6, 31.3, 28.9, 22.5, 13.9 ppm; ESI-MS for C₂₀H₂₈N₂O₂ [M+H]⁺ *m/z* = 329, found 329.

3-(4-ethyl-2-methoxyphenoxy)-N,N,N-trimethylpyridin-2-aminium triflate (12)

Compound **11** (330 mg, 0.99 mmol) was dissolved in 10 mL CH₂Cl₂. The temperature of the solution was reduced to -78°C and methyl triflate (179 mg, 1.09 mmol) was then added slowly. Subsequently, the reaction was warmed to room temperature and maintained at room temperature for 24 hrs after which the solvent was removed by rotary evaporation. The crude product was purified by automated column chromatography with silica gel using 10% MeOH/95% CH₂Cl₂. ¹H NMR (400MHZ, CDCl₃): δ 8.29 (d, *J* = 8.0, 1H), 8.19 (d, *J* = 4.0, 1H), 7.21-7.26 (m, 1H), 7.10 (d, *J* = 8.0, 1H), 6.78-6.90 (m, 2H), 3.90 (s, 9H), 3.67 (s, 3H), 2.6 (t, *J* = 8.0, 2H), 1.60-1.68 (br, 2H), 1.29-1.36 (br, 6H), 0.87-0.91 (br, 3H); ¹³C NMR(400MHZ, CDCl₃): δ = 154.62, 150.31, 149.20, 142.65, 138.03, 131.71, 128.92, 122.85, 120.74, 119.70, 112.63, 55.92, 55.94, 35.98, 31.66, 31.31, 29.00, 22.57, 14.06 ppm; ESI-MS for C₂₁H₃₁N₂O₂ [M+H]⁺ *m/z* = 343, found 343.

Radiosynthesis of [¹¹C]PT70

The synthesis of [¹¹C]PT70 was performed using organotin or stannanes **6** as the precursor. The precursor (1.0 mg) was dissolved in 0.3 ml THF with 2 mg tetrakis(triphenylphosphine)palladium(0). After [¹¹C]CH₃I was purged into the solution and trapped at 0 °C, the reaction vessel was sealed and heated at 100°C for 5 min in an oil bath. The reaction mixture was diluted with 1 ml of aqueous ammonium formate (0.1M) prior to loading onto a semi-preparative HPLC column. HPLC purification was performed using a reverse phase PFP column (Phenomenex, Luna PFP 250×10, 5 μm), at a 5 ml/min flow rate with a mobile phase consisting of 68% MeCN/32% aqueous ammonium formate (0.1 M). The product was collected at the expected retention time (17 min) and the solvent was removed by rotary evaporation. After dilution with 4 ml saline with 1 ml sterile alcohol, the solution was filtered through an Acrodisc 13-mm Syringe Filter with 0.2 μm Supor membrane (Pall Corporation, Ann Arbor, MI) into a sterile vial for delivery. Radiochemical purity was determined by reverse-phase analytical HPLC using a Phenomenex, Luna PFP, 250×4.6, 5 μm column operated at 1.0 ml/min flow rate using a mobile phase of 70% MeCN/30% water, with 10 min retention time. Subsequently, purity was verified using TLC (5% EA/95% HE, R_f = 0.45) by co-spotting the labeled product with a standard.

Radiosynthesis of [¹⁸F]PT161

Aliquots of aqueous [¹⁸F]KF which has been delivered from the cyclotron was added into a Reacti-Vial preloaded with 5 mg Kryptofix 2.2.2 and 1 mg K₂CO₃. The solution was azeotropically dried with additional aliquots of MeCN at 105°C. A solution of **9** or **12** (2 mg

dissolved in 300 μ L MeCN) was added to the Reacti-Vial containing the dried fluorine-18 residue. After sealing, the Reacti-Vial was heated to temperature indicated in **Table 2.1** for various time points and then quenched by the addition of 3 ml cold H₂O. The product formation of intermediate **13** was monitored by TLC (20% EA/95% HE, R_f = 0.62) equipped with both UV and RAD detector by co-spotting the labeled product with a standard.

Pharmacokinetics of PT70

The pharmacokinetics (PK) of PT70 was conducted in healthy Swiss Webster mice. The administration route used in this study is iv (10 mg/kg). After a single drug administration, blood samples were collected at 5 min, 15 min, 30 min, 1 h, 2 h, 4 h, 7 h and 24 h (n = 3). Each mouse was bled at two consecutive time points via retro – orbital bleeding and cardiac puncture, respectively, and ethylenediaminetetraacetic acid (EDTA) was used as the anticoagulant. Whole blood samples were centrifuged, and the plasma that resulted was treated with acetonitrile to precipitate the plasma proteins. After an additional centrifugation step, the supernatant was collected for LC-MS/MS analysis. The plasma concentration of PT70 from was calculated and analyzed using PK analysis software WinNonlin (NCA model).

Conclusions

In summary, a novel time-dependent InhA inhibitor, PT70, with long residence time and *in vivo* efficacy against *M. tb* infected mice, has been labeled with the positron emission isotope carbon-11. [¹¹C]PT70 was synthesized using one-step modified Stille reaction, purified and formulated within 1 h, with over 98% radiochemical purity determined by HPLC. Biodistribution and PK of PT70 were determined in healthy mice. The tissue distribution of the drug resulted in efficacy for both primary and secondary infected organs in *M. tuberculosis* infected mice. Furthermore, we explored different radiolabelling routes for PT161, another time-dependent diaryl ether InhA inhibitor. Although current efforts didn't allow the incorporation of fluorine-18 into diaryl ether inhibitors, a click-chemistry strategy has been proposed as an alternative route.

Chapter 3 Radiosynthesis, Pharmacokinetics and Pharmacodynamics of a Novel Enoyl-ACP Inhibitor in *Staphylococcus aureus*-infected Mice

This chapter is based on the work that has been published in:

Wang, H.; Lu, Y.; Liu, L.; Alexoff, D.; Kim, S. W.; Fowler, J. S., and Tonge, P. J.

“Radiosynthesis and biological evaluation of Novel Enoyl-ACP Reductase Inhibitor for *Staphylococcus aureus*”. European Journal of Medicinal Chemistry. 2014, 88(17): 66 -73.

Introduction

Target tissue pharmacokinetics (PK), the link between plasma PK and drug effects (106), has emerged as an important facet in drug discovery and development. Although plasma PK is often used as a surrogate for tissue PK, the equilibrium between plasma and target tissue cannot always be achieved; drug levels in target tissues are often substantially different from the corresponding plasma levels (106, 113). In the case of antibiotic compounds, suboptimal tissue drug concentrations resulting from estimates based on plasma PK, can not only lead to therapeutic failure but also trigger bacterial resistance (165). Thus, current Food and Drug Administration (FDA) guidelines require tissue drug distribution studies at infected and uninfected sites (113). Positron emission tomography (PET), which images drugs and other molecules labeled with positron-emitting isotopes (primarily nitrogen, oxygen, carbon, and fluorine), has been applied in creative ways to study drug action directly in humans and

laboratory animals (166). In addition, the methodology developed for studying drug distribution in laboratory animals using PET can be readily translated to humans (114).

Staphylococcus aureus is a highly infectious pathogen that is carried by 30% of healthy people, usually in the anterior nasal cavities. It is the most common causative agents of nosocomial infections and is readily transferred to immunocompromised patients and causes post-surgical wound infections (170-172). *S. aureus* is able to acquire resistance to antibiotics rapidly, and methicillin-resistant strains (MRSA) emerged only one year after the introduction of this antibiotic in 1959 (173). MRSA infection has spread in the past few decades and is treated by vancomycin, the “drug of last resort” (174). Unfortunately, vancomycin-resistant strains (VRSA) were isolated in June 2002 (175) and there is therefore an urgent need to continuously discover new drugs to combat *S. aureus*.

The type II fatty acid biosynthesis pathway (**Figure 3.1a**), which is usually found in plants and bacteria, is responsible for the *de novo* production of lipids for incorporation into the bacterial cell membrane (176). The final step in fatty acid elongation is catalyzed by the enoyl-ACP reductase enzyme, which has emerged as an attractive drug target in those pathogens that contain the FabI homologue (177). Isoniazid (**Figure 3.1b**), a front-line tuberculosis prodrug, is known to target InhA, the FabI homologue in *Mycobacterium tuberculosis* (151) while triclosan (**Figure 3.1b**), a diphenyl ether inhibitor of the *S. aureus* FabI (saFabI), is recommended as a topical antiseptic to reduce MRSA skin colonization (178). Furthermore, three separate saFabI inhibitors are currently in clinical trials for treating infection caused by drug-resistant *S. aureus* (179-181).

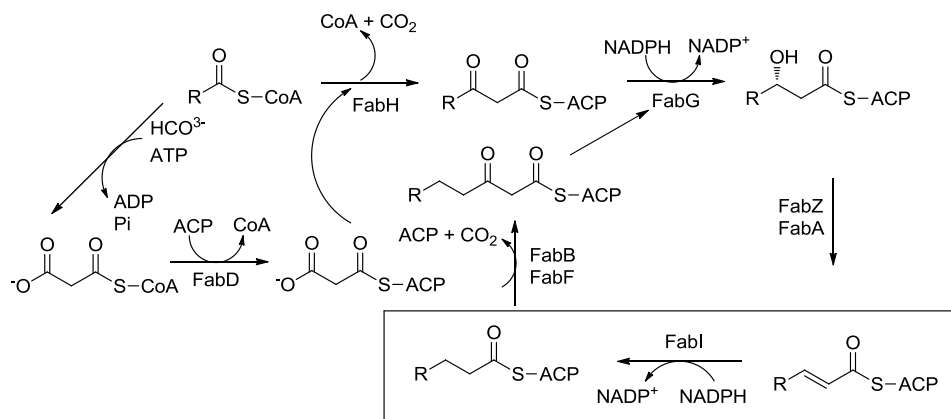


Figure 3. 1a Fatty acid biosynthesis pathway in *S. aureus*.

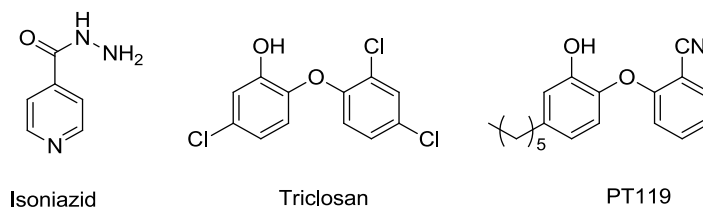


Figure 3.1b Examples of FabI inhibitors.

We recently reported a series of 20 diphenyl ether saFabI inhibitors in which explored the SAR for long residence time inhibition of saFabI (182). Residence time is defined as the reciprocal of the enzyme-inhibitor dissociation rate constant, and is a promising early stage indicator of *in vivo* drug efficacy (160). Our most potent compound PT119 (Fig. 1b; $K_i = 0.01$ nM) has a residence time of 750 min because of its favorable interactions with the enzyme (182). It also shows a promising Minimum Inhibitory Concentration (MIC) value of 0.5 $\mu\text{g/mL}$ against *S. aureus* (unpublished data).

Herein, we report the radiolabeling of our lead compound PT119 with carbon-11 (half life: 20.4 min) to evaluate its biodistribution in both healthy and *S. aureus* infected mice. We also report

the PK of PT119 by both intravenous and subcutaneous routes. Furthermore, we report the *in vivo* efficacy of PT119 in two different infection models.

Materials and Methods

General

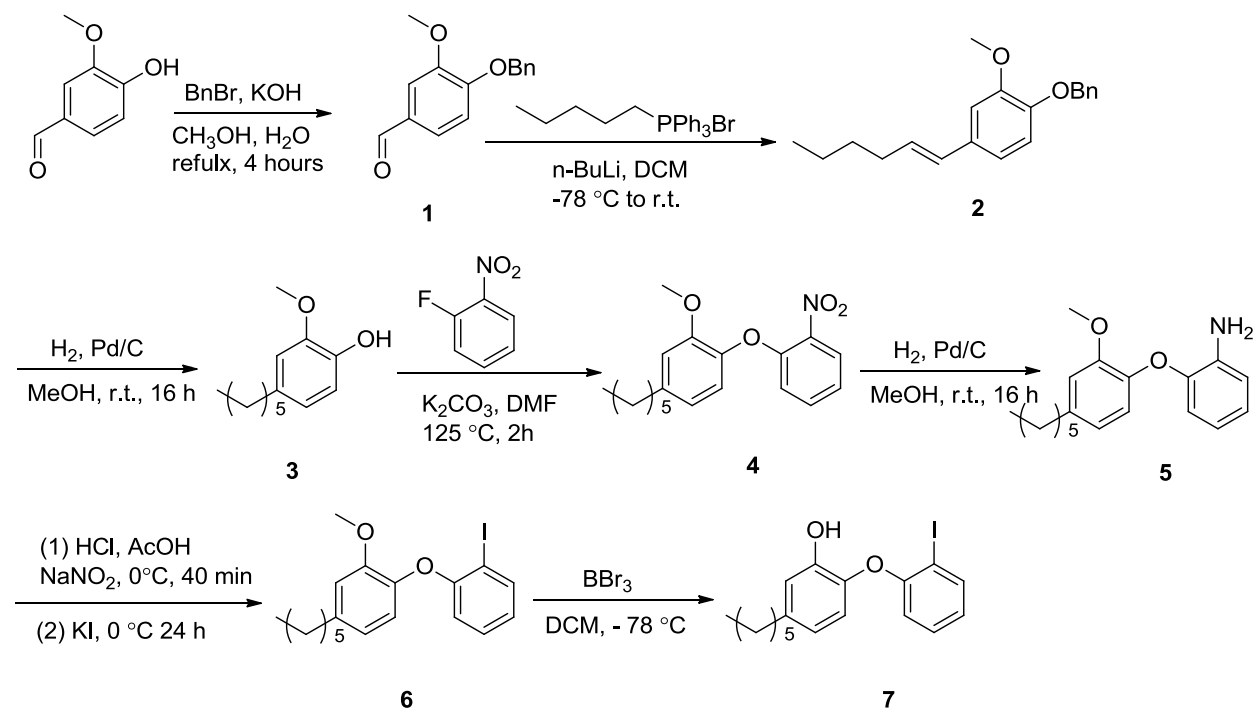
All chemicals used in the study were purchased from commercial vendors and were used without further purification except where stated. Vanillin and benzyl bromide were purchased from Alfa Aesar. BBr₃, 1-fluoro-2-nitrobenzene, n-BuLi, and t-BuLi were purchased from Sigma-aldrich.

[¹¹C]HCN was generated from [¹¹C]CO₂ using a custom-built automated synthesis unit (183). Briefly, [¹¹C]CO₂ was obtained from proton bombardment of a N₂/O₂ target (¹⁴N(p,α)¹¹C) using an EBCO TR 19 cyclotron (Advanced Cyclotron System Inc., Richmond, Canada) and trapped on molecular sieves with an embedded Ni catalyst. The trapped [¹¹C]CO₂ was heated to 350 °C with H₂ on nickel catalyst to produce [¹¹C]CH₄. Subsequent reaction of [¹¹C]CH₄ and NH₃ was catalyzed by platinum at 950 °C and produced [¹¹C]HCN, which was carried by a stream of argon into a shielded hot cell for radiosynthesis.

Analytical and preparative high performance liquid chromatography (HPLC) were performed using a Knauer HPLC system (Sonntek Inc., Woodcliff Lake, NJ, USA) equipped with a model K-5000 pump, a Rheodyne 7125 injector, a model 87 variable wavelength monitor, and a NaI radioactivity detector. Specific activity was determined by measuring the radioactivity and the mass; the latter was derived from a standard curve (UV absorbance at 254 nm by peak area) after HPLC injection of different quantities of the authentic reference compound. The purities of the intermediate and final products were >95%.

Chemistry – synthesis of reference PT119 and precursor for labelling

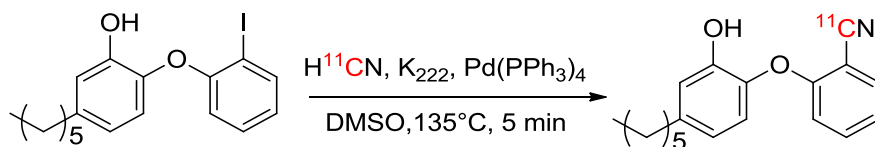
The synthesis of the reference compound PT119 has been described previously (164). Precursor **7** was synthesized by multistep organic synthesis (**scheme 3.1**). First, vanillin was protected with a benzyl group and coupled with a hexyl chain using a Wittig reaction to form compound **2**, after which hydrogenation was used to generate compound **3**. Compound **4** was synthesized by nucleophilic aromatic substitution of **3** with 1-fluoro-2-nitrobenzene, and was converted to compound **5** by reduction with H₂ catalyzed by palladium on charcoal. Compound **6** was prepared from **5** by utilizing the Sandmeyer reaction, which proceeded through a diazonium salt intermediate prior to iodide anion attack. The deprotection was carried out with tribromoborane in dichloromethane to form **7**.



Scheme 3. 1 Synthesis of reference PT119.

Radiosynthesis of [¹¹C]-PT119

The synthesis of [¹¹C]PT119 was performed using the iodo-precursor **7**. The precursor **7** (1.0 mg), K₂₂₂(0.2 mg) and tetrakis (triphenylphosphine) palladium (0) (2.0 mg) was placed in a vial with 0.2 ml DMSO and heated slightly until all the solid dissolved. This solution was then added to [¹¹C]HCN that had been purged and trapped in 0.15 ml DMSO. The reaction solution was sealed in a reaction vial and heated at 135 °C for 5 min in an oil bath. The reaction was quenched by the addition of 1 ml water and the mixture was filtered through celite prior to injection onto a reverse phase PFP semi-preparative column (Phenomenex, Luna PFP 250×10, 5 μm), at a 5 mL/min flow rate with a mobile phase consisting of 70% MeCN/30% aqueous ammonium formate (0.1 M). The product was collected at the expected retention time (10 min) based on a standard and the solvent was removed by rotary evaporation. After dilution with 1mL sterile alcohol plus 4 mL saline, the solution was filtered through an Acrodisc 13-mm syringe filter with 0.2 μm Supor membrane into a sterile vial for delivery. Radiochemical purity was determined by reversed-phase analytical HPLC using a Phenomenex, Luna PFP, 250×4.6, 5 μm column operated at 1.0 mL/min flow rate using a mobile phase of 70% MeCN/30% H₂O, with 10 min retention time. Subsequently, purity was verified using TLC (5% EA/95% HE, R_f = 0.4) by co-spotting the labeled product with a standard.



Scheme 3. 2 Radiosynthesis of [¹¹C]PT119.

Uptake of [¹¹C]PT119 in *S. aureus* cells

[¹¹C]PT119 and [¹⁸F]FDG were incubated with *S. aureus* suspended in PBS buffer containing 2% brain-heart-infusion broth. In each Eppendorf vial, 2.5×10^7 CFU of *S. aureus* were exposed to 30 μ Ci [¹¹C]PT119 or 13 μ Ci of [¹⁸F]FDG. The mixture was incubated at 37 °C in a shaking water bath. The background group was incubated without bacteria. In competition studies, the uptake of [¹¹C]PT119 and [¹⁸F]FDG was challenged with cold PT119 and D-glucose, respectively. For this purpose, the cells were preincubated with 2.5 μ g/ml cold PT119 or 10 mg/ml D-glucose at 37 °C for 30 min. An aliquot of 1 mL incubation mixture was taken out at 20, 40, 60, 90, 120 min in triplicate. Then, the cell pellets were centrifuged and washed with PBS buffer twice to get rid of extracellular radioactivity. The radioactivity was determined in a well counter. After correction for background activity, results are reported as the mean percentages of radioactivity associated with the cell compared with the total radioactivity added.

Infection models

All animals used in this study were maintained in accordance with the American Association for Accreditation of Laboratory Animal Care criteria. The experimental protocol was approved by the Institutional Animal Care and Use Committees (IACUC) at Stony Brook University and Brookhaven National Laboratory.

Six-week old, specific pathogen free, male Swiss Webster mice weighing 28 to 32 g were purchased from Taconic and housed in the Division of Laboratory Animal Resources (DLAR) at Stony Brook University under Biosafety Level - 2 (BSL - 2) conditions. All mice were given *ad*

libitum access to food and water throughout the entire study. Prior to infection, mice were rendered neutropenic by treatment with cyclophosphamide on day -4 (150 mg/kg) and day -1 (100 mg/kg) via intraperitoneal injection (ip).

Bacterial stocks were freshly prepared before inoculation. In general, MRSA strain BAA1762 was cultured in Mueller Hinton broth at 37 °C to mid log phase ($OD_{600} = 0.45$, 2×10^8 cells/ml). Bacterial cells were harvested by centrifugation (11,000 rpm, 3 min) and washed with sterilized brain heart infusion (BHI) broth. Final inoculums were generated by diluting bacteria to the desired concentrations in BHI broth. Two infection models were used in this study, a systemic infection model and a thigh muscle infection model. To induce systemic infection, mice were injected with 2×10^7 bacterial cells (2×10^8 cells/mL inoculum, 100 μ L) intraperitoneally. Thigh infections were established by injecting 5×10^5 bacterial cells (10^7 cells/mL inoculum, 50 μ L) into the left thigh muscles of mice.

In vivo antibacterial efficacy of PT119

In order to determine *in vivo* efficacy, PT119 was formulated in a mixed solvent consisting ethanol/PEG-400/saline (40/20/40). In the systemic infection study, PT119 (100 mg/kg) was given by subcutaneous (sc) injection on day 0 (1 hour post infection), day 1 and day 2 with a 24 hour administration interval. The same dose of PT119 was administered each time. A group of infected mice treated with vehicle was used as a negative control whereas another group of healthy mice treated with vehicle was used as positive control. Survival was assessed twice a day after infection for 7 days in total and dead animals were removed as soon as they died. Survivors of the study were euthanized by CO₂ inhalation as recommended by the American Veterinary

Medical Association (AVMA) guidelines on euthanasia. In the thigh muscle infection model, a single dose of PT119 (15, 40, 100 mg/kg) was given sc 1 hour post infection. A group of infected mice treated with vehicle was used as negative control. All mice were euthanized by CO₂ inhalation 24 hours post infection. Muscle tissue from the infected thighs was collected and homogenized in 1 mL of saline. Bacterial load was determined by counting colony forming unit (CFU) of serial dilutions on MH II-sheep blood agar plates.

PK of PT119

The pharmacokinetics (PK) of PT119 was conducted in healthy Swiss Webster mice. Two administration routes, iv (10 mg/kg) and sc (40 mg/kg), were studied. After a single drug administration, blood samples were collected at 5 min, 15 min, 30 min, 1 h, 2 h, 4 h, 7 h and 24 h (n = 3). Each mouse was bled at two consecutive time points via retro – orbital bleeding and cardiac puncture, respectively, and ethylenediaminetetraacetic acid (EDTA) was used as the anticoagulant. Whole blood samples were centrifuged, and the plasma that resulted was treated with acetonitrile to precipitate the plasma proteins. After an additional centrifugation step, the supernatant was collected for LC-MS/MS analysis. The plasma concentration of PT119 from each administration route was calculated and analyzed using PK analysis software WinNonlin (NCA model). The bioavailability of sc administration was determined after dosing normalization.

Biodistribution of [¹¹C]-PT119

The *in vivo* biodistribution of [¹¹C]PT119 was determined in healthy mice and in both systemic infection and thigh infection models. In brief, mice were anesthetized using isoflurane and stabilized in a mouse restrainer. Approximately 100 µCi of [¹¹C]PT119 in 50 – 200 µl ethanol/saline (1/3, v/v) was administered using the lateral tail vein. Treated mice were returned to their home cages, allowed to recover from anesthesia and were free to move during the uptake period. Mice were euthanized by cervical dislocation at different time points. In the systemic infection group, infected mice as well as healthy control mice were sacrificed at 20 min, 40 min and 60 min. The carcasses were dissected immediately and organs of interest (spleen, lung, liver and kidney) were harvested. Blood samples were collected by cardiac puncture. Tissue or blood samples were transferred into glass vials, weighed and counted using a well counter (Picker, Cleveland, OH). In the thigh infection group, infected mice and healthy control mice were euthanized at 15 min, 30 min, 45 min and 60 min. Muscle tissue from both thighs, as well as blood, were collected, weighed and counted. Radioactivity values are given as the percentage of total injection dose/g (%ID/g) and are expressed as the mean ± standard deviation (SD, n=3).

Results

Radiosynthesis of [^{11}C]PT119

The radiosynthesis of [^{11}C]PT119 was accomplished by a one-step tetrakis (triphenylphosphine) palladium (0) catalyzed cyanation (**scheme 3.2**). This method was adapted from the previously reported radiolabeling of an aromatic ring with [^{11}C]HCN(184), and involved reaction with [^{11}C]HCN in DMSO for 5 min at 135 °C. The reaction mixture was subsequently purified by HPLC and fractions from HPLC were concentrated *in vacuo* to generate the dry product. Analytical HPLC and TLC demonstrated that the product was over 98% radiochemically pure with a specific activity of 0.5 – 0.8 Ci/ μmol at the end of cyclotron bombardment (EOB). The total synthesis time was 50 min.

Uptake of [^{11}C]PT119 in *S. aureus* cells

The results of the *S. aureus* uptake studies is presented in **Figure 3.2**. The radioactivity associated with the cells decreased for [^{11}C]PT119 and increased for [^{18}F]FDG. In the competition group, no clear difference was observed for PT119 between with and without cold PT119 while binding of [^{18}F]FDG decreased significantly after competition with *D*-glucose. The reason for the decrease of [^{11}C]PT119 binding could be intracellular metabolism. The binding of [^{11}C]PT119 did not change significantly, probably because the binding sites were not saturated by the cold compounds.

The results suggest that both PT119 and FDG are taken up by *S. aureus* cell. However, we could not conclude decisively from this preliminary data whether the activity was intracellular or not. We speculated that the compound may have penetrated the cell membrane, for the fact that the washing of the cells did not remove the remaining radioactivity.

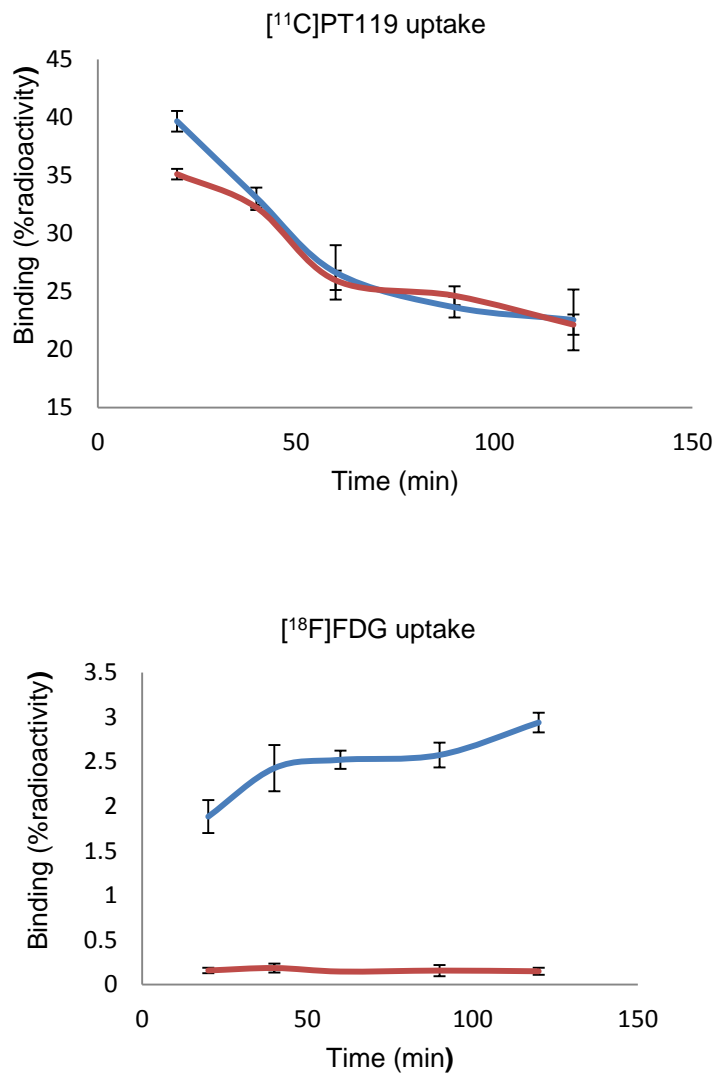


Figure 3. 2 [¹¹C]PT119 and [¹⁸F]FDG uptake of *S. aureus* cells, experimental group (blue) and competition group (red).

Validation of *S. aureus* thigh infection model for PET imaging

Mouse muscle thigh infection model is a standard preclinical model for both PD effects evaluation of drug candidates and nuclear imaging studies for identifying bacterial infection tracer. In a previous study, Welling et al reported that T/NT ratio (infected thigh/uninfected thigh) of [¹⁸F]FDG in *S. aureus* mice thigh infection model is 2.3 – 2.6 (185). However, we did not observe accumulated [¹⁸F]FDG in the infected thigh when we first tried this animal model as shown in **Figure 3.3a**. We hypothesized that the bacteria burden is too high and the resulted necrosis has blocked the blood flow into the infected thigh. Therefore, we decreased the bacteria burden for inoculation to 10⁷ CFU. As a result, [¹⁸F]FDG accumulated in the left thigh (the infected one) as shown in **Figure 3.3b**. Furthermore, we did a quantitative analysis by counting radioactivity in the thighs (**Figure 3.4** and **Table 3.1**), the results showed that the thigh infection model has been validated with a maximum T/NT ratio 1.28 at 20 min after administration of [¹⁸F]FDG ($p < 0.005$).

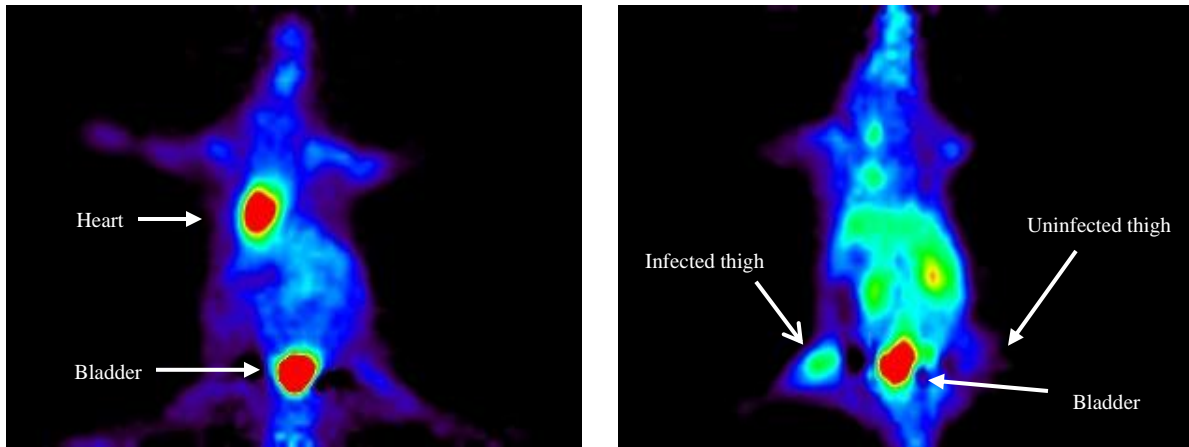


Figure 3.3 [¹⁸F]FDG imaging of *S. aureus* thigh infection model (slice, not projection, summed from 0-120 min).

In Figure 3.3a, [¹⁸F]FDG did not accumulate in the infected thigh because of excess inflammation and limited blood flow; In Figure 3.3 b, [¹⁸F]FDG accumulated in the infected thigh after the inoculation load of bacteria decreased to 10⁷ CFU.

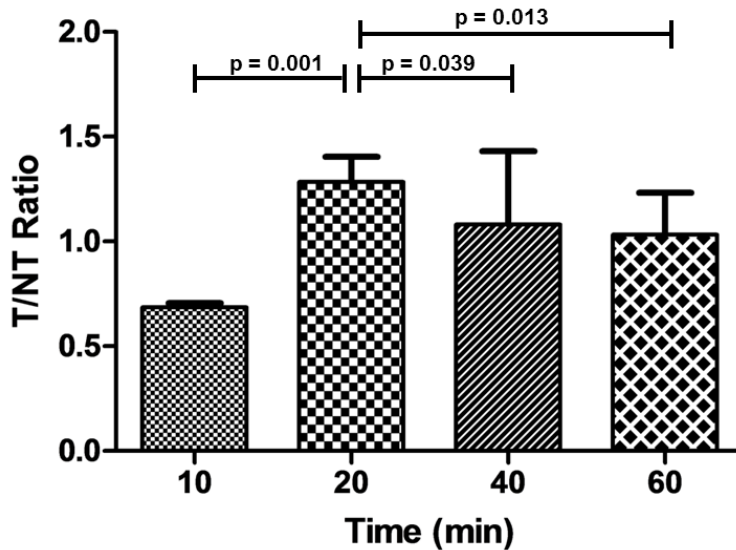


Figure 3.4 Quantitative analysis of T/NT ratio (infected/uninfected) for [¹⁸F]FDG in *S. aureus* thigh infected model.

Table 3. 1 Quantitative analysis of T/NT (infected/uninfected) ratio for [¹⁸F]FDG in *S. aureus* thigh infected model.

Time (min)	Ratio
10	0.69 ± 0.02
20	1.28 ± 0.09
40	1.08 ± 0.28
60	1.03 ± 0.16

Biodistribution of [¹¹C]PT119 in thigh infected mice

In the *S. aureus* thigh infection model, the distribution patterns of [¹¹C]PT119 in the infected thigh, healthy thigh and blood were found to be similar (**Figure 3.5** and **Table 3.2**). There was no significant difference between infected thigh and healthy thigh, which suggests that *S. aureus* infection does not change the biodistribution of PT119. The distribution of [¹¹C]PT119 between the thighs and serum was also similar, indicating rapid equilibration of PT119 between these two compartments.

Table 3. 2 Biodistribution in thigh infection model.

	Healthy thigh	Infected thigh	Blood
15 min	0.98 ± 0.21	0.89 ± 0.20	0.72 ± 0.13
30 min	0.63 ± 0.13	0.54 ± 0.06	0.42 ± 0.04
45 min	0.42 ± 0.03	0.38 ± 0.05	0.28 ± 0.07
60 min	0.33 ± 0.02	0.34 ± 0.03	0.26 ± 0.01

Values given are [%ID/cc], n =3.

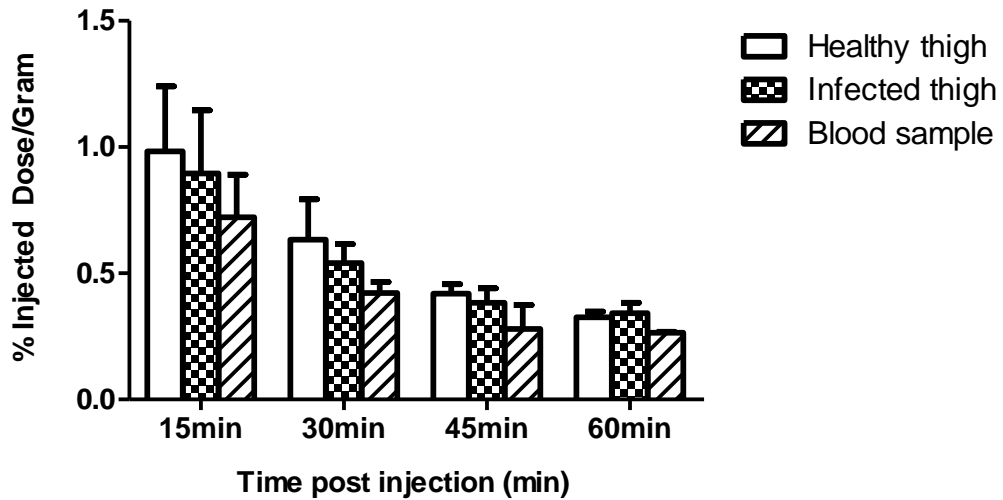


Figure 3. 5 Biodistribution of [¹¹C]PT119 in *S. aureus* thigh infection model.

Biodistribution of [¹¹C]PT119 in systemic infected and healthy mice

Peripheral organ drug distribution was determined in healthy mice and those with systemic *S. aureus* infection (**Figure 3.6** and **Table 3.3**). Again, no significant difference in drug concentration was observed between infected tissues and healthy tissues. For all tissues measured, the highest concentration of drug was measured at 20 min after injection and decreased at later times.

Table 3. 3 Biodistribution in systemic infection model

Healthy control:

	Spleen	Lung	Liver	Kidney	Blood
20 min	0.67 ± 0.12	3.19 ± 0.13	11.79 ± 1.09	2.22 ± 0.19	0.64 ± 0.08
40 min	0.37 ± 0.03	1.75 ± 0.13	9.69 ± 1.40	1.41 ± 0.09	0.41 ± 0.07
60 min	0.19 ± 0.01	1.32 ± 0.13	6.91 ± 1.60	0.93 ± 0.06	0.34 ± 0.03

Values given are [%ID/cc], n = 3.

Systemic infected:

	Spleen	Lung	Liver	Kidney	Blood
20 min	0.71 ± 0.05	3.28 ± 0.31	11.18 ± 0.89	2.41 ± 0.08	0.67 ± 0.09
40 min	0.30 ± 0.10	1.78 ± 0.69	5.25 ± 1.69	1.15 ± 0.14	0.38 ± 0.14
60 min	0.31 ± 0.03	2.01 ± 0.08	7.31 ± 1.76	1.13 ± 0.07	0.44 ± 0.01

Values given are [%ID/cc], n = 3.

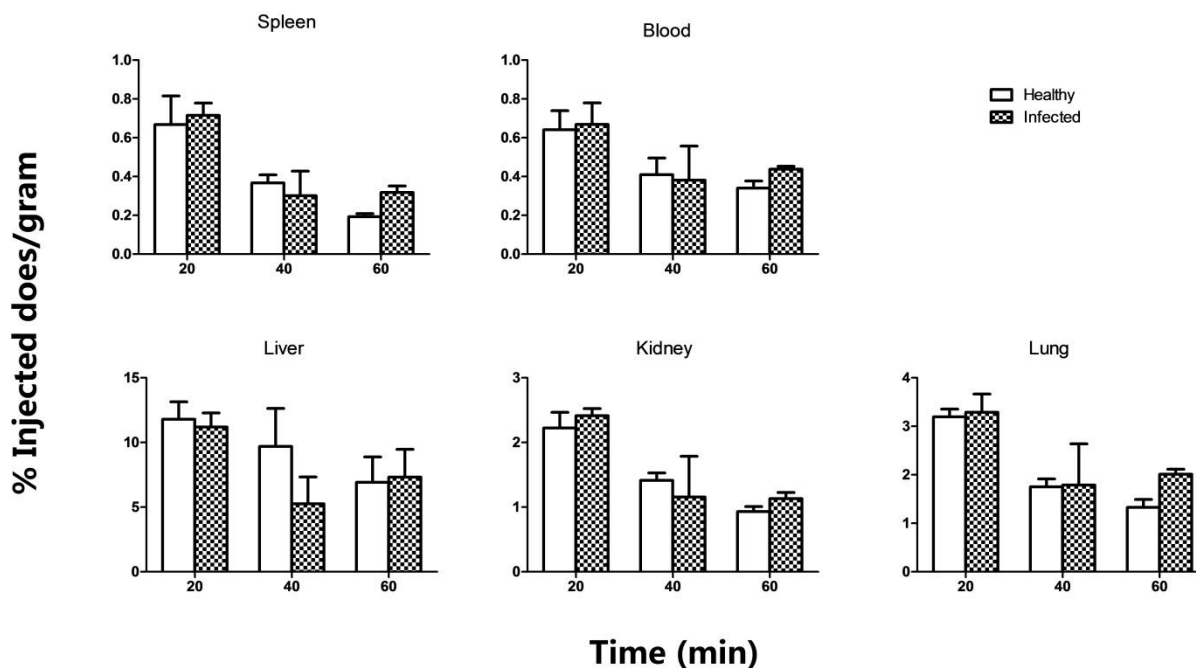
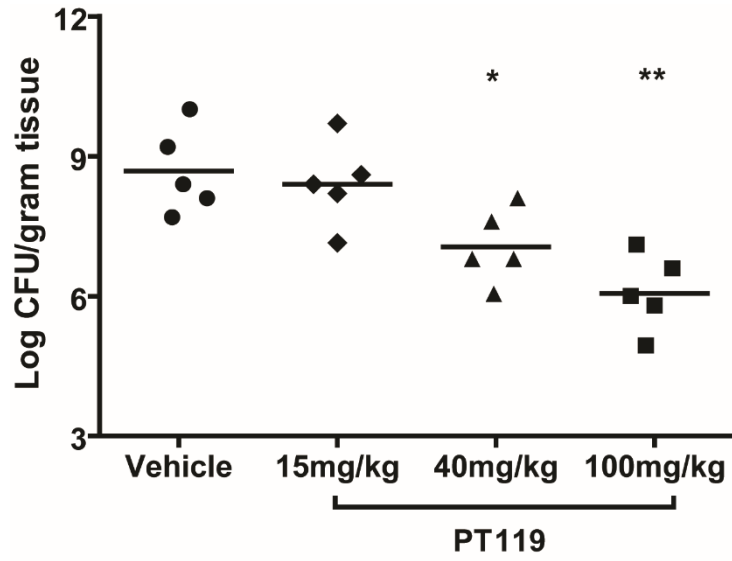


Figure 3. 6 Biodistribution of [¹¹C]PT119 in *S. aureus* systemic infection model.

PT119 has efficacy in the *S. aureus* infected mice

The efficacy of PT119 was evaluated in both the *S. aureus* thigh muscle infection model and the systemic infection model. In the thigh infection model, a single dose of PT119 was delivered sc 1 h post infection. Then the muscle from the infected thigh was collected to enumerate bacterial load 24 hours post infection. Untreated mice generally displayed 10^9 CFU in infected thigh 24 hours post infection. PT119 significantly reduced bacterial growth to 10^7 CFU (40mg/kg; Figure 3.7) and 10^6 CFU (100 mg/kg; Figure 3.7). In the *S. aureus* systemic model, animals in the infection model were treated with PT119 for three consecutive days, starting from the day of infection and then monitored for four additional days. In general, our experiments showed that

all treated animals survived longer than untreated control animals, indicating that PT119 has antibacterial activity and is able to reduce the bacterial load. Untreated control mice had 0% survival rate with a median survival of 1 day, whereas treatment with 100 mg/kg PT119 delivered sc resulted in a 50% median survival.



* P<0.01, ** P<0.001

Figure 3.7a. *In vivo* efficacy in thigh infected model.

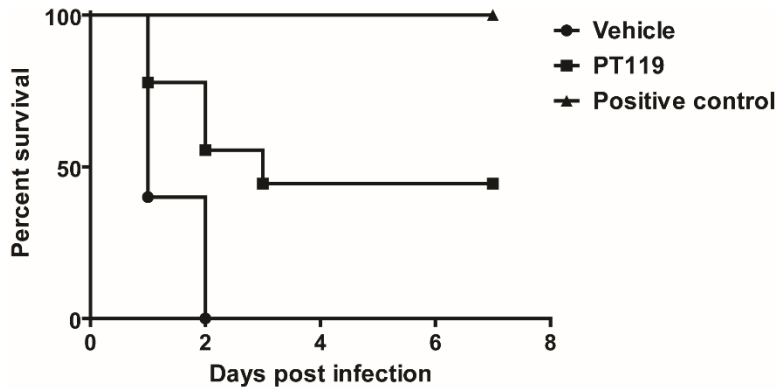


Figure 3.7b. *In vivo* efficacy in systemic infected model.

Figure 3. 7 *In vivo* efficacy of PT119 in two different models.

PK and subcutaneous bioavailability of PT119

The pharmacokinetic parameters that were determined included AUC, C_{\max} , T_{\max} , F (bioavailability) and $t_{1/2}$ for PT119 following dosing at 10 mg/kg iv and 40 mg/kg sc (**Figure 3.6** and **Table 3.4**). The AUC of PT119, which evaluates drug exposure, was 0.64 or 1.77 h* $\mu\text{g/mL}$ when delivered iv at 10 mg/kg or sc 40 mg/kg, respectively. Delivery of PT119 at 10 mg/kg iv resulted in a C_{\max} value of 0.84 $\mu\text{g/mL}$ with a T_{\max} of 0.08 h, whereas a 40 mg/kg dose delivered sc yielded a C_{\max} value of 0.28 $\mu\text{g/mL}$ with a T_{\max} of 4 h. The bioavailability (F) of PT119 was assessed to determine the fraction of the dose reaching the systemic circulation after administration. PT119 delivered sc at 40 mg/kg had an F value of 69% (**Table 3.4**).

Table 3. 4 *In vivo* pharmacokinetic parameters for PT119 delivered iv and sc

Route and dose	iv 10 mg/kg	sc 40 mg/kg
V_{ss} (mL)	475.6	
V_Z (mL)	704.1	
CL(mL/h)	438.8	
MRT* (h)	0.65	6.47
$t_{1/2}$ (h)	1.01	6.17
C_{max} ($\mu\text{g/mL}$)	0.84	0.28
T_{max} (h)	0.08	4
$AUC_{0-\infty}$ ($\text{h} \cdot \mu\text{g/mL}$)	0.64	1.77
AUC ($\text{h} \cdot \mu\text{g/mL}$)/MIC ($\mu\text{g/mL}$)	1.28	3.54
Bioavailability $F(0, \infty)$ (%)		69

*MRT, mean residence time

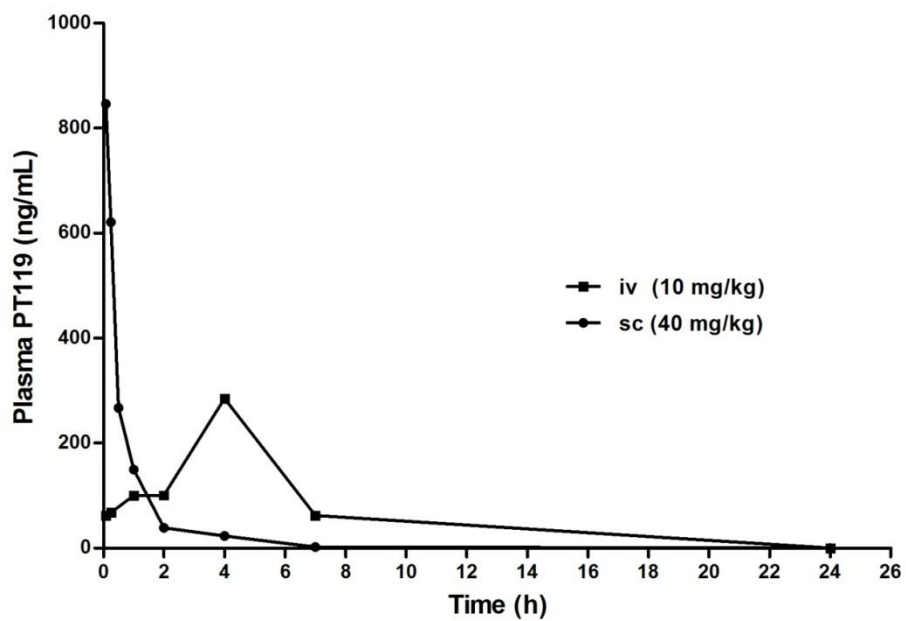


Figure 3. 8 Bioavailability and *in vivo* pharmacokinetics of PT119.

Discussion

The type II fatty acid biosynthesis pathway (FASII) is a promising target for novel antibacterial drug discovery (177, 186) and, using structure-based design, we have developed a series of diphenyl ethers that are potent FASII FabI enzyme inhibitors. Importantly, the activity of the FabI inhibitors against several bacterial pathogens confirms that this enzyme is a sensitive target for the development of broad-spectrum chemotherapeutics (159, 160, 187), and led to the discovery of PT119. Here, we extended our studies on PT119 and developed a radiolabelling method using the PET isotope carbon-11 to determine the biodistribution and pharmacokinetics parameters of this compound. The use of carbon-11 labeling enables the biodistribution of PT119 to be determined without altering the structure of the parent compound. However, the short half-life of carbon-11 (20.4 min) not only makes labelling challenging, but also limits the time window for monitoring drug distribution after administration. In this study, radiosynthesis and formulation of [^{11}C]PT119 has been accomplished in 1 h using [^{11}C]HCN, enabling at least one additional hour for determining the biodistribution of this compound.

The use of PET imaging to study PK has many advantages over other conventional techniques (166, 188). Although in this study drug concentrations in tissues are determined by radioactivity measured in excised tissues (*ex vivo*), the method can be easily be translated to larger species including human subjects, where multiple measurements in the same subject at different times and in a variety of physiologic or pathologic states would be feasible. Another major benefit of PET imaging is that it is a quantitative measurement. Besides the translational potential and quantitative potential, PET can also be used to determine target engagement in human subjects if specific binding of a radiotracer is observed. It is important to determine target engagement

because the pharmacological validation of drug action requires verification that chemical probes engage their intended targets *in vivo* (129).

The parent drug of PT119, triclosan, is an antibacterial agent that has been used worldwide in medical and consumer products for more than 20 years (189, 190). Despite the almost ubiquitous occurrence of the substance, PK studies are sparse (191). In a previous study of orally ingested triclosan in humans, the drug appears to be readily absorbed from the gastrointestinal tract and has a rapid turnover. However the high lipophilicity of the drug gives rise to questions regarding distribution properties and accumulation (192). We previously reported the PK and *in vivo* efficacy against *Francisella tularensis* of PT04, an analog of PT119 (169). Like PT04, which successfully cleared infection in an *F. tularensis* murine model (169), PT119 also decreased bacterial load in *S. aureus* murine model (Fig. 4). However, this study is the first to measure the tissue distribution of triclosan derivatives to our knowledge. The antibacterial efficacy of the saFabI inhibitor AFN-1252 (Affinium Pharmaceuticals, Toronto, ON, Canada) is reported to be driven by AUC/MIC rather than Time>MIC [34]. We would expect the same PD parameter to predict PT119 efficacy because both compounds have similar modes of action, and it is interesting to note that the AUC/MIC value for PT119 at 40 m/kg is only 3.5 despite the fact that this dose of PT119 reduces CFUs by 2 logs in the thigh infection model (AUC/MIC value for AFN-1252 at 30 mg/kg is 20 (193)). Since the PET studies suggest that PT119 has similar blood and tissue concentrations, we speculate that the *in vivo* efficacy of this compound results partly from the long half time of the saFabI:PT119 drug-target complex (t_R 750 min).

A more detailed understanding of the relationship between PK of antimicrobial drugs and their action on target pathogens (PD) has led to greater sophistication in design of dosage schedules which improves the activity and reduce the selection pressure for resistance in antimicrobial therapy. This, in turn, may be informative in the pharmaceutical development of antimicrobial drugs (194). Like most antibacterial agents, PT119 requires transport to the site of infection and interaction with the pathogen. As a result, determining the drug concentration at the site of action is a more accurate approach to determining PD relationships than plasma drug concentration (195). This study presents a promising model to evaluate PK/PD relationships based on target tissue concentrations.

It has been reported that [^{18}F]FDG accumulated in *S. aureus* infected thigh muscles to a level 2.3 – 2.6 times greater than in the healthy thigh (185). However, [^{18}F]FDG is a non-specific marker of glycolytic activity that relies upon a host inflammatory response and cannot discriminate sterile inflammation from infection (196). By targeting intracellular pathogen enzymes rather than the inflammatory response of the host, radiolabelled drugs especially those with significant drug-target lifetime and quick clearance, are promising candidates for probes to detect and localize bacteria. We have previously demonstrated that PT119 has a significant residence time of 750 min on saFabI (182). Since the half-life of ^{11}C is only 20.4 min, using a longer-lived PET isotope, such as ^{18}F (half-life 109.8 min) or ^{124}I (half-life 4.2 days), could potentially be used to achieve the goal though this would be a different drug molecule and the similarity in their properties would need to be determined. In addition, increasing the interval between tracer administration and imaging could further increase signal-to-background ratio by allowing the washout of the background PET signal in future investigation.

Conclusions

In summary, a novel time-dependent saFabI inhibitor, PT119, with optimal drug-target interactions, long residence time and promising MIC, has been labeled with the positron emission isotope carbon-11. [¹¹C]PT119 was synthesized using one-step cyanation, purified and formulated within 1 h, with >98% radiochemical purity. Synthesis of this compound allows for analysis of the biodistribution of the labeled drug in mice using PET. The studies demonstrated that there is rapid accumulation of drug and/or its labeled metabolites in tissues, but that there is no significant difference in distribution between infected animals and healthy animals during the ~ 1h time course of the drug biodistribution following administration. Studies in mice also demonstrated that PT119 was able to decrease bacterial load in both the thigh muscle infection model and systemic infection model. These studies provide an opportunity to review the pharmacokinetics of this new drug in two different *S. aureus* infected mice models which will aid in further optimization of this inhibitor series and will ultimately provide a more accurate approach to determine PK/PDs relationships than plasma drug concentration. These results also indicate that future PET studies in human subjects will yield valuable insights into the clinical application of this drug or other similar drugs, and also set the scene for imaging the distribution of the pathogen *in vivo*.

Acknowledgement

We are grateful to Dr. Michael Schueller for cyclotron operations, and the PET imaging team at BNL (David Alexoff, Youwen Xu, Colleen Shea and Lisa Muench) for technical assistance.

This work was funded by grants to PJT from NIH (GM102864) and from Stony Brook University (TRO Fusion Award).

Chapter 4 Noninvasive Imaging of 5-[¹⁸F]-Pyrazinamide in *Mycobacterium tuberculosis*-infected Mice Using Positron Emission Tomography

Infected animal experiments were conducted in collaboration with Dr. Sanjay Jain and his team in Johns Hopkins University.

Introduction

Tuberculosis (TB) is one of the world's most lethal infectious diseases. In 2011, nearly 9 million people fell ill from TB and 1.4 million died (64). World health Organization (WHO) has estimated that one-third of the world's population is infected with this pathogen, and many of them develop reactivation disease, sometimes decades after the initial infection (197, 198). HIV/AIDS infection, multidrug resistant TB (MDR-TB), and extensively drug resistant TB (XDR-TB) have made the problem more complex (146).

While many bacterial infections are treated using a 1-2 week course of monotherapy, the treatment of TB requires the use of multiple antibiotics over a 6-9 month period, dramatically increasing the risk of noncompliance and enhancing the emergence of resistance (199). Current active TB is treated with first-line drugs, isoniazid (INH), rifampin (RIF), pyrazinamide (PZA), and ethambutol (ETB). This current regime has been used for decades and is primarily based on pharmacokinetics (PK) studies in serum combined with historical data on the efficacy (200, 201). Nevertheless, a growing number of studies support the importance of monitoring drug concentrations in infected tissues

(106, 113, 202). This is because most drugs exert their bactericidal effects at the site of infection than in the plasma and because drug equilibration between plasma and infection site cannot always be achieved (106, 113). Failure to reach optimal drug concentration at the site of infection may result in therapeutic failure and trigger bacterial resistance (113). In severely ill patients, normal physiology may be compromised, thus elevating the risk of renal and hepatic toxicity (203). Therefore, the Food and Drug Administration (FDA) now requires clinical studies of tissue drug distribution at uninfected and infected sites (113). Positron emission tomography (PET), which images drug and other molecules labeled with positron-emitting isotopes, provides a method of acquiring quantitative information on the dynamics of drug absorption, distribution, and elimination in a living animal or human. In addition, this methodology developed for imaging drug distribution in laboratory animals using PET can be readily translated to humans (115). Our group has reported a pioneering study in the field, using positron emission isotope carbon-11 to radiolabel first line TB drugs (INH, PZA, RIF) and to determine multiple tissue organ PK noninvasively in healthy baboon by PET (184). Two years later, we extended our work to determine PK in *M. tuberculosis*-mice using a fluorine-18 analog of INH, in collaboration with Dr. Sanjay Jain in Johns Hopkins University (204).

PZA is another first-line TB drug used in combination with INH, ETB, and RIF for the drug-susceptible TB and frequently for multidrug-resistant TB (64, 205). Novel highly effective TB regimens still require PZA to be effective (206). PZA shortens TB treatment from the 9 to 12 months required before its introduction to the current standard of 6 months, often referred to as a short course chemotherapy (207). Thus, PZA has important

therapeutic effect in current TB-regimen for the treatment of drug-sensitive, drug-resistant, and latent TB.

Despite its importance in clinic setting, the mechanism of PZA is poorly understood (208). The disconnect of poor *in vitro* activity and good *in vivo* sterilizing property remains an unsolved problem (209). Structurally, PZA is an analog of nicotinamide (NAM), requires amide hydrolysis by mycobacterial pyrazinamidase (PZase, a nicotinamidase) to pyrazinoic acid (POA) (210). Mutation in the *pncA* gene encoding the PZase is the major mechanism for PZA resistance in *M. tuberculosis* (211, 212). POA acts against *M. tuberculosis*, but the exact biochemical basis of action has not been fully established. It has been hypothesized that POA either disrupts *M. tuberculosis* membrane transport and energetics, or inhibits fatty acid synthase I (208, 213, 214).

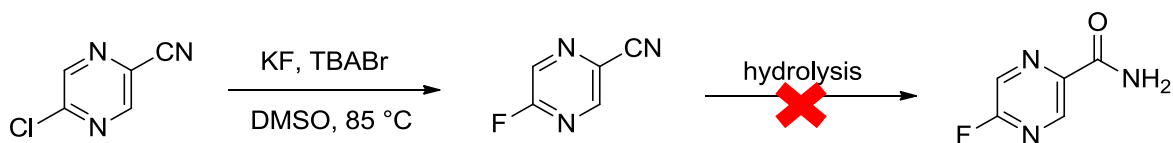
Extensive medicinal chemistry studies have been conducted on pyrazinamide. Among all the structural derivatives of PZA, 5-chloro-pyrazinamide (5-Cl-PZA) is the one most well studied. Unlike PZA, 5-Cl-PZA is active against mycobacterial species including PZA-resistant strains of *M. tuberculosis*, and is only weakly converted by PZase (215). However, it lacks *in vivo* sterilizing activity in *M. tuberculosis* and *M. bovis* infected mice (216).

Here we present the synthesis of a PZA analog, 5-fluoro-pyrazinamide (5-F-PZA), and its corresponding radiolabelling route using fluorine-18. The 5-[¹⁸F]-PZA is used in PET imaging study in *M. tuberculosis* infected mice in order to provide more direct insight into the PK and biodistribution of the drug. Furthermore, we also explore the potential application of using 5-[¹⁸F]-PZA to detect bacteria because of its unique pathogen-specific metabolism.

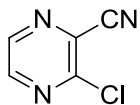
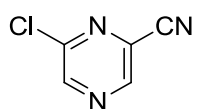
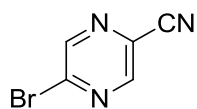
Results

Chemistry

The original proposed synthesis route for 5-F-PZA was presented in **Scheme 4.1**. In this two-step synthesis route, nucleophilic fluorination on the halogen precursor is followed by hydrolysis of cyano group to amide group based on the following rationales: (1) cyano group is a strong electron withdrawing group which can aid the nucleophilic fluorination reaction; (2) the reactivity of amide might interfere with the fluorination reaction, thus starting with a cyano group which can be hydrolyzed into amide subsequently. In reality, we successfully fluorinated the starting material by using potassium fluoride and phase-transfer-catalyst tetrabutylammonium bromide (217). However, the hydrolysis failed due to the fact that fluorine on the para position is activated and not tolerable to various hydrolysis conditions (218, 219).



Other S.M. tried: Other conditions tried:



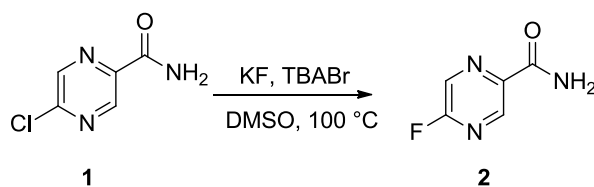
- (1) HF·TEA at various temperature
- (2) HF·pyridine at various temperature
- (3) TBAF, DMF at various temperature
- (4) TBAF, tert-amyl alcohol at various temperature

Hydrolysis conditions tried:

- (1) conc. HCl, THF
- (2) H₂O₂, K₂CO₃
- (3) TFA, H₂SO₄

Scheme 4. 1 Original proposed 2-step synthesis route for 5-F-PZA

Then we explored a one-step synthesis route for non-radioactive 5-F-PZA (**Scheme 4.2**). 5-Cl-PZA, an important PZA analog with increased *in vitro* activity against *M. tuberculosis*, also commercial available as starting material here, is fluorinated with potassium fluoride and phase-transfer-catalyst tetrabutylammonium bromide (217). Other fluorination methods such as hydrogen fluoride and tetrabutylammonium fluoride prove not working for the purpose here. The compound **2** is characterized by GC-EI Mass: Calculated m/z for Molecular Ion C₅H₄FN₃O (M⁺): m/z=141, and 141 was found. ¹H NMR (400 MHz, CDCl₃ and CD₃OD): δ 9.00 (s, 1H), δ 8.36 (d, J=7.8 Hz, 1H). ¹⁹F NMR (400 MHz, CDCl₃ and CD₃OD): δ 75.17 (d, J=7.3 Hz). ¹³C NMR (500 MHz, CDCl₃ and CD₃OD): δ 164.72 (s, 1'-C), δ 161.56 (d, J= 256.5 Hz, 5'-C), δ 142.41 (d, J= 12.8 Hz, 3'-C), δ 142.27 (d, 2'-C) δ 131.78 (d, J=38.7 Hz, 6'-C).

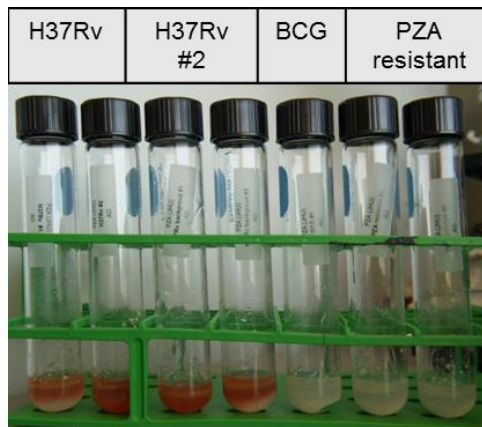


Scheme 4. 2 Synthesis of 5-F-PZA

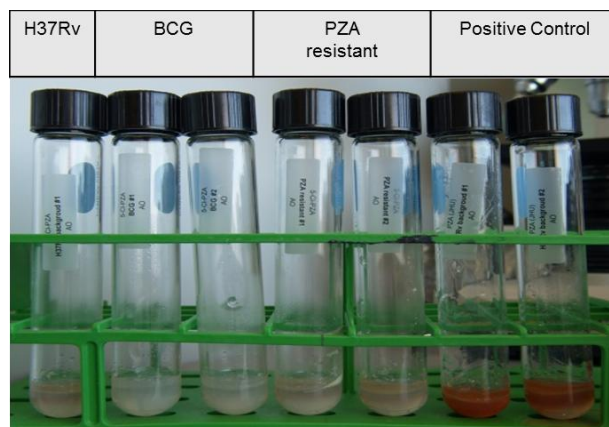
Characterization of 5-F-PZA

As discussed before, PZA is a prodrug which will be converted into pyrazinoic acid (POA) upon deamination by pyrazinamidase (PZase) (210). The susceptibility of PZA to *M. tuberculosis* but not other mycobacteria is based on the presence of an active PZase and a deficiency in POA efflux (210, 220). An assay was developed by Wayne et al to

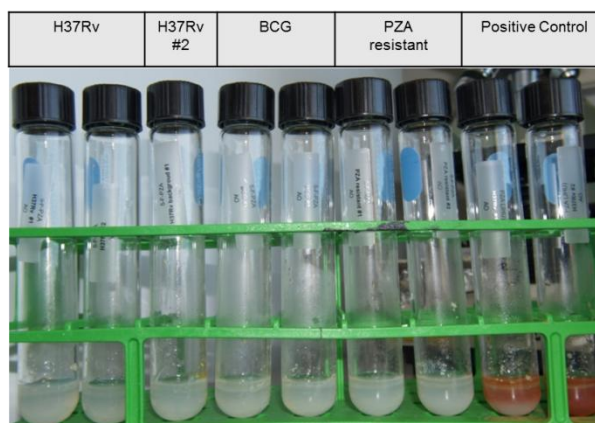
detect PZase activity by monitoring the color change upon the hydrolysis of PZA to POA (221). In this study, a modified Wayne PZase assay was used to evaluate 5-F-PZA and compare the result to PZA and 5-Cl-PZA (222). A PZA-susceptible strain *M. tuberculosis* H37Rv is used as positive control, while PZA resistant strain and BCG strain are used as negative control (**Figure 4.1A**). In the test group of 5-Cl-PZA, it is only weakly converted into corresponding carboxylic acid by not only H37Rv strain but also PZA resistant strain, as shown in **Figure 4.1B**. In the test group of 5-F-PZA, it cannot be converted into the corresponding carboxylic acid by all the mycobacteria strains tested (**Figure 4.1C**).



(A) PZA is converted into POA when tested with the *M. tuberculosis* H37Rv, but not with BCG and PZA-resistant strain.



(B) 5-Cl-PZA is weakly converted into 5-Cl-POA when tested with both *M. tuberculosis* H37Rv and PZA resistant strain, but with BCG.



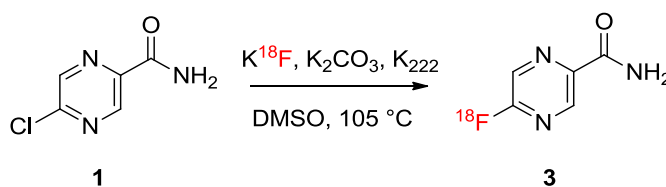
(C) 5-F-PZA is not converted into 5-F-POA when tested with *M. tuberculosis* H37Rv, PZA resistant strain, and BCG.

Figure 4. 1 Wayne's Modified Pyrazinamidase Assay.

PZase activity was measured using a whole-cell Fe(II)-dependent colorimetric assay modified from that of Wayne (221).

Radiochemistry

The radiosynthesis of 5-[¹⁸F]-PZA was accomplished using the one-step classical nucleophilic substitution to a chlorine leaving group (**scheme 4.3**). The average radiochemical yield of the reaction is 30% (non-decay corrected) using 2 mg precursor and a reaction time of 5 min in DMSO at 100 °C. The reaction mixture was subsequently purified by HPLC and fractions from HPLC were concentrated *in vacuo* to generate dry product. The final product was formulated in saline with a trace of sterilized ethanol. The specific activity of 5-[¹⁸F]-PZA is 0.074 Ci/μmol at the time of delivery to animals. The decay-corrected yield is 50%, and the purity is >95%, determined by HPLC. The formation of 5-[¹⁸F]-PZA is confirmed with both analytical and semi-prep HPLC chromatography shown in **Figure 4.2**.



Scheme 4. 3 Radiosynthesis of 5-[¹⁸F]-PZA

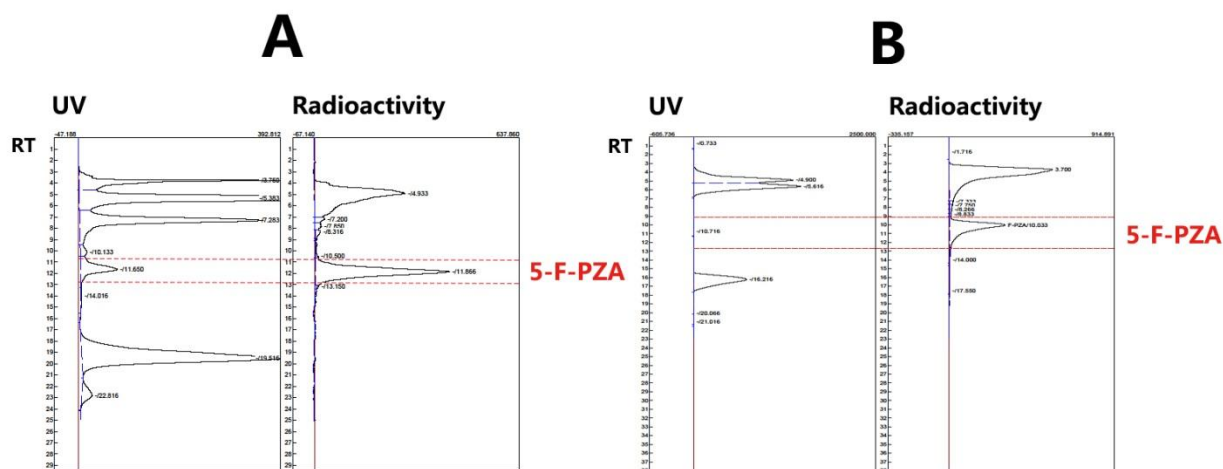


**Figure 4. 2 Analytical and semi-preparation HPLC chromatography of 5-
[¹⁸F]fluoropyrazinamide.**

(A) Analytical HPLC spectrum. The left panel is the time course of UV signal. The right panel is the time course of radioactivity. (B) Semi-preparation HPLC spectrum. The left panel is the time course of UV signal. The right panel is the time course of radioactivity.

PET Imaging

The radiotracer 5-[¹⁸F]-PZA was prepared at Johns Hopkins University with a specific activity of 0.074 Ci/ μ mol at the time of delivery to the animal, and imaged using positron emission tomography (PET) followed by computed tomography (CT) scan in *M.*

tuberculosis infected mice in collaboration with Dr. Jain's lab.

Imaging experiments were performed in C3HeB/FeJ mice for their intrinsic ability to form localized and well-defined TB lesions with central necrosis and hypoxia (223, 224).

Mice were imaged 17-weeks after a low-dose aerosol infection. Pulmonary bacterial

burden was $6.7 \pm 0.3 \log_{10}$ CFU at the time of imaging. Coregistered 5- ^{18}F -PZA-PET/CT images are shown in **Figure 4.3**. Discrete foci of 5- ^{18}F -PZA-PET activity colocalizing with the TB lesions (as seen on CT) were noted in the lung fields of the infected mouse, suggesting that 5- ^{18}F -PZA and/or its radiolabeled metabolite penetrated and concentrated at the site of TB lesions. High uptake in bone in both infected and uninfected animals were observed, suggesting either the presence of free radioactive fluoride or that 5- ^{18}F -PZA and or/its radioactive metabolites accumulate in bone.

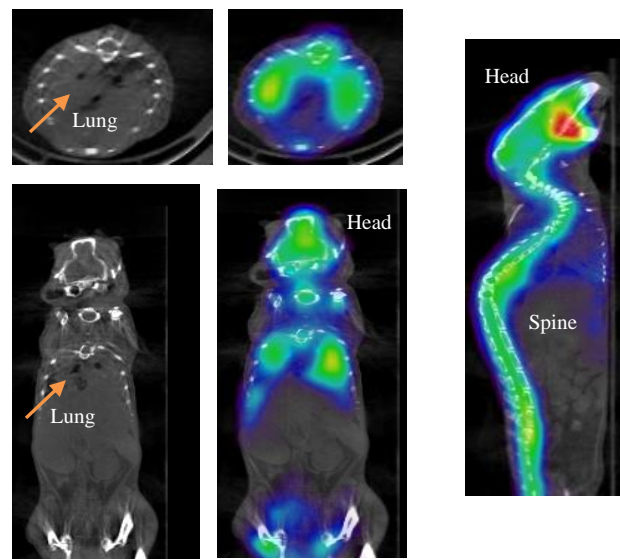


Figure 4. 3 5- ^{18}F -PZA in *M. tuberculosis* infected mouse 30 min post injection.

Images were slices from mice at 30 min, not summed images. The arrow indicates the position of lung.

[¹⁸F]NaF PET/CT imaging was conducted to compare with 5-[¹⁸F]-PZA-PET/CT. Coregistered [¹⁸F]NaF PET/CT images were shown in **Figure 4.4**. Diffuse [¹⁸F]NaF PET activity was noted in the bone area including skull and also lung fields.

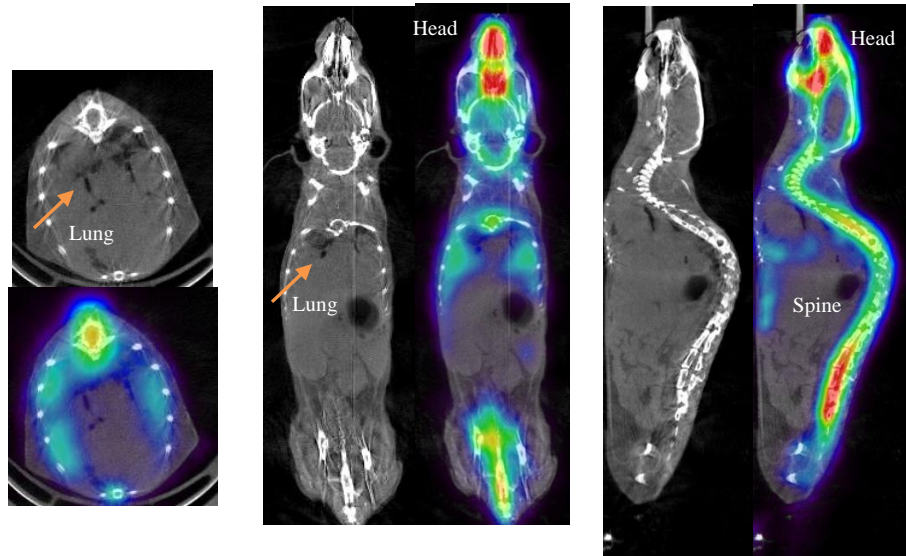


Figure 4. 4 [¹⁸F]NaF in *M. tuberculosis* infected mouse 30 min post-injection. Images were slices from mice at 30 min, not summed images. The arrow indicates the position of lung.

Organ compartment pharmacokinetics of 5-[¹⁸F]-PZA

We performed additional quantitative analyses to evaluate the differences in 5-[¹⁸F]-PZA-PET signal between *M. tuberculosis*-infected and uninfected mice. Following simultaneous 5-[¹⁸F]-PZA injections into paired infected and uninfected C3HeB/FeJ mice, we performed dynamic PET acquisitions overtime. As shown in **Figure 4.5**, there

was more 5- ^{18}F -PZA and/or its radioactive metabolite PET activity in the lung fields of the infected mice than in uninfected mice.

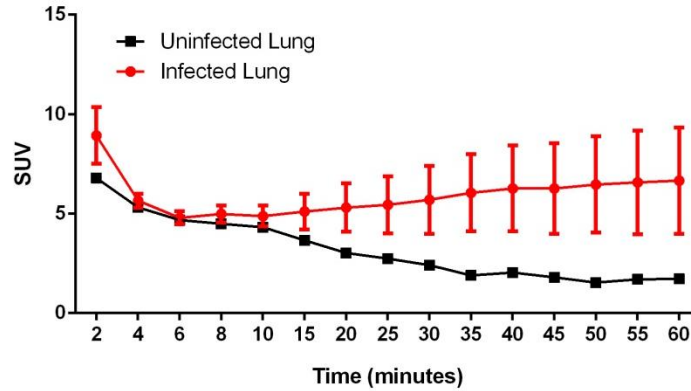


Figure 4.5 Lung compartment pharmacokinetics of 5- ^{18}F -PZA.

Infected group has 3 animals, uninfected group has 1 animal. SUV stands for standardized uptake value.

***Ex vivo* biodistribution**

Mice were sacrificed after PET/CT scans for tissue biodistribution determination. As shown in **Figure 4.6**, the radioactivity in lung and brain of infected mice is much higher than uninfected mouse. Because the mice were sacrificed 80 min (60 min PET + 20 min CT) after injection, one the possible explanation for the higher signal-to-background ratio is that the background signal has been washed away.

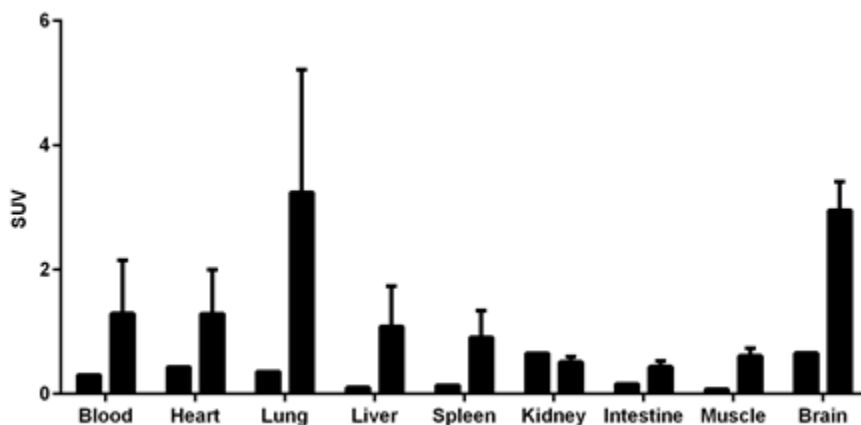


Figure 4. 6 Ex vivo tissue biodistribution of 5-[¹⁸F]-PZA in *M. tuberculosis* infected and uninfected mice.

Infected group has 3 animals, uninfected group has 1 animal. SUV stands for standardized uptake value.

Microsomal Stability Assay

Mice microsomal stability assay was performed to evaluate the metabolic stability of 5-F-PZA. As shown in table 1, 87.3% of 5-F-PZA remains intact after incubating with mice microsomes for 40 min (**Table 4.1, Figure 4.7**).

Table 4. 1 Metabolic stability of 5-F-PZA in mouse liver microsomes.

Incubation Time (min)	Area ratio Sample 01	Area ratio Sample 02	Average	%Remaining
0.0	0.9080	0.8700	0.889	100
5.0	0.8470	0.8660	0.857	96.3
10.0	0.8400	0.8480	0.844	94.9
20.0	0.8340	0.8590	0.847	95.2
40.0	0.7990	0.7530	0.776	87.3

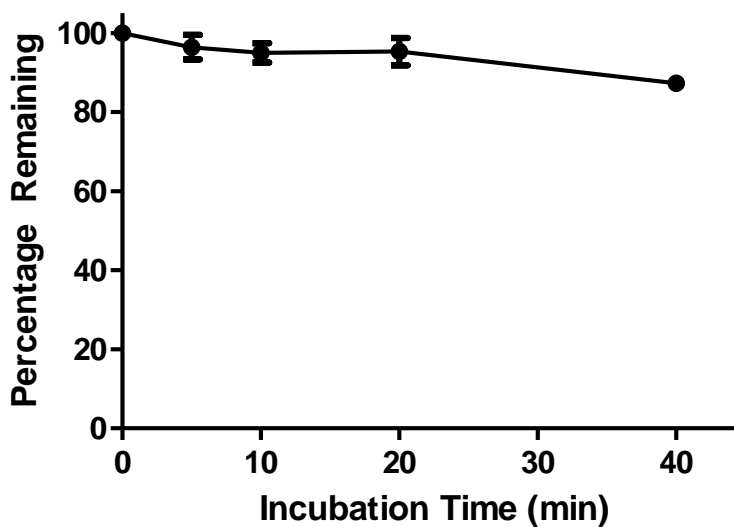


Figure 4. 7 Metabolic stability of 5-F-PZA in mouse liver microsomes.

Discussions

PZA has been playing an important role in TB therapy since its introduction. The fact that PZA was considerably more active *in vitro* at acidic pH gave rise to the idea that the drug targets a subpopulation of TB bacteria that are dormant and residing in an acidified niche (225). Despite the ongoing argument on molecular target of PZA or POA (226-228), PZA continues to show its importance in combinational therapy. For example, PZA works synergistically with newly approved TB drug TMC207 (229). Dartois et al recently reported that vascular supply of host-derived (in addition to PZase converted) POA may contribute to the *in vivo* efficacy of PZA, therefore reducing the apparent discrepancy between *in vitro* and *in vivo* activity (230). Like most antimicrobial agents, PZA requires transport to the site of infection to be able to interact with the pathogen. Therefore, drug concentration at infection site is a more useful parameter to correlate with PD than serum drug concentration (195). Matrix-assisted laser desorption ionization (MALDI) mass spectrometry has the power to detect drugs within TB granulomas (121), but has to be performed in *ex-vivo* tissue samples. Clinical dialysis is another tool for continuous monitoring of drug concentration (231), but the technique requires precise anatomic knowledge of the lesion location for probe insertion. Here we present the utilization of PET imaging to generate *in situ* PK non-invasively in live animal and potentially to detect bacterial infection. The method can also be easily translated to healthy volunteers and patients.

Our data shows that 5-Cl-PZA is only weakly converted to its corresponding carboxylic acid (5-Cl-POA), but it is also subject to weak deamination by PZA-resistant strain and BCG strain. Taken together the fact that 5-Cl-PZA has much wider range of *in vitro* activity compared to PZA, it is likely that halogen substituted PZA present a different mechanism of action than its parent compound (232). In the case of 5-F-PZA, none of the tested mycobacteria species is able to convert it into its corresponding carboxylic acid (5-F-POA).

The 5-[¹⁸F]-PZA PET activity in infected mice correlates with TB lesions and is higher than in uninfected mouse. However, the 5-[¹⁸F]-PZA PET images resemble [¹⁸F]NaF-PET images, rising the argument that the signal might be from free [¹⁸F] fluoride which is known to be a skeletal imaging reagent since 1962 (233). The metabolic stability of 5-F-PZA has been evaluated and reveals that the compound is stable when incubated with mouse liver microsomes. It is common in PET imaging using isotope fluorine 18 that even a small percentage of defluorination can cause significant bone uptake due to its high sensitivity (234). Taking a close comparison between brain region of 5-[¹⁸F]-PZA and [¹⁸F]NaF PET, one can observe that PET activity accumulates in the brain in 5-[¹⁸F]-PZA while in the skull in the case of [¹⁸F]NaF PET, which is consistent with the previous report that PZA's ability to penetrate brain-blood-barrier (184) and the distribution pattern of [¹⁸F]fluoride. Alternatively, different labeling positions could be employed to increase the metabolic stability and thusly minimize or eliminate defluorination *in vivo*. Taken together, these data suggest that 5-[¹⁸F]-PZA accumulated in infected tissue due to pathogen-specific metabolism, therefore can be used as a promising probe candidate to

detect pathogen distribution *in vivo*. In addition, as a PK probe of PZA, the distribution data also offers explanation for the discrepancy between *in vitro* and *in vivo* activity, that the drug is accumulated in infected tissue.

Another interesting discovery from our data is that the signal-to-background ratio is increasing over time, suggesting tracer specific retention and clearance of background signal. Since the half-life of fluorine-18 is 109.8 min, using a longer-lived PET isotope, such as iodine-124 (half-life 4.2 days), could potentially be used to achieve the goal. In addition, increasing the interval between tracer administration and imaging could further increase signal-to-background ratio by allowing the washout of the background PET signal in future investigation.

Conclusions

In summary, we have developed a radiosynthesis route for 5-[¹⁸F]-PZA, a fluorinated analog of front-line TB drug PZA, as an imaging probe for determining PK in *M. tuberculosis* infected-mice using PET. The biodistribution and multicompartiment pharmacokinetics of the labeled drug has been evaluated. Furthermore, metabolic stability of the tracer is determined using mouse liver microsomes to improve our understanding of the tracer's fate *in vivo*. The data suggests 5-[¹⁸F]-PZA as a promising imaging probe with room to improve regarding *in vivo* stability and employing longer-lived isotope. This methodology is rapid, non-invasive, and most importantly, can be readily translated to clinical settings.

Experimental Section

Synthesis of Reference 5-Fluoropyrazinamide (2)

5-Chloropyrazinamide (**1**, 50 mg, 0.3173 mmol), potassium fluoride (110.43 mg, 1.90 mmol) and tetrabutylammonium bromide (20.46 mg, 0.064 mmol) were added to a 10ml RBF and put under vacuum for 1 hour to dry. After filling the RBF with N₂, 10ml dry DMSO stored over molecular sieves were added into the RBF. The reaction mixture was heated to 110 °C and reflux for 30 min under the protection of N₂. TLC was used to confirm the completion of the reaction. After the reaction mixture cooled down to room temperature, it was extracted with iced water and ethyl acetate. The organic layer was dried with MgSO₄. Then the dried organic layer was distilled under vacuum to give crude products. Silica gel column was used to purify the crude compound **2**.

GC-EI Mass: Calculated m/z for Molecular Ion(M⁺): m/z=141, and 141 was found. ¹H NMR (400 MHz, CDCl₃ and CD₃OD): δ 9.00 (s, 1H), δ 8.36 (d, J=7.8 Hz, 1H). ¹⁹F NMR (400 MHz, CDCl₃ and CD₃OD): δ 75.17 (d, J=7.3 Hz). ¹³C NMR (500 MHz, CDCl₃ and CD₃OD): δ 164.72 (s, 1'-C), δ 161.56 (d, J= 256.5 Hz, 5'-C), δ 142.41 (d, J= 12.8 Hz, 3'-C), δ 142.27 (d, 2'-C) δ 131.78 (d, J=38.7 Hz, 6'-C).

PZase assay

The modified Wayne's PZase assay was conducted as described before (221), with slightly modifications (222). Briefly, 7H9 broth base was dissolved in water, to which 2 mL glycerol, PZA (or other tested compound) at a final concentration of 400 µg/mL, and

1.5% agarose were added. Four – mL aliquots of this melted agar were distributed in glass tubes and autoclaved. After the agar plate is prepared, actively growing culture was carefully inoculated and incubated at 37 °C for 4 days. 1 mL ferrous ammonium sulfate (1%) was added to each tube after incubation and observed for an initial 4 h for the appearance of a pink band (positive). The PZA-susceptible strain *M. tuberculosis* H37Rv was used as positive control, and the PZA-resistant strain was used as negative control.

Radiosynthesis of 5-[¹⁸F]F-pyrazinamide (3)

The development of radiosynthesis was conducted at Dr. Fowler's lab in Brookhaven National Laboratory. The radiosynthesis for imaging studies were performed at Dr. Pomper's lab (Johns Hopkins Medical Center) with assistance of Dr. Ronnie Mease. Aqueous [¹⁸F]KF was eluted from the resin with 1 ml K₂CO₃ (1mg) in MeCN/H₂O solution (900 µL/100 µL) into a Reacti-Vial preloaded with 5 mg Kryptofix 2.2.2.. The solution was azeotropically dried with additional aliquots of MeCN at 105 °C. 2mg of **1** was dissolved in 300 µL DMSO and the whole solution was added to the Reacti-Vial. The sealed Reacti-Vial was heated at 105°C for 5 min before it was quenched by addition of 3 ml cold H₂O. The mixture was loaded onto a semipreparative HPLC column (Phenomenex, Luna PFP 250 × 10, 5 µm) operated at a 5 ml/min flow rate with a mobile phase consisting of 8% MeCN/92% H₂O. The product was collected at the expected retention time (10 min) and the solvent was removed by rotary evaporation. After dilution with 1-2 ml of saline, the solution was filtered through an Acrodisc 13 mm syringe filter equipped with a 0.2 µm Supor membrane (Pall Corporation, Ann Arbor, MI) into a sterile

vial. Radiochemical purity was determined by reverse-phase analytical HPLC using a Phenomenex, PFP, 250×4.6 , $5 \mu\text{m}$ column operated at 1 ml/min flow rate using a mobile phase of 8% MeCN/92% H_2O .

Microsomal Stability Assay

Test compound was weighed and dissolved in 100% DMSO to obtain 10 mM stock solution. The stock solution was diluted to 500 μM with mixture of methanol and H_2O (1:1). The final concentrations of DMSO and methanol were equal or less than 0.1%. Liver microsomes incubations were conducted in duplicate in 96 - well plates. Each well contained 40 μl of 0.1M potassium phosphate buffer (pH 7.4), 2.5 mM MgCl_2 , 0.625 mg/ml mouse liver microsomes, and test compound (1.25 μM) or positive control. After 5-min preincubation at 37 °C, 10 μl of 5.0 mM NADPH in 0.1M potassium phosphate buffer was added to initiate the enzymatic reaction. The final component concentrations are 0.1M potassium phosphate buffer (pH 7.4), 1.0 mM NADPH, 2.0 mM MgCl_2 , 0.5 mg/ml mouse liver microsomes, and test compound (1.0 μM) or positive control (1.0 μM). Reactions were terminated at various time points (0, 5, 10, 20, 40 min) by adding 100 μl of ice-cold acetonitrile containing internal standard. A parallel incubation was performed using 0.1M potassium phosphate buffer (pH 7.4) instead of NADPH as the negative control, and reactions was terminated at 40 min after incubation at 37°C.

Animal Experiment

Protocols were approved by the Johns Hopkins Biosafety, Radiation Safety and Animal Care and Use Committees.

***In vivo* aerosol infection**

Five- to six-week-old female C3HeB/FeJ (Jackson Laboratory) mice were aerosol infected with frozen stocks of *M. tuberculosis* H37Rv, using the Middlebrook Inhalation Exposure System (Glas-Col). Three mice were sacrificed at 1 day and 17 weeks after infection to determine the number of bacilli implanted in the lungs and the bacillary burden at the time of imaging. The entire lungs were homogenized in PBS and plated onto Middlebrook 7H11 selective plates (Becton Dickinson). All plates were incubated at 37 °C for 4 weeks before the colonies were counted. A separate group of identically infected mice were used for imaging studies.

Bio-containment and anesthesia

Live *M. tuberculosis*-infected animals were imaged within a sealed bio-containment bed (Minerve) modified in-house to be compliant with biosafety-3 containment. Two 0.22 µm 60 mm disc VACU-GUARD (Whatman) filters were used in series at both the inlet and the outlet to contain the bacteria within the device. A standard small animal anesthesia machine was used to deliver a mixture of Isoflurane (Henry Schein) and oxygen during transport and imaging. Animals were anesthetized, a 30 gauge needle (BD Bioscience)

was attached to polyethylene-10 tubing (Braintree Scientific) was inserted into the lateral tail vein of each mouse as a catheter for tracer delivery. Animals were sealed inside the bio-containment device in the biosafety level 3 facility and the external surfaces of the bio-containment device was decontaminated and transported to the imaging suite. During prolonged anesthesia (> 20 min), an infrared thermometer and a heat-lamp were used to measure and maintain ambient air temperature inside the bio-containment device.

[¹⁸F]NaF-PET/CT imaging

The night before each imaging time-point, mice were fastened for 12 hrs. Water was provided *ad libitum*. On the day of imaging, each mouse was weighed, injected with 200 μ Ci of [¹⁸F]NaF via the tail vein and imaged 45 min post-injection using the Mosaic HP (Philips) Small Animal PET imager with 15 min static acquisition. A CT scan was also performed at the same time using the NanoSPECT/CT (BIOSCAN) *in vivo* animal imager. PET images were reconstructed and co-registered with CT images. Three mice were used for each group.

5-[¹⁸F]-PZA-PET/CT imaging

One week after PET scan with [¹⁸F]NaF, the same C3HeB/FeJ mice were weighed, injected with 200 μ Ci of 5-[¹⁸F]-PZA via the tail vein and imaged 20 min postinjection using the Mosaic HP (Philips) Small Animal PET images with 10 min dynamic acquisition windows for 120 min. Infected and uninfected controls were scanned two at a time as matched pairs. A different group of animals from the same cohort was

injected with 200 μCi of 5- ^{18}F -PZA via the tail vein catheter at the start of image acquisition, and dynamic windows were set for 5 2-minute windows, followed by 10 5-minute windows for a total scan time of 60 minutes. CT scans were immediately performed subsequent to PET imaging using the NanoSPECT/CT (BIOSCAN) *in vivo* animal imager. PET data were reconstructed and co-registered with CT images. Images were automatically coregistered and presented VivoQuant 1.22, with a resulting 1:1 correspondence. Each animal CT had two spherical (3 mm diameter) regions of interest (ROI) drawn manually in the lung fields making sure not to overlap the PET-active liver while but single ROIs were outlined for liver and brain. The standard uptake values (SUV) were computed by normalizing the ROI activity for each mouse to the injected dose and animal weight using Amide version 1.0.4. For each group, the mean lung 5- ^{18}F -PZA-PET activity at each time-point was calculated by averaging the normalized lung SUV of all the ROIs in that group. Mean lung 5- ^{18}F -PZA-PET activity at each time-point was also calculated similarly for uninfected animals used as controls and imaged at the same time. At least 3 animals were imaged for each group.

Statistical analysis

Statistical comparison between groups was performed using one tail distribution, two sample, unequal variance t-test in Excel 2010 (Microsoft). Data are presented on a linear scale as mean \pm standard error for the mean PET activities and on a logarithmic scale as mean \pm standard deviation for CFU counts.

Chapter 5 Synthesis, Characterization, and Radiolabelling of 2-(¹⁸F)fluoro-4-aminobenzoic acid ([¹⁸F]-PABA) for PET imaging

Introduction

Early and accurate diagnosis is of utmost importance in the attempts to combat bacterial infections. Currently available diagnostic methods often depend on the availability of clinical samples that contain bacteria, which is sometimes difficult to obtain. These methods can also be time consuming, in some cases are inaccurate (14, 18).

Consequently, there is an urgent need to develop a method that can rapidly and specifically detect and localize bacteria in infected patients.

Noninvasive anatomic imaging techniques, such as Computed Tomography (CT) and Magnetic Resonance Imaging (MRI), as well as functional imaging modalities, such as Position Emission Tomography (PET) and Single Photon Emission Computed Tomography (SPECT), are used when an occult infection is suspected in clinical settings (235). Among these techniques, 2-deoxy-2-[¹⁸F]fluoro-D-glucose ([¹⁸F]FDG)-PET has emerged as a highly sensitive and widely used tool (33). PET is an excellent tool for non-invasive imaging in which molecules of interest are radiolabelled with positron emitting isotopes such as carbon-11 and fluorine-18 (3). [¹⁸F]FDG is an analogue of glucose, and accumulates in tissues that have high glycolytic activity such as tumor cells (24, 25). The utility of [¹⁸F]FDG-PET to image bacterial infection (53, 236-238) and to monitor the response to therapy (239, 240) also has been evaluated. However, [¹⁸F]FDG relies on

host inflammatory responses and can not differentiate among oncologic, inflammatory, and infectious processes. The fact that [^{18}F]FDG accumulates in many other human cells limits the utility of [^{18}F]FDG in the clinical diagnosis of bacterial infection (53, 238).

In the efforts to identify and develop novel radiotracers that can specifically detect bacterial infection in human patients, we hypothesize that small molecules which are essential for bacterial metabolism but not for human cells will be actively and selectively taken up by bacterial cells where they will accumulate. Therefore, the radiolabelling of these small molecules with positron emitting isotopes should allow the detection and localization of pathogens *in vivo* with PET. Para-aminobenzoic acid (PABA) is our molecule of interest (**Figure 5.1**). PABA is the natural substrate for the enzyme dihydropteroate synthase (DHPS) which catalyzes the incorporation of PABA into tetrahydrofolate (**Figure 5.2**) (241), which functions as a one-carbon carrier in a variety of biosynthetic reactions (242). Bacteria need PABA for the purpose of tetrahydrofolate synthesis while human cells do not. Although bacteria can synthesize PABA *de novo* from the pentose phosphate pathway (241), studies also show that bacteria can take up and use PABA from exogenous sources (243). Our collaborator at Johns Hopkins University (Dr. Sanjay Jain) has demonstrated that bacterial cells accumulate PABA to much higher levels than mammalian cells (unpublished data).

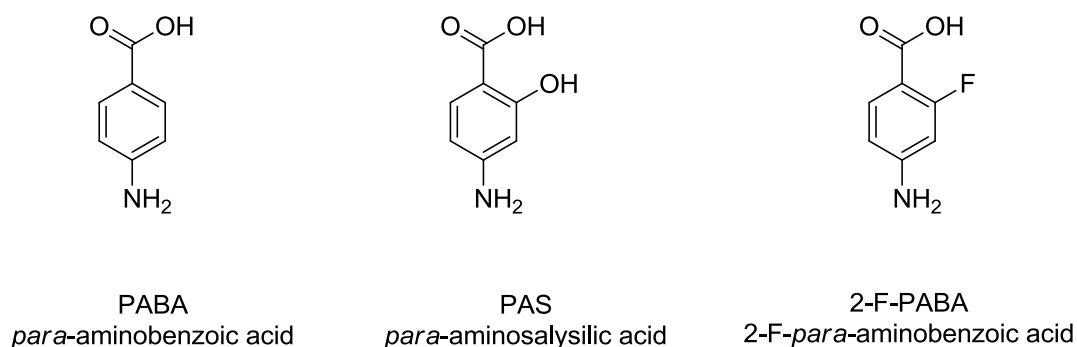


Figure 5. 1 Structures of PABA, PAS, and 2-F-PABA

Relevant to our hypothesis, important discoveries have recently been made to understand the mode of action for *p*-aminosalicylic acid (PAS), a structural analog of PABA and a second line drug for tuberculosis (244). It has been shown that instead of inhibiting DHPS as previously speculated, PAS is actually an alternative substrate for the DHPS enzyme and is incorporated into dihydropteroate in tetrahydrofolate synthesis pathway (245), which subsequently, inhibits dihydrofolate reductase (DHFR) (**Figure 5.2**) (246) in *Mycobacterium tuberculosis*. Similar to PAS, which carries a hydroxyl group at 2 position, 2-F-PABA will also very likely to be the natural substrate PABA and thus accumulate in infected tissues specifically due to bacterial uptake.

In this study, we will develop the synthesis route for PABA analog, 2-F-PABA, and test whether or not it can be sequestered in bacteria through a mechanism similar to PABA and PAS (247). Then, we will develop radiolabelling strategy for 2-[¹⁸F]-PABA, and explore its ability to detect and localize bacterial infection.

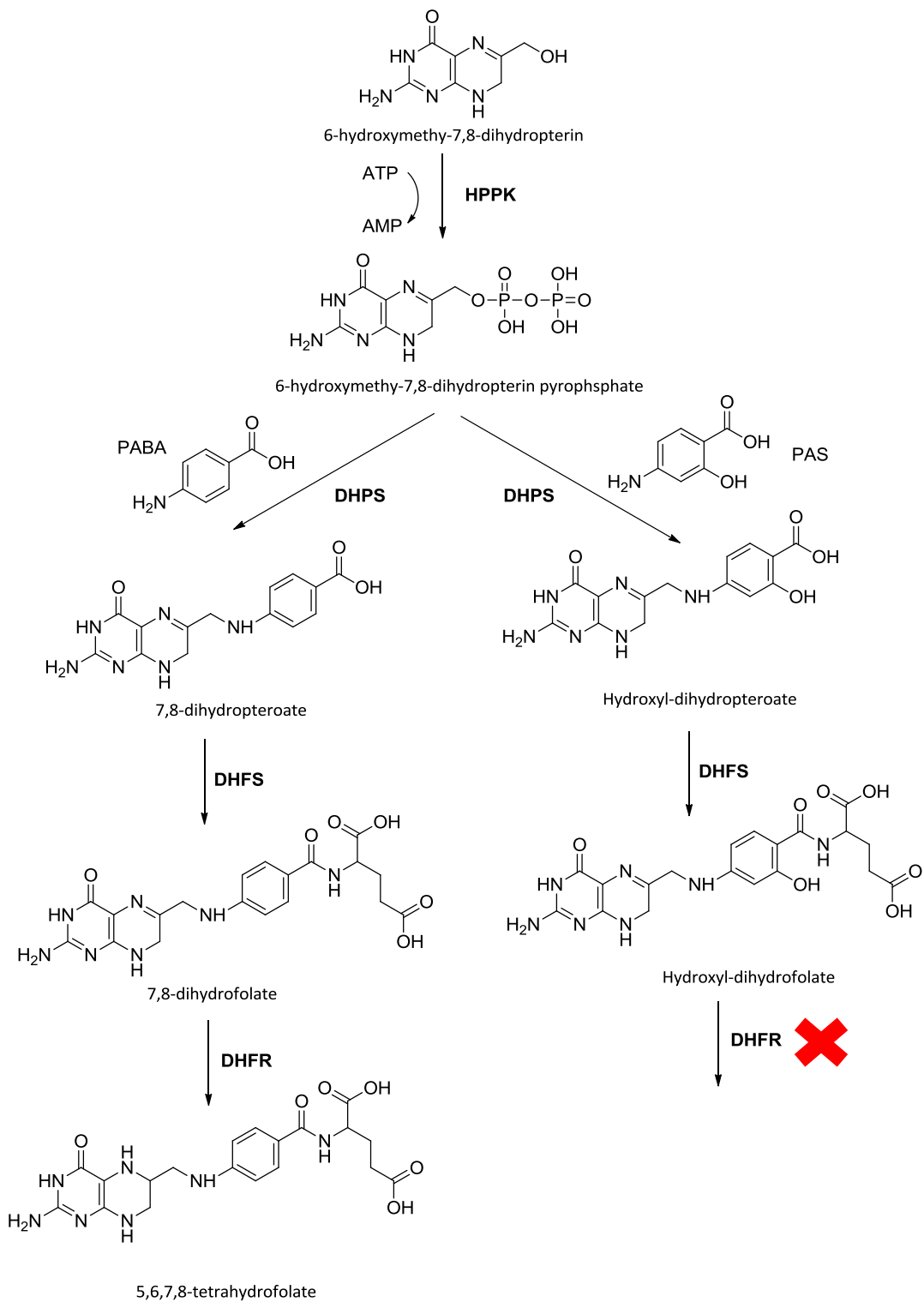


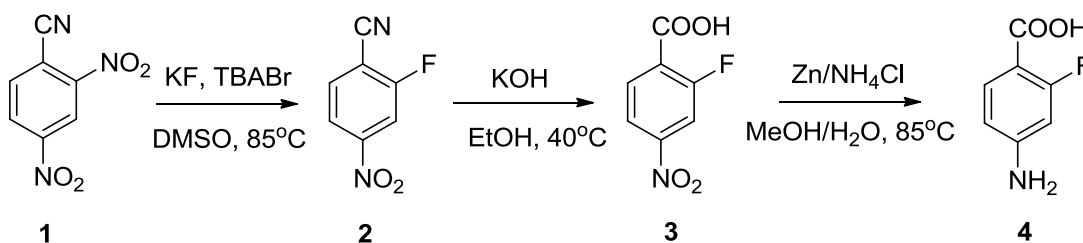
Figure 5. 2 PAS is an alternative substrate for DHPS and the product analog inhibits DHFR. Reproduced from (246).

Methods and Materials

Chemistry

The starting materials (compound **1**, **5**, and **7**) were purchased from Sigma-Aldrich and used without further purification. The nonradioactive chemistry method is developed by Zhuo (Dean) Zhang from Dr. Tonge's research group.

Synthesis of 2-F-PABA from 2, 4-Dinitrobenzonitrile



Scheme 5. 1 Synthesis of 2-F-PABA from 2, 4-dinitrobenzonitrile

2-Fluoro-4-nitrobenzonitrile (2)

2, 4-dinitrobenzonitrile (**1**, 500 mg, 2.59 mmol), potassium fluoride (450.75 mg, 7.77 mmol) and tetrabutylammonium bromide (167.02 mg, 0.52 mmol) were added to a 100 ml RBF and put under vacuum for 1 hour to dry. After filling the RBF with N₂, 50 ml dry DMSO stored over molecular sieves were added into the RBF. The reaction mixture was heated to 110 °C and refluxed for 30 min under N₂. TLC was used to confirm the completion of the reaction. After cooling to room temperature, it was extracted with iced water and ethyl acetate. The organic layer was dried with MgSO₄, and the concentrate in vacuo give the crude product. Purification by *Combiflash* using a silica gel column

yielded compound **2**. **ESI-MS** Calculated m/z for C₇H₃FN₂O₂ Molecular Ion ([M]⁺): m/z=166.02, found m/z=166.05, found m/z=120.03 for [M-NO₂]⁺. **¹H NMR** (400 MHz, CDCl₃) δ 8.19 (ddd, J=8.5, 2.1, 0.9 Hz, 1H), δ 8.13 (dd, J=8.4, 2.1 Hz, 1H), δ 7.91 (dd, J=8.5, 6.2 Hz, 1H). **¹⁹F NMR** (400 MHz, CDCl₃): δ -101.0492 – - 101.09 (m).

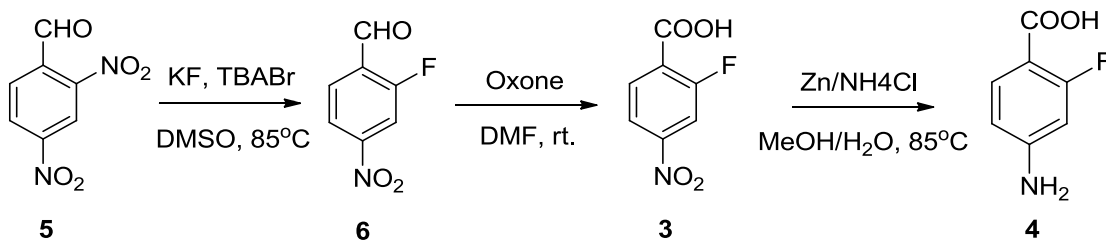
2-Fluoro-4-nitrobenzoicacid (3)

2-Fluoro-4-nitrobenzotrile (**2**, 200 mg, 1.20 mmol), was added to a solution of KOH (1.12 g, 20 mmol) in H₂O/EtOH (10 ml/2 ml). The reaction mixture was stirred for 4 h at 40 °C. After completion of the reaction was confirmed by TLC, the reaction mixture was concentrated under reduced pressure. Then the reaction mixture was acidified to pH ~1 using 10 M HCl and extracted with ethyl acetate. The organic layer was dried with MgSO₄, and then evaporated under vacuum to give crude product. Purification by *Combiflash* using a silica gel column (MeOH/CH₃Cl=5%, with 0.1% Acetic Acid) yielded compound **3**. **ESI-MS** Calculated m/z for C₇H₄FNO₄ Molecular Ion [M-H]⁻ in negative mode is m/z=184.01, found m/z=184.01 for [M-H]⁻. **¹H NMR** (400 MHz, CDCl₃ and CD₃OD): δ 8.16 – 8.12 (m, 1H), δ 8.06 (dd, J=8.6, 1.7 Hz, 1H), δ 8.00 (dd, J=9.9, 1.9 Hz, 1H). **¹⁹F NMR** (400 MHz, CDCl₃ and CD₃OD): δ 104.90 – 104.95 (m). (Commercially available standard *2-Fluoro-4-nitrobenzoicacid (3)* **¹H NMR** (400 MHz, CDCl₃ and CD₃OD) δ 8.14 (dd, J=8.6, 7.0Hz, 1H), δ 8.06 (ddd, J=8.6, 2.1, 0.8 Hz, 1H), δ 8.00 (dd, J=9.9, 2.1 Hz, 1H) **¹⁹F NMR** (400 MHz, CDCl₃ and CD₃OD): δ 104.78 – 104.82 (m)).

2-Fluoro-para-aminobenzoic acid (**4**)

2-Fluoro-4-nitrobenzoic acid (**3**, 100 mg, 0.54 mmol), zinc powder (353.20 mg, 5.40 mmol) and ammonium chloride (433.53 mg, 8.10 mmol) were added to a 25 mL RBF containing MeOH/H₂O (4.5/1 ml). The reaction mixture was heated to 80°C and refluxed for 20 min. Upon the completion of the reaction which was confirmed by HPLC, then reaction mixture was cooled to RT and concentrated under reduced pressure. The pH was then adjusted to 4, and the solution was extracted with ethyl acetate. The organic layer was dried with MgSO₄, and then evaporated under vacuum to give crude product. Purification by *CombiFlash* using a silica gel column (MeOH/CH₃Cl=5%) yielded compound **4**. **ESI-MS** Calculated m/z for C₇H₆FNO₂ [M-H]⁻ in Negative mode is m/z=154, found m/z=154 in Negative mode ESI-MS. Calculated m/z for [M+H]⁺ in positive mode ESI-MS is m/z=156, found m/z=156 in positive mode ESI-MS. **¹H NMR** (400 MHz, CD₃OD) δ 7.66 (dd, J= 8.6, 8.6 Hz, 1H), δ 6.42 (dd, J= 2.2, 8.6 Hz), δ 6.32 (dd, J=2.2, 13.8 Hz). **¹⁹F NMR** (400 MHz, CD₃OD): δ -110.5213 – -110.5825 (m). **¹³C NMR** (400 MHz, CD₃OD) δ 168.32 (d, J= 3.7 Hz, 7'-C), δ 166.05 (d, J= 254.7 Hz, 2'-C), δ 156.95 (d, J= 12.5 Hz, 4'-C), δ 134.98 (d, J= 3.1 Hz, 6'-C), δ 110.63 (d, J= 1.6 Hz, 5'-C), δ 06.51 (d, J= 9.5 Hz, 1'-C), δ 101.51 (d, J=25.6 Hz, 3'-C).

Synthesis of 2-F-PABA from 2, 4- Dinitrobenzaldehyde



Scheme 5. 2 Synthesis of 2-F-PABA from 2, 4-dinitrobenzaldehyde

2-Fluoro-4-nitrobenzaldehyde (6)

2, 4-dinitrobenzaldehyde (**5**, 100 mg, 0.51 mmol), potassium fluoride (88.72 mg, 1.53 mmol) and tetrabutylammonium bromide (32.87 mg, 0.10 mmol) were added to a 10 ml RBF and put under vacuum for 1 hour to dry. After filling the RBF with N₂, 2.5 ml dry DMSO stored over molecular sieves were added into the RBF. The reaction mixture was heated to 85 °C and refluxed for 20 min under N₂. TLC was used to confirm the completion of the reaction. After cooling down to RT, the reaction mixture was extracted with iced water and ethyl acetate. The organic layer was dried with MgSO₄, then evaporated under vacuum to give crude product. Purification by *Combiflash* using a Silica gel column yielded compound **6**. *EI-MS* Calculated m/z for C₇H₄FNO₃ Molecular Ion ([M]⁺): m/z=169, found m/z=169. ¹H NMR (400 MHz, CDCl₃): δ 10.45 (s, 1H), δ 8.16 (dd, J=8.6, 1.9 Hz), δ 8.11 – 8.07 (m, 2H). ¹⁹F NMR (400 MHz, CDCl₃): δ -117.43 (dd, J=10.2, 7.1 Hz).

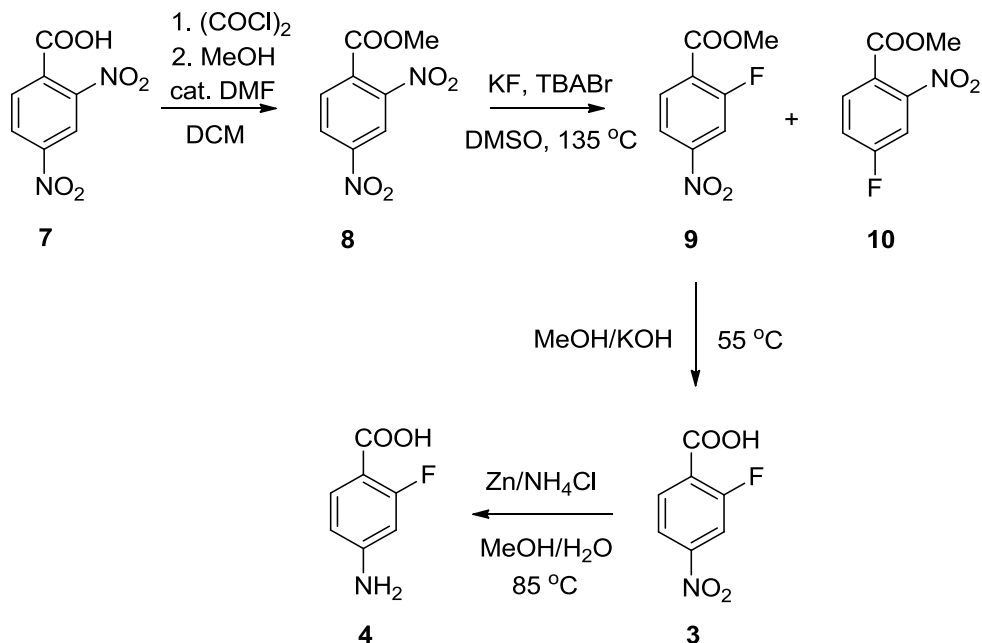
2-Fluoro-4-nitrobenzoic acid (3)

2, 4-Dinitrobenzaldehyde (**5**, 100 mg, 0.51 mmol) and oxone (30.35 mg, 0.12 mmol) were dissolved in 0.5 ml DMF. The reaction mixture was stirred at RT for 4 h. After TLC confirmed the reaction was completed, the pH of the reaction mixture was adjusted to 1 and the solution was extracted with iced water and ethyl acetate. The organic layer was dried with MgSO₄, then evaporated under vacuum to give crude product. Purification by *Combiflash* using a silica gel column yielded compound **3**. *ESI-MS* Calculated m/z for C₇H₄FNO₄ Molecular Ion [M-H]⁻ in negative mode is m/z=184.01, found m/z=184.01 for [M-H]⁻. ¹H NMR (400 MHz, CDCl₃ and CD₃OD): δ 8.23 – 8.19 (m, 1H), δ 8.12 – 8.09 (m, 1H), δ 8.06 – 8.03 (m, 1H). ¹⁹F NMR (400 MHz, CDCl₃ and CD₃OD): δ 103.68 (dd, J=10.12, 7.76 Hz) .

2-Fluoro-para-aminobenzoic acid (4)

The method 2-F-PABA was synthesized from 2-fluoro-4-nitrobenzoic acid was the same as what was used before in the synthesis of 2-F-PABA from 2, 4-dinitrobenzonitrile.

Synthesis of 2-F-PABA from 2, 4- Dinitrobenzoic acid



Scheme 5. 3 Synthesis of 2-F-PABA from 2, 4-dinitrobenzoic acid

Methyl 2,4-dinitrobenzoate (8)

2, 4-Dinitrobenzoic acid (**7**, 1 g, 4.71 mmol) was added to a 50 ml RBF and put under vacuum for 1 hour to dry. After filling the RBF with N₂, 10 ml dry dichloromethane and a drop of N,N-dimethylformamide were added into the RBF. Then 1.62 ml oxalyl chloride was added to the solution drop wise under N₂. The reaction mixture was stirred at RT for 2 hours. Then 2 mL methanol was added slowly into the reaction mixture, which was stirred at RT for 5 min. After TLC confirmed the reaction is completed, the solution was extracted with iced water and dichloromethane. The organic layer was dried with MgSO₄, then evaporated under vacuum to give crude product. Purification by *Combiflash* using a silica gel column yielded compound **8**. ¹H NMR (400Hz, CDCl₃): δ

8.81 (d, J=2.2 Hz, 1H), δ 8.55 (dd, J=8.4, 2.2 Hz, 1H), δ 7.95 (d, J=8.4 Hz, 1H), δ 4.00 (s, 3H).

Methyl 2-fluoro-4-nitrobenzoate (9) and methyl 2-nitro-4-fluorobenzoate (10).

Compound **8** (400 mg, 1.72 mmol), potassium fluoride (307.72 mg, 5.30 mmol) and tetrabutylammonium bromide (114.04 mg, 0.35 mmol) were added to a 25 mL RBF and put under vacuum for 1 hour to dry. After filling the RBF with N₂, 8 ml dry DMSO stored over molecular sieves was added into the RBF. The reaction mixture was heated to 135 °C and refluxed for 30 min under N₂. After TLC confirmed the reaction was completed, the reaction mixture was cooled down to RT, and was extracted with iced water and ethyl acetate. The organic layer was dried with MgSO₄, then evaporated under vacuum to give crude product. Purification by *Combiflash* using a silica gel column yielded mixture of compound **9** and **10**. The mixture was characterized by GC-EI-MS and NMR. The mixture can be further separated by silica gel column using *combiflash* to give pure compound **9** and **10**.

GC-MS: Two species were observed in the GC spectrum corresponding to the mixture of **9** and **10**, and both species gave two major ion peaks under EI-MS: m/z=190.00 for Molecular Ion C₈H₆FNO₄ [M]⁺⁺ and m/z=168.00 for fragment [M-CH₃O]⁺.

Compound **9**: ¹H NMR (400 MHz, CDCl₃): δ 8.14 (ddd, J=8.6, 6.6, 0.3 Hz, 1H), δ 8.08 (ddd, J=8.6, 2.1, 0.5 Hz, 1H), δ 8.02 (ddd, J=10.1, 2.1, 0.3 Hz, 1H), δ 4.00 (s, 3H). ¹⁹F

NMR (400 MHz, CDCl₃): δ 104.45 (dd, J=10.4, 6.8 Hz). **¹³C NMR** (400 MHz, CDCl₃): δ 164.70 (d, J=3.6 Hz), δ 162.73 (d, J=261.2 Hz), δ 152.72 (d), δ 134.47 (d, J=1.4 Hz), δ 125.67 (d, J=10.9 Hz), δ 120.24 (d, J=4.3 Hz), δ 113.90 (d, J=27.7 Hz), δ 53.50 (s).

Compound **10**: **¹H NMR** (400 MHz, CDCl₃): δ 7.83 (dd, J=8.6, 5.4 Hz, 1H), δ 7.58 (dd, J=7.8, 2.5 Hz, 1H), δ 7.02 (dd, J=8.6, 7.5, 2.5 Hz, 1H), δ 3.92 (s, 3H). **¹⁹F NMR** (400 MHz, CDCl₃): δ -103.58 – -103.63 (m).

2-Fluoro-4-nitrobenzoic acid (3)

40 mg compound **9** and KOH (22.54 mg, 0.40 mmol) were added to 10 ml RBF containing 2 ml MeOH. The reaction mixture was stirred for 30 min at 55 °C. After TLC confirmed the reaction was completed, the pH of the reaction mixture was adjusted to 1 and the solution was extracted with iced water and ethyl acetate. The organic layer was dried with MgSO₄, then evaporated under vacuum to give crude product. Purification by *Combiflash* using silica gel column yielded compound **3**. **ESI-MS** Calculated m/z for C₇H₄FNO₄ Molecular Ion [M-H]⁻ in negative mode is m/z=184.01, found m/z=184.01 for [M-H]⁻. Compound **3**: **¹H NMR** (400 MHz, CDCl₃ and CD₃OD) δ 8.16 (dd, J=8.6, 7.0 Hz, 1H), δ 8.07 (ddd, J=8.6, 2.1, 0.5 Hz, 1H), δ 8.01 (dd, J=9.9, 2.1 Hz, 1H). **¹⁹F NMR** (400 MHz, CDCl₃ and CD₃OD): δ -104.59 – -104.64 (m).

Commercially available standard 2-Fluoro-4-nitrobenzoic acid (3)

$^1\text{H NMR}$ (400 MHz, CDCl_3 and CD_3OD) δ 8.14 (dd, $J=8.6, 7.0\text{Hz}$, 1H), δ 8.06 (ddd, $J=8.6, 2.1, 0.8\text{ Hz}$, 1H), δ 8.00 (dd, $J=9.9, 2.1\text{ Hz}$, 1H). $^{19}\text{F NMR}$ (400 MHz, CDCl_3 and CD_3OD): δ 104.78 – 104.82 (m).

2-Fluoro-para-aminobenzoic acid (4)

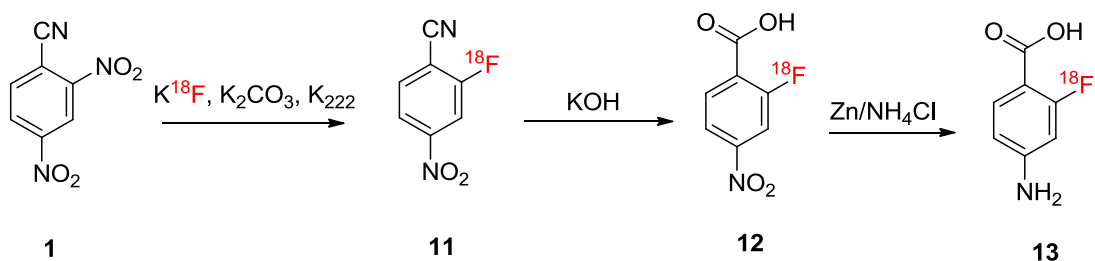
The method 2-F-PABA was synthesized from 2-fluoro-4-nitrobenzoic acid was the same as what was used before in the synthesis of 2-F-PABA from 2, 4-dinitrobenzotrile.

Radiochemistry

The radiochemistry was developed in Dr. Joanna Fowler's facility at Brookhaven National Laboratory with the help of Dr. Wenchao Qu, and technical assistance from Dr. Michael Schueller, Youwen Xu, and Colleen Shea. Analytical and preparative high performance liquid chromatography (HPLC) were performed using a Knauer HPLC system (Sonntek Inc., Woodcliff Lake, NJ, USA) equipped with a model K-5000 pump, a Rheodyne 7125 injector, a model 87 variable wavelength monitor, and a NaI radioactivity detector.

Among the three non-radioactive synthesis routes developed for 2-F-PABA (Scheme **5.1**, **5.2**, and **5.3**), the one that starts from 2,4-dinitrobenzotrile (compound **1**) was chosen

for radioactive chemistry development because compound **1** is a good combination of reactivity and stability compared to 2,4-dinitrobenzaldehyde (compound **5**, reactive but not stable) and 2,4-dinitrobenzoic acid (compound **7**, stable but not reactive). The scheme for radiosynthesis of 2-[¹⁸F]-PABA is shown in **Scheme 5.4**.



Scheme 5.4 Radiosynthesis of 2-[¹⁸F]-PABA

2-¹⁸F-4-nitrobenzonitrile (11)

Aqueous [¹⁸F]fluoride was produced by the ¹⁸O (p, n) ¹⁸F reaction. The fluoride activity was trapped in Kryptofix 2.2.2 (5 mg) and potassium carbonate (1 mg) in acetonitrile/water solution (950/50 μL), and dried by azeotropic distillation with aliquots of acetonitrile. The solid residue was resublimized with 0.2-0.3 mL of DMSO, containing a required amount of the precursor 2,4-dinitrobenzonitrile (compound **1**, 2mg). The reaction mixture was stirred by vortex and kept in sealed vial for 5 min at RT. The color of the reaction mixture changed from yellow to maroon. The formation of intermediate **11** was confirmed with a TLC scanner equipped with both UV and radioactivity detector, together with the byproduct: 4-¹⁸F-2-nitrobenzonitrile, characterized by both UV and radioactive R_f value on the TLC scanner (**Figure 5.3**).

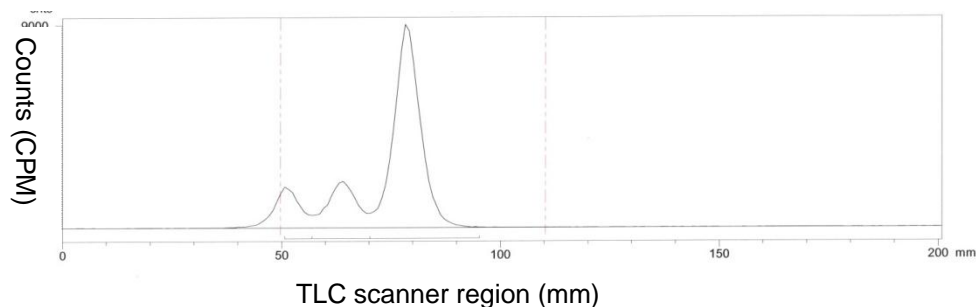


Figure 5. 3 Radio TLC result for formation of intermediate 11.

Major peak is 2-substitution product (71.69% conversion). Shift is consistent with cold standard UV.

2-¹⁸F-4-Nitrobenzoicacid (12)

The reaction mixture from the first step was loaded onto a C18 light sep-pack, which was pre-activated with 5 mL acetonitrile and 10 mL H₂O. Then 10 mL H₂O was used to wash the C18 light sep-pack to elute unreacted fluoride and other water-soluble impurities.

After that, 0.3 mL methanol was used to elute the intermediate **11** into a vial which contains 1 mL 2M KOH solution. The reaction mixture was heated to 105 °C and stirred for 10 min, then quenched with 3 mL H₂O. The formation of intermediate 12 is confirmed with TLC scanner equipped with both UV and radioactivity detector, characterized by both UV and radioactive R_f value on the TLC scanner (**Figure 5.4**).

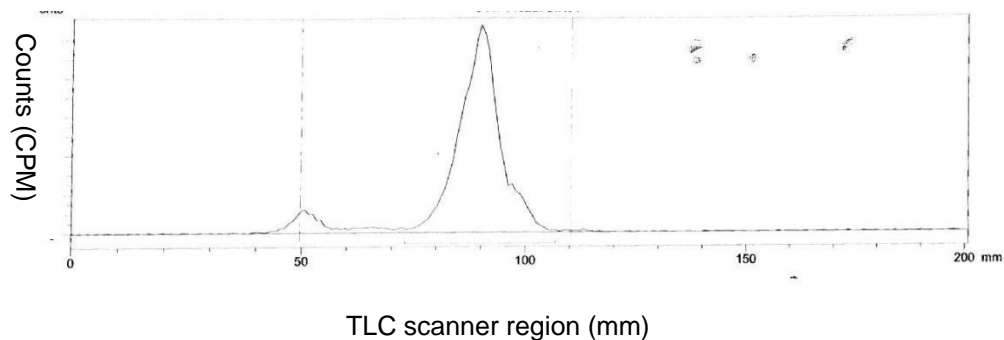


Figure 5. 4 Radio TLC result for formation of intermediate **12.**

Major peak is 2-¹⁸F-4-nitrobenzoicacid **12** (91.67% conversion). Shift is consistent with cold standard UV.

2-¹⁸F-para-aminobenzoicacid (13**, 2-[¹⁸F]-PABA)**

The reaction mixture from step 2 was loaded into a C18 light sep-pack for concentration, and also getting rid of excess KOH solution which will be toxic to the subsequent reduction reaction. Then, 0.3 mL MeOH was used to elute intermediate **12** into a vial containing Zn powder (3.6 mg) and NH₄Cl (4.5 mg) in 1mL H₂O. The reaction mixture was heated to 105 °C, stirred for 5 min, and then filtered using an injection filter (RC membrane, 0.45 μm), after which it was loaded into a reversed-phase analytical HPLC using a Phenomenex, Luna PFP, 250×4.6, 5 μm column operated at 1.0 mL/min flow rate using a mobile phase of (1) 18% Acetonitrile/H₂O (0.05% TFA) with 7.5 min retention time; or (2) 15% Methanol/H₂O (0.05% TFA), with 18 min retention time. Two different analytical HPLC system with different retention time for the product, each showed the same UV and radioactivity retention time respectively, were employed here to confirm the formation of 2-[¹⁸F]-PABA.

MIC screen

Minimum inhibitory concentrations (MIC) for *M. tuberculosis* was determined by Dr. Xinxin Yang, for *E. coli*, *P aeruginosa*, *K pneumoniae*, and *S. aureus*. were determined by Chendi Gu.

MIC determination for *M. tuberculosis*. The MIC was determined by the broth dilution method. Middlebrook 7H9 broth supplemented with 0.05% Tween-80, 0.2% glycerol, and albumin/NaCl/glucose (ADC) complex containing serial two-fold concentrations of PAS, PABA, and F-PABA ranging from 100 to 0.1 μ M were inoculated with 0.1 mL of the 1000 fold dilution of a log phase broth culture of *M. tuberculosis H37Rv*. The MIC was defined as the lowest concentration at which no visible growth was observed after 14 days incubation at 37°C.

MIC determination for other strains. MICs were determined in duplicate by broth microdilution. Briefly, compounds were dissolved in DMSO to get the stock solutions of 10 mg drug/ mL. 2-fold dilution series covering 200 to 0.39 μ g drug/mL at 1% final DMSO were prepared by diluting the stock solutions in 100 μ L cation adjusted Mueller Hinton II broth. 100 μ L of cells in the logarithmic phase were then added to the drug-containing media to a final concentration of 5×10^5 CFU/mL and were incubated at 37 °C overnight. The MIC was recorded the next day as the lowest concentration of drug which prevented visible growth under the condition of the test.

Results and Discussions

Chemistry

Three different schemes were developed and evaluated for the purpose of synthesis of non-radioactive 2-F-PABA. The first scheme starts with 2, 4-dinitrobenzonitrile (**1**). Fluorination of **1** completes within 30 minutes at the temperature of 85 °C, which is fast enough for radioactive synthesis. Two regioisomers (2-fluoro-4-nitrobenzonitrile **2** and 2-nitro-4-fluorobenzonitrile) were produced in the fluorination step. They can be separated by silica gel column chromatography. Two regioisomers were identified after hydrolysis by comparing to standard 2-fluoro-4-nitrobenzoic acid (**3**) which is commercially available. The hydrolysis of **2** is relatively slow at 40 °C, which takes about 4 hours. Further increase in temperature results in a reduced yield of **3**. At 80 °C, no formation of **3** was observed on TLC likely because the 5' fluorine is not stable under basic conditions. However, hydrolysis of **2** under acidic conditions (HCl solution and HBr solution) was even slower. Although the last reduction step is fast and clean (the reaction completes in 30 minutes at 80 °C), the slow hydrolysis step of this method might limit its application in radiosynthesis.

2, 4-Dinitrobenzaldehyde (**5**) was used as the starting material for the second scheme. Fluorination of **5** is fast at 85 °C, and is completed within 20 min. For some reason, 2-fluoro-4-nitrobenzaldehyde is the major product while its regioisomer 2-nitro-4-fluorobenzaldehyde is the minor product. Also, the two regioisomers can be separated by silica gel column chromatography and their structures were determined by comparison to

standard 2-fluoro-4-nitrobenzoic acid after hydrolysis. Although the first step is fast, the second oxidation step is relatively slow and takes about 2 hours to complete. In addition 2, 4-dinitrobenzaldehyde (**5**) was found to be unstable hence difficult to handle.

Therefore, this scheme was left to be the alternative plan for radiolabelling PABA.

The third scheme involved the fluorination of methyl 2, 4-dinitrobenzoate (**8**). As expected, two regioisomers **9** and **10** were produced. Due to steric hinderance of the ortho position, **9** is the minor product. To optimize the fluorination reaction, reaction mixtures were heated to different temperatures. As the temperature was incereased, the time needed for all starting material to be consumed became shorter. However, as temperature was over 135 °C, the yield of methyl 2-fluoro-4-nitrobenzoate (**9**) was reduced. The ratio of **10** to **9** was about 2 at 135 °C. According to ¹H NMR, **9** and **10** cannot be separated by silica gel column. However, their responding products after hydrolysis can be separated by silica gel column. The following hydrolysis and reduction are fast, and complete in 20 min and 30 min, respectively.

Taken together, the first scheme was chosen to be further used in the radiosynthesis of 2-[¹⁸F]F-PABA, because compound **1** is a good combination of reactivity and stability compared to 2,4-dinitrobenzaldehyde (compound **5**, reactive but not stable) and 2,4-dinitrobenzoic acid (compound **7**, stable but not reactive).

Radiochemistry

The radiosynthesis for 2-[¹⁸F]-PABA (**Scheme 5.4**) is based on the corresponding non-radioactive synthesis route (**Scheme 5.1**). The characterization of first two steps were conducted by TLC scanner equipped with both UV and radioactivity detector. Because this reaction contains regioisomers which have similar retention times as the desired product, two different analytical HPLC systems were employed to characterize the final product formation. In **Figure 5.5**, each analytical HPLC system shows that the radioactivity signal coincides with the UV signal of the non-radioactive standard compound.

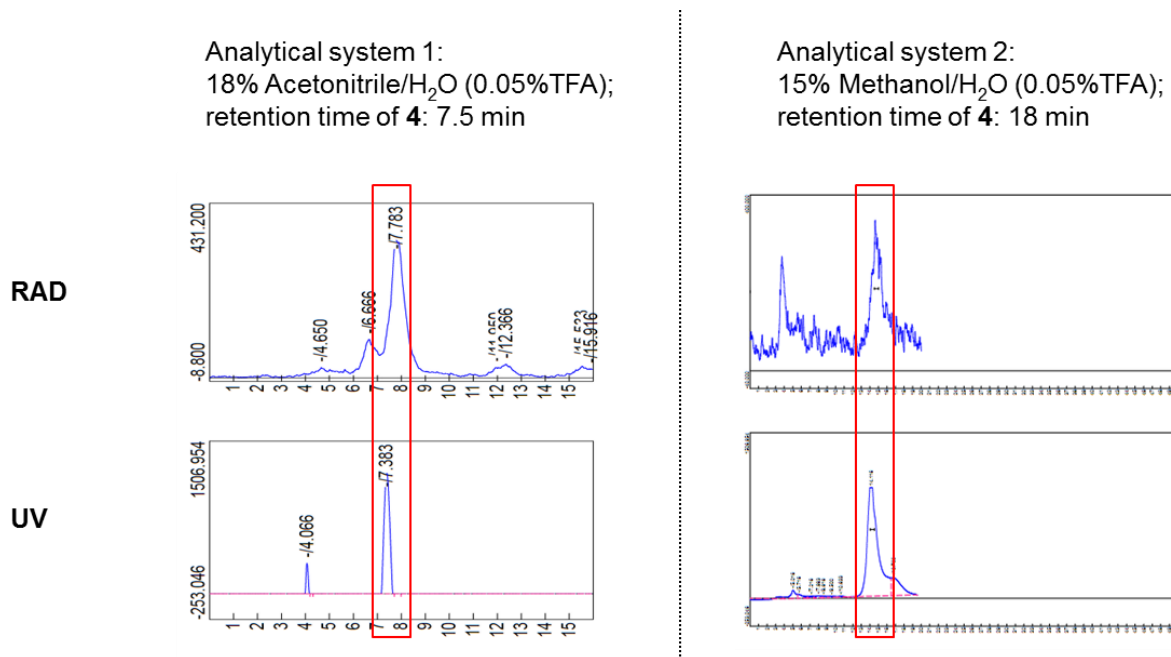


Figure 5. 5 Two analytical HPLC system, each shows the formation of final product 2-[¹⁸F]-PABA with different retention time.

Because the radiosynthesis route for 2-[¹⁸F]-PABA includes two more steps after fluorination step, the over yield is inherently low. In order improve the yield of the radiosynthesis, a new solid-phase extraction sep-pack (Oasis HLC sep-pack, Waters) was applied to intermediate **12** and compared to traditional C18 light sep-pack (**Table 5.1**). As a result, the trapping efficiency for intermediate **12** was improved 3 fold by using the Oasis HLB cartridge.

Table 5. 1 Comparison of trapping efficiency for intermediate 12 using two different solid-phase extraction products

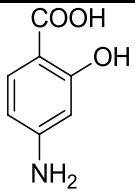
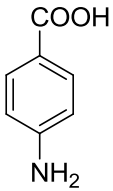
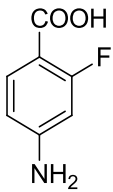
Cartridge	C18 sep-pack	OASIS HLB cartridge
Radioactivity loaded to the cartridge	88 µCi	85 µCi
Radioactivity trapped on the cartridge	20 µCi	54 µCi
Trapping efficiency	22.7%	63.5%

MIC screen result

The Minimum Inhibitory Concentrations (MIC) of compound PAS, PABA, and 2-F-PABA have been determined against *M. tuberculosis*, *E. coli*, *P aeruginosa*, *K*

pneumoniae, and *S. aureus*. *M. tuberculosis* H37Rv growth was inhibited by PAS with an MIC of 1 μ M, consistent with previous reports (245, 246), but not inhibited by PABA or 2-F-PABA. As to other bacteria species tested, none of the compounds showed inhibition up to 200 μ g/mL. Taken together, these results indicate that PAS is a narrow-spectrum antibiotic for *M. tuberculosis* (248).

Table 5. 2 MIC screen results for PABA, PAS, and 2-F-PABA

NAME	STRUCTURES	MIC					
		<i>M. tb</i> H37Rv	<i>E.coli</i> MG1655	<i>P. aeruginosa</i> PAO1	<i>K. pneumoniae</i> ATCC 13883	<i>S. aureus</i> Newmann 1762 (MRSA)	<i>S. aureus</i> ATCC BAA 1762 (MRSA)
PAS		1 μ M	>200 μ g/mL	>200 μ g/mL	>200 μ g/mL	>200 μ g/mL	>200 μ g/mL
PABA		>100 μ M	>200 μ g/mL	>200 μ g/mL	>200 μ g/mL	>200 μ g/mL	>200 μ g/mL
2-F-PABA		>100 μ M	>200 μ g/mL	>200 μ g/mL	>200 μ g/mL	>200 μ g/mL	>200 μ g/mL

*MIC for *M. tb* was determined by Dr. Xinxin Yang, for other bacteria species were determined by Chendi Gu.

Conclusion

In summary, we have identified PABA as a molecule of interest for radiolabelling with PET fluorine-18 isotope. Based on the structural similarity of 2-F-PABA to PABA and PAS (the latter is also sequestered into folate biosynthesis pathway in a similar mechanism to PABA), 2-[¹⁸F]-PABA is proposed to be a promising PET imaging radiotracer to detect bacterial infection in human patients. We have developed three nonradioactive synthesis routes for 2-F-PABA, one of which is selected to proceed to radiosynthesis based on its merit of both reactivity and stability. Finally, we successfully incorporated fluorine-18 into PABA and optimized the overall reaction yield by 3-fold (from 15% to 45%, decay corrected).

Bibliography

1. Phelps ME, Mazziotta JC. Positron emission tomography: human brain function and biochemistry. *Science*. 1985;228(4701):799-809.
2. Fowler JS, Wolf AP. Working against time: Rapid radiotracer synthesis and imaging the human brain. *Accounts Chem Res*. 1997;30(4):181-8.
3. Miller PW, Long NJ, Vilar R, Gee AD. Synthesis of C-11, F-18, O-15, and N-13 Radiolabels for Positron Emission Tomography. *Angew Chem Int Edit*. 2008;47(47):8998-9033.
4. Phelps ME, Hoffman EJ, Mullani NA, Ter-Pogossian MM. Application of annihilation coincidence detection to transaxial reconstruction tomography. *J Nucl Med*. 1975;16(3):210-24.
5. Phelps ME, Hoffman EJ, Coleman RE, Welch MJ, Raichle ME, Weiss ES, et al. Tomographic images of blood pool and perfusion in brain and heart. *J Nucl Med*. 1976;17(7):603-12.
6. Hoffmann EJ, Phelps ME, Mullani NA, Higgins CS, Ter-Pogossian MM. Design and performance characteristics of a whole-body positron transaxial tomograph. *J Nucl Med*. 1976;17(6):493-502.
7. Cho Z, Chan JK, Hall EL, Kruger RP, Mccaughey DG. Comparative-Study of 3-D Image-Reconstruction Algorithms with Reference to Number of Projections and Noise Filtering. *Int J Nucl Med Biol*. 1976;3(3-4):163-5.
8. Phelps ME. Positron emission tomography provides molecular imaging of biological processes. *Proc Natl Acad Sci U S A*. 2000;97(16):9226-33. PMID: 16850.

9. Turkington TG. Introduction to PET instrumentation. *J Nucl Med Technol.* 2001;29(1):4-11.
10. Townsend DW, Cherry SR. Combining anatomy and function: the path to true image fusion. *Eur Radiol.* 2001;11(10):1968-74.
11. Charron M, Beyer T, Bohnen NN, Kinahan PE, Dachille M, Jerin J, et al. Image analysis in patients with cancer studied with a combined PET and CT scanner. *Clin Nucl Med.* 2000;25(11):905-10.
12. Beyer T, Townsend DW, Brun T, Kinahan PE, Charron M, Roddy R, et al. A combined PET/CT scanner for clinical oncology. *J Nucl Med.* 2000;41(8):1369-79.
13. Blodgett TM, Meltzer CC, Townsend DW. PET/CT: form and function. *Radiology.* 2007;242(2):360-85.
14. Ryan KJ, Ray CG, Sherris JC. *Sherris medical microbiology : an introduction to infectious diseases.* 4th ed. New York: McGraw-Hill; 2004.
15. Gotthardt M, Bleeker-Rovers CP, Boerman OC, Oyen WJ. Imaging of inflammation by PET, conventional scintigraphy, and other imaging techniques. *J Nucl Med Technol.* 2013;41(3):157-69.
16. Bleeker-Rovers CP, Boerman OC, Rennen HJJM, Corstens FHM, Oyen WJG. Radiolabeled compounds in diagnosis of infectious and inflammatory disease. *Curr Pharm Design.* 2004;10(24):2935-50.
17. Boss DS, Olmos RV, Sinaasappel M, Beijnen JH, Schellens JH. Application of PET/CT in the development of novel anticancer drugs. *Oncologist.* 2008;13(1):25-38.

18. Kumar R, Basu S, Torigian D, Anand V, Zhuang H, Aavi A. Role of modern imaging techniques for diagnosis of infection in the era of F-18-fluorodeoxyglucose positron emission tomography. *Clinical Microbiology Reviews*. 2008;21(1):209.
19. Ido T, Wan CN, Casella V, Fowler JS, Wolf AP, Reivich M, et al. Labeled 2-Deoxy-D-Glucose Analogs - F-18-Labeled 2-Deoxy-2-Fluoro-D-Glucose, 2-Deoxy-2-Fluoro-D-Mannose and C-14-2-Deoxy-2-Fluoro-D-Glucose. *J Labelled Compd Rad*. 1978;14(2):175-83.
20. Alavi A, Dann R, Chawluk J, Alavi J, Kushner M, Reivich M. Positron emission tomography imaging of regional cerebral glucose metabolism. *Semin Nucl Med*. 1986;16(1):2-34.
21. Alavi A, Kramer E, Wegener W, Alavi J. Magnetic resonance and fluorine-18 deoxyglucose imaging in the investigation of a spinal cord tumor. *J Nucl Med*. 1990;31(3):360-4.
22. Alavi A, Newberg AB, Souder E, Berlin JA. Quantitative analysis of PET and MRI data in normal aging and Alzheimer's disease: atrophy weighted total brain metabolism and absolute whole brain metabolism as reliable discriminators. *J Nucl Med*. 1993;34(10):1681-7.
23. Alavi A, Reivich M, Ferris S, Christman D, Fowler J, MacGregor R, et al. Regional cerebral glucose metabolism in aging and senile dementia as determined by 18F-deoxyglucose and positron emission tomography. *Exp Brain Res*. 1982;Suppl 5:187-95.
24. Reif AE, Potter VR, Lepage GA. Aerobic glycolysis in homogenates of normal and tumor tissues. *Cancer Res*. 1953;13(11):807-16.

25. Warburg O. Note on the metabolism of tumours. *Biochem Z.* 1930;228:257-8.
26. Fuster D, Chiang S, Johnson G, Schuchter LM, Zhuang HM, Alavi A. Is F-18-FDG PET more accurate than standard diagnostic procedures in the detection of suspected recurrent melanoma? *J Nucl Med.* 2004;45(8):1323-7.
27. Isasi CR, Lu P, Blafox MD. A metaanalysis of 18F-2-deoxy-2-fluoro-D-glucose positron emission tomography in the staging and restaging of patients with lymphoma. *Cancer.* 2005;104(5):1066-74.
28. Kumar R, Xiu Y, Yu JQ, Takalkar A, El-Haddad G, Potenta S, et al. 18F-FDG PET in evaluation of adrenal lesions in patients with lung cancer. *J Nucl Med.* 2004;45(12):2058-62.
29. Kumar R, Xiu Y, Potenta S, Mavi A, Zhuang H, Yu JQ, et al. 18F-FDG PET for evaluation of the treatment response in patients with gastrointestinal tract lymphomas. *J Nucl Med.* 2004;45(11):1796-803.
30. Zhuang H, Kumar R, Mandel S, Alavi A. Investigation of thyroid, head, and neck cancers with PET. *Radiol Clin North Am.* 2004;42(6):1101-11, viii.
31. De Winter F, Vogelaers D, Gemmel F, Dierckx RA. Promising role of 18-F-fluoro-D-deoxyglucose positron emission tomography in clinical infectious diseases. *Eur J Clin Microbiol Infect Dis.* 2002;21(4):247-57.
32. Haroon A, Zumla A, Bomanji J. Role of fluorine 18 fluorodeoxyglucose positron emission tomography-computed tomography in focal and generalized infectious and inflammatory disorders. *Clin Infect Dis.* 2012;54(9):1333-41.

33. Revest M, Patrat-Delon S, Devillers A, Tattevin P, Michelet C. Contribution of 18fluoro-deoxyglucose PET/CT for the diagnosis of infectious diseases. *Med Mal Infect.* 2014;44(6):251-60.
34. Chakrabarti R, Jung CY, Lee TP, Liu H, Mookerjee BK. Changes in glucose transport and transporter isoforms during the activation of human peripheral blood lymphocytes by phytohemagglutinin. *J Immunol.* 1994;152(6):2660-8.
35. Miyamoto M, Sato EF, Nishikawa M, Nishizawa Y, Morii H, Inoue M. Effect of endogenously generated nitric oxide on the energy metabolism of peritoneal macrophages. *Physiol Chem Phys Med NMR.* 2003;35(1):1-11.
36. Sorbara LR, Maldarelli F, Chamoun G, Schilling B, Chokekijcahi S, Staudt L, et al. Human immunodeficiency virus type 1 infection of H9 cells induces increased glucose transporter expression. *J Virol.* 1996;70(10):7275-9. PMID: 190788.
37. Yamada S, Kubota K, Kubota R, Ido T, Tamahashi N. High accumulation of fluorine-18-fluorodeoxyglucose in turpentine-induced inflammatory tissue. *J Nucl Med.* 1995;36(7):1301-6.
38. Kubota R, Yamada S, Kubota K, Ishiwata K, Tamahashi N, Ido T. Intratumoral distribution of fluorine-18-fluorodeoxyglucose in vivo: high accumulation in macrophages and granulation tissues studied by microautoradiography. *J Nucl Med.* 1992;33(11):1972-80.
39. Conrad GR, Sinha P. Narrow time-window dual-point 18F-FDG PET for the diagnosis of thoracic malignancy. *Nucl Med Commun.* 2003;24(11):1129-37.

40. Xiu Y, Bhutani C, Dhurairaj T, Yu JQ, Dadparvar S, Reddy S, et al. Dual-time point FDG PET imaging in the evaluation of pulmonary nodules with minimally increased metabolic activity. *Clin Nucl Med.* 2007;32(2):101-5.
41. Bhutani C, Yu JQ, Bhargava P, Zhuang HM, Alavi A. Dual-time point FDG-PET imaging in the evaluation of pulmonary nodules with borderline level of increased FDG uptake. *J Nucl Med.* 2003;44(5):181.
42. de Winter F, van de Wiele C, Vogelaers D, de Smet K, Verdonk R, Dierckx RA. Fluorine-18 fluorodeoxyglucose-position emission tomography: a highly accurate imaging modality for the diagnosis of chronic musculoskeletal infections. *J Bone Joint Surg Am.* 2001;83-A(5):651-60.
43. Boulton AJ. The diabetic foot: a global view. *Diabetes Metab Res Rev.* 2000;16 Suppl 1:S2-5.
44. Lipsky BA. A report from the international consensus on diagnosing and treating the infected diabetic foot. *Diabetes Metab Res Rev.* 2004;20 Suppl 1:S68-77.
45. Schinabeck MK, Johnson JL. Osteomyelitis in diabetic foot ulcers. Prompt diagnosis can avert amputation. *Postgrad Med.* 2005;118(1):11-5.
46. Williams DT, Hilton JR, Harding KG. Diagnosing foot infection in diabetes. *Clin Infect Dis.* 2004;39 Suppl 2:S83-6.
47. Basu S, Chryssikos T, Houseni M, Scot Malay D, Shah J, Zhuang H, et al. Potential role of FDG PET in the setting of diabetic neuro-osteoarthropathy: can it differentiate uncomplicated Charcot's neuroarthropathy from osteomyelitis and soft-tissue infection? *Nucl Med Commun.* 2007;28(6):465-72.

48. Zhuang H, Duarte PS, Pourdehnad M, Maes A, Van Acker F, Shnier D, et al. The promising role of 18F-FDG PET in detecting infected lower limb prosthesis implants. *J Nucl Med.* 2001;42(1):44-8.
49. Petersdorf RG, Beeson PB. Fever of unexplained origin: report on 100 cases. *Medicine (Baltimore).* 1961;40:1-30.
50. Petersdorf RG. Fever of unknown origin. An old friend revisited. *Arch Intern Med.* 1992;152(1):21-2.
51. Bleeker-Rovers CP, Vos FJ, de Kleijn EMHA, Mudde AH, Dofferhoff TSM, Richter C, et al. A prospective multicenter study on fever of unknown origin - The yield of a structured diagnostic protocol. *Medicine.* 2007;86(1):26-38.
52. Blockmans D, Knockaert D, Maes A, De Caestecker J, Stroobants S, Bobbaers H, et al. Clinical value of [(18)F]fluoro-deoxyglucose positron emission tomography for patients with fever of unknown origin. *Clin Infect Dis.* 2001;32(2):191-6.
53. Stumpe KDM, Dazzi H, Schaffner A, von Schulthess GK. Infection imaging using whole-body FDG-PET. *Eur J Nucl Med.* 2000;27(7):822-32.
54. Rohde H, Horstkotte MA, Loeper S, Aberle J, Jenicke L, Lampidis R, et al. Recurrent *Listeria monocytogenes* aortic graft infection: confirmation of relapse by molecular subtyping. *Diagn Micr Infec Dis.* 2004;48(1):63-7.
55. Krupnick AS, Lombardi JV, Engels FH, Kreisel D, Zhuang H, Alavi A, et al. 18-fluorodeoxyglucose positron emission tomography as a novel imaging tool for the diagnosis of aortoenteric fistula and aortic graft infection--a case report. *Vasc Endovascular Surg.* 2003;37(5):363-6.

56. Pabst T, Kenn W, Kaiser WA, Hahn D. Understanding why contrast enhancement in dynamic MRI is not reproducible: illustration with a simple phantom. *Breast J*. 2001;7(3):166-70.
57. Chen DL, Ferkol TW, Mintun MA, Pittman JE, Rosenbluth DB, Schuster DP. Quantifying pulmonary inflammation in cystic fibrosis with positron emission tomography. *Am J Respir Crit Care Med*. 2006;173(12):1363-9. PMID: 2662975.
58. Gungor T, Engel-Bicik I, Eich G, Willi UV, Nadal D, Hossle JP, et al. Diagnostic and therapeutic impact of whole body positron emission tomography using fluorine-18-fluoro-2-deoxy-D-glucose in children with chronic granulomatous disease. *Arch Dis Child*. 2001;85(4):341-5. PMID: 1718940.
59. Ozsahin H, von Planta M, Muller I, Steinert HC, Nadal D, Lauener R, et al. Successful treatment of invasive aspergillosis in chronic granulomatous disease by bone marrow transplantation, granulocyte colony-stimulating factor-mobilized granulocytes, and liposomal amphotericin-B. *Blood*. 1998;92(8):2719-24.
60. Li JS, Sexton DJ, Mick N, Nettles R, Fowler VG, Jr., Ryan T, et al. Proposed modifications to the Duke criteria for the diagnosis of infective endocarditis. *Clin Infect Dis*. 2000;30(4):633-8.
61. Vieira ML, Grinberg M, Pomerantzeff PM, Andrade JL, Mansur AJ. Repeated echocardiographic examinations of patients with suspected infective endocarditis. *Heart*. 2004;90(9):1020-4. PMID: 1768449.
62. Saby L, Laas O, Habib G, Cammilleri S, Mancini J, Tessonnier L, et al. Positron emission tomography/computed tomography for diagnosis of prosthetic valve

endocarditis: increased valvular 18F-fluorodeoxyglucose uptake as a novel major criterion. *J Am Coll Cardiol.* 2013;61(23):2374-82.

63. Sarrazin JF, Philippon F, Tessier M, Guimond J, Molin F, Champagne J, et al. Usefulness of fluorine-18 positron emission tomography/computed tomography for identification of cardiovascular implantable electronic device infections. *J Am Coll Cardiol.* 2012;59(18):1616-25.

64. Who. Global Tuberculosis Report 2012. *Global Tuberculosis Report 2012.* 2012:1-272.

65. Williams C. Global Tuberculosis Control: WHO Report 2011. *Aust Nz J Publ Heal.* 2012;36(5):497-8.

66. Martinez V, Castilla-Lievre MA, Guillet-Caruba C, Grenier G, Fior R, Desarnaud S, et al. F-18-FDG PET/CT in tuberculosis: an early non-invasive marker of therapeutic response. *Int J Tuberc Lung D.* 2012;16(9):1180-5.

67. Demura Y, Tsuchida T, Uesaka D, Umeda Y, Morikawa M, Ameshima S, et al. Usefulness of 18F-fluorodeoxyglucose positron emission tomography for diagnosing disease activity and monitoring therapeutic response in patients with pulmonary mycobacteriosis. *Eur J Nucl Med Mol Imaging.* 2009;36(4):632-9.

68. Bakheet SM, Powe J, Ezzat A, Rostom A. F-18-FDG uptake in tuberculosis. *Clin Nucl Med.* 1998;23(11):739-42.

69. Goo JM, Im JG, Do KH, Yeo JS, Seo JB, Kim HY, et al. Pulmonary tuberculoma evaluated by means of FDG PET: findings in 10 cases. *Radiology.* 2000;216(1):117-21.

70. Kim IJ, Lee JS, Kim SJ, Kim YK, Jeong YJ, Jun S, et al. Double-phase 18F-FDG PET-CT for determination of pulmonary tuberculoma activity. *Eur J Nucl Med Mol Imaging*. 2008;35(4):808-14.
71. M. S. Sonnenberg JEB, G. L. Mandell, R. Dolin, Eds. Mandell, Douglas, and Bennett's Principles and Practice of Infectious Diseases. Philadelphia, PA: Elsevier Inc.; 2010.
72. Li ZB, Wu Z, Cao Q, Dick DW, Tseng JR, Gambhir SS, et al. The synthesis of 18F-FDS and its potential application in molecular imaging. *Mol Imaging Biol*. 2008;10(2):92-8. PMID: 4143166.
73. Weinstein EA, Ordonez AA, DeMarco VP, Murawski AM, Pokkali S, MacDonald EM, et al. Imaging Enterobacteriaceae infection in vivo with 18F-fluorodeoxyisobutyl positron emission tomography. *Sci Transl Med*. 2014;6(259):259ra146.
74. Solanki KK, Mather SJ, Janabi MA, Britton KE. A rapid method for the preparation of ⁹⁹Tc hexametazime-labelled leucocytes. *Nucl Med Commun*. 1988;9(10):753-61.
75. Tewson TJ, Yang D, Wong G, Macy D, DeJesus OJ, Nickles RJ, et al. The synthesis of fluorine-18 lomefloxacin and its preliminary use in human studies. *Nucl Med Biol*. 1996;23(6):767-72.
76. Anderson VE, Osheroff N. Type II topoisomerases as targets for quinolone antibacterials: turning Dr. Jekyll into Mr. Hyde. *Curr Pharm Des*. 2001;7(5):337-53.
77. Pan XS, Yague G, Fisher LM. Quinolone resistance mutations in *Streptococcus pneumoniae* GyrA and ParC proteins: mechanistic insights into quinolone action from

enzymatic analysis, intracellular levels, and phenotypes of wild-type and mutant proteins.

Antimicrob Agents Chemother. 2001;45(11):3140-7. PMID: 90795.

78. Britton KE, Wareham DW, Das SS, Solanki KK, Amaral H, Bhatnagar A, et al.

Imaging bacterial infection with (99m)Tc-ciprofloxacin (Infecton). *J Clin Pathol.*

2002;55(11):817-23. PMID: 1769796.

79. Das SS, Wareham DW, Britton KE. 99mTc-labeled antimicrobial peptides for

detection of bacterial and *Candida albicans* infections. *J Nucl Med.* 2002;43(8):1125;

author reply 6-7.

80. Sarda L, Saleh-Mghir A, Peker C, Meulemans A, Cremieux AC, Le Guludec D.

Evaluation of (99m)Tc-ciprofloxacin scintigraphy in a rabbit model of *Staphylococcus aureus* prosthetic joint infection. *J Nucl Med.* 2002;43(2):239-45.

81. Dumarey N, Blocklet D, Appelboom T, Tant L, Schoutens A. Infecton is not

specific for bacterial osteo-articular infective pathology. *Eur J Nucl Med Mol Imaging.*

2002;29(4):530-5.

82. Langer O, Mitterhauser M, Brunner M, Zeitlinger M, Wadsak W, Mayer BX, et

al. Synthesis of fluorine-18-labeled ciprofloxacin for PET studies in humans. *Nucl Med Biol.* 2003;30(3):285-91.

83. Babich JW, Rubin RH, Graham WA, Wilkinson RA, Vincent J, Fischman AJ.

18F-labeling and biodistribution of the novel fluoro-quinolone antimicrobial agent,

trovafloxacin (CP 99,219). *Nucl Med Biol.* 1996;23(8):995-8.

84. Fischman AJ, Babich JW, Alpert NM, Vincent J, Wilkinson RA, Callahan RJ, et

al. Pharmacokinetics of 18F-labeled trovafloxacin in normal and *Escherichia coli*-

- infected rats and rabbits studied with positron emission tomography. *Clin Microbiol Infect.* 1997;3(1):63-72.
85. Zasloff M. Antimicrobial peptides of multicellular organisms. *Nature.* 2002;415(6870):389-95.
86. Akhtar MS, Imran MB, Nadeem MA, Shahid A. Antimicrobial peptides as infection imaging agents: better than radiolabeled antibiotics. *Int J Pept.* 2012;2012:965238. PMID: 3362861.
87. Ganz T, Lehrer RI. Defensins. *Curr Opin Immunol.* 1994;6(4):584-9.
88. Welling MM, Nibbering PH, Paulusma-Annema A, Hiemstra PS, Pauwels EK, Calame W. Imaging of bacterial infections with ^{99m}Tc-labeled human neutrophil peptide-1. *J Nucl Med.* 1999;40(12):2073-80.
89. Welling MM, Mongera S, Lupetti A, Balter HS, Bonetto V, Mazzi U, et al. Radiochemical and biological characteristics of ^{99m}Tc-UBI 29-41 for imaging of bacterial infections. *Nucl Med Biol.* 2002;29(4):413-22.
90. Akhtar MS, Khan ME, Khan B, Irfanullah J, Afzal MS, Khan MA, et al. An imaging analysis of (^{99m}Tc-UBI (29-41) uptake in *S. aureus* infected thighs of rabbits on ciprofloxacin treatment. *Eur J Nucl Med Mol Imaging.* 2008;35(6):1056-64.
91. IM R. *Essential Immunology.* 9th ed: Oxford: Blackwell Scientific; 1997.
92. Proud D, Kaplan AP. Kinin formation: mechanisms and role in inflammatory disorders. *Annu Rev Immunol.* 1988;6:49-83.
93. Weiner R. The role of transferrin and other receptors in the mechanism of ⁶⁷Ga localization. *Int J Rad Appl Instrum B.* 1990;17(1):141-9.

94. Bekerman C, Hoffer PB, Bitran JD. The role of gallium-67 in the clinical evaluation of cancer. *Semin Nucl Med.* 1984;14(4):296-323.
95. Fischman AJ, Rubin RH, White JA, Locke E, Wilkinson RA, Nedelman M, et al. Localization of Fc and Fab fragments of nonspecific polyclonal IgG at focal sites of inflammation. *J Nucl Med.* 1990;31(7):1199-205.
96. Dams ET, Oyen WJ, Boerman OC, Claessens RA, Wymenga AB, van der Meer JW, et al. Technetium-99m labeled to human immunoglobulin G through the nicotinyl hydrazine derivative: a clinical study. *J Nucl Med.* 1998;39(1):119-24.
97. Morgan JR, Williams LA, Howard CB. Technetium-labelled liposome imaging for deep-seated infection. *Br J Radiol.* 1985;58(685):35-9.
98. Oyen WJ, Boerman OC, Storm G, van Bloois L, Koenders EB, Crommelin DJ, et al. Labelled Stealth liposomes in experimental infection: an alternative to leukocyte scintigraphy? *Nucl Med Commun.* 1996;17(9):742-8.
99. Oyen WJ, Boerman OC, Storm G, van Bloois L, Koenders EB, Claessens RA, et al. Detecting infection and inflammation with technetium-99m-labeled Stealth liposomes. *J Nucl Med.* 1996;37(8):1392-7.
100. Rusckowski M, Fritz B, Hnatowich DJ. Localization of infection using streptavidin and biotin: an alternative to nonspecific polyclonal immunoglobulin. *J Nucl Med.* 1992;33(10):1810-5.
101. Mardirossian G, Wu C, Rusckowski M, Hnatowich DJ. The stability of ⁹⁹Tcm directly labelled to an Fab' antibody via stannous ion and mercaptoethanol reduction. *Nucl Med Commun.* 1992;13(7):503-12.

102. Weiner RE, Sasso DE, Gionfriddo MA, Thrall RS, Syrbu S, Smilowitz HM, et al. Early detection of oleic acid-induced lung injury in rats using (111)In-labeled anti-rat intercellular adhesion molecule-1. *J Nucl Med.* 2001;42(7):1109-15.
103. Weiner RE, Sasso DE, Gionfriddo MA, Syrbu SI, Smilowitz HM, Vento J, et al. Early detection of bleomycin-induced lung injury in rat using indium-111-labeled antibody directed against intercellular adhesion molecule-1. *J Nucl Med.* 1998;39(4):723-8.
104. Peters AM, Danpure HJ, Osman S, Hawker RJ, Henderson BL, Hodgson HJ, et al. Clinical experience with 99mTc-hexamethylpropylene-amineoxime for labelling leucocytes and imaging inflammation. *Lancet.* 1986;2(8513):946-9.
105. Peters AM. The utility of [99mTc]HMPAO-leukocytes for imaging infection. *Semin Nucl Med.* 1994;24(2):110-27.
106. Langer O, Muller M. Methods to assess tissue-specific distribution and metabolism of drugs. *Curr Drug Metab.* 2004;5(6):463-81.
107. Audus KL, Knaub SR, Guillot FL, Schaeffer JM. The effect of protein binding on ivermectin uptake by bovine brain microvessel endothelial cells. *Vet Res Commun.* 1992;16(5):365-77.
108. Hyatt JM, McKinnon PS, Zimmer GS, Schentag JJ. The importance of pharmacokinetic/pharmacodynamic surrogate markers to outcome. Focus on antibacterial agents. *Clin Pharmacokinet.* 1995;28(2):143-60.
109. Lambert HP. Clinical significance of tissue penetration of antibiotics in the respiratory tract. *Scand J Infect Dis Suppl.* 1978(14):262-6.

110. Neu HC. Bacterial resistance to fluoroquinolones. *Rev Infect Dis.* 1988;10 Suppl 1:S57-63.
111. Jacobs RABJG. *Anti-infective chemtherapeutic and antibiotic agents.*: Lange Medical Publishing/McGraw-Hill; 2001.
112. Presant CA, Wolf W, Waluch V, Wiseman C, Kennedy P, Blayney D, et al. Association of Intratumoral Pharmacokinetics of Fluorouracil with Clinical-Response. *Lancet.* 1994;343(8907):1184-7.
113. Muller M, Pena AD, Derendorf H. Issues in pharmacokinetics and pharmacodynamics of anti-infective agents: Distribution in tissue. *Antimicrob Agents Ch.* 2004;48(5):1441-53.
114. Fischman AJ, Alpert NM, Babich JW, Rubin RH. The role of positron emission tomography in pharmacokinetic analysis. *Drug Metab Rev.* 1997;29(4):923-56.
115. Fischman AJ, Babich JW, Bonab AA, Alpert NM, Vincent J, Callahan RJ, et al. Pharmacokinetics of [18F]trovafloxacin in healthy human subjects studied with positron emission tomography. *Antimicrob Agents Chemother.* 1998;42(8):2048-54. PMID: 105732.
116. Greer T, Sturm R, Li L. Mass spectrometry imaging for drugs and metabolites. *J Proteomics.* 2011;74(12):2617-31. PMID: 3151478.
117. Solon EG, Schweitzer A, Stoeckli M, Prideaux B. Autoradiography, MALDI-MS, and SIMS-MS imaging in pharmaceutical discovery and development. *AAPS J.* 2010;12(1):11-26. PMID: 2811645.
118. Chughtai K, Heeren RM. Mass spectrometric imaging for biomedical tissue analysis. *Chem Rev.* 2010;110(5):3237-77. PMID: 2907483.

119. Prideaux B, Stoeckli M. Mass spectrometry imaging for drug distribution studies. *J Proteomics*. 2012;75(16):4999-5013.
120. Lappin G, Garner RC. Big physics, small doses: the use of AMS and PET in human microdosing of development drugs. *Nat Rev Drug Discov*. 2003;2(3):233-40.
121. Prideaux B, Dartois V, Staab D, Weiner DM, Goh A, Via LE, et al. High-sensitivity MALDI-MRM-MS imaging of moxifloxacin distribution in tuberculosis-infected rabbit lungs and granulomatous lesions. *Anal Chem*. 2011;83(6):2112-8. PMID: 3158846.
122. Ungerstedt U. Microdialysis--principles and applications for studies in animals and man. *J Intern Med*. 1991;230(4):365-73.
123. Elmquist WF, Sawchuk RJ. Application of microdialysis in pharmacokinetic studies. *Pharm Res*. 1997;14(3):267-88.
124. Wu Z, Wang D. [Application of sites-microdialysis technology in pharmacokinetic studies]. *Zhongguo Zhong Yao Za Zhi*. 2010;35(13):1765-8.
125. Ding PT, Xu H, Zheng JM. [Application of microdialysis in pharmacokinetic and drug metabolism studies]. *Yao Xue Xue Bao*. 2002;37(4):316-20.
126. Westerink BH, Damsma G, Rollema H, De Vries JB, Horn AS. Scope and limitations of in vivo brain dialysis: a comparison of its application to various neurotransmitter systems. *Life Sci*. 1987;41(15):1763-76.
127. Grimwood S, Hartig PR. Target site occupancy: emerging generalizations from clinical and preclinical studies. *Pharmacol Ther*. 2009;122(3):281-301.

128. Krishna R, Herman G, Wagner JA. Accelerating drug development using biomarkers: a case study with sitagliptin, a novel DPP4 inhibitor for type 2 diabetes. *AAPS J.* 2008;10(2):401-9. PMID: 2751391.
129. Simon GM, Niphakis MJ, Cravatt BF. Determining target engagement in living systems. *Nat Chem Biol.* 2013;9(4):200-5.
130. Ashworth S, Rabiner EA, Gunn RN, Plisson C, Wilson AA, Comley RA, et al. Evaluation of ¹¹C-GSK189254 as a novel radioligand for the H3 receptor in humans using PET. *J Nucl Med.* 2010;51(7):1021-9.
131. Ruth TJ, Bida GT, Wolf AP. Experimentally Determined Thick Target Yields for the N-14(P,Alpha)C-11 Reaction. *J Labelled Compd Rad.* 1981;18(1-2):247-8.
132. Bida GT, Ruth TJ, Wolf AP. Experimentally Determined Thick Target Yields for the N-14(P,Alpha)C-11 Reaction. *Radiochim Acta.* 1980;27(4):181-5.
133. Link JM, Krohn KA, Clark JC. Production of [¹¹C]CH₃I by single pass reaction of [¹¹C]CH₄ with I₂. *Nucl Med Biol.* 1997;24(1):93-7.
134. Jewett DM. A simple synthesis of [¹¹C]methyl triflate. *Int J Rad Appl Instrum A.* 1992;43(11):1383-5.
135. Nordberg A. PET imaging of amyloid in Alzheimer's disease. *Lancet Neurol.* 2004;3(9):519-27.
136. Zheng QH, Gardner TA, Raikwar S, Kao C, Stone KL, Martinez TD, et al. [¹¹C]Choline as a PET biomarker for assessment of prostate cancer tumor models. *Bioorg Med Chem.* 2004;12(11):2887-93.

137. Langer O, Nagren K, Dolle F, Lundkvist C, Sandell J, Swahn CG, et al. Precursor synthesis and radiolabelling of the dopamine D-2 receptor ligand [C-11]raclopride from [C-11]methyl triflate. *J Labelled Compd Rad.* 1999;42(12):1183-93.
138. Iwata R, Ido T, Takahashi T, Nakanishi H, Iida S. Optimization of [11C]HCN production and no-carrier-added [1-11C]amino acid synthesis. *Int J Rad Appl Instrum A.* 1987;38(2):97-102.
139. Roeda D, Tavitian B, Coulon C, David F, Dolle F, Fuseau C, et al. Synthesis of [C-11]RPR-72840A and its evaluation as a radioligand for the serotonin reuptake site in positron emission tomography. *Bioorgan Med Chem.* 1997;5(2):397-403.
140. Hooker JM, Reibel AT, Hill SM, Schueller MJ, Fowler JS. One-Pot, Direct Incorporation of [C-11]CO₂ into Carbamates. *Angew Chem Int Edit.* 2009;48(19):3482-5.
141. Nishijima K, Kuge Y, Seki K, Ohkura K, Motoki N, Nagatsu K, et al. A simplified and improved synthesis of [11C]phosgene with iron and iron (III) oxide. *Nucl Med Biol.* 2002;29(3):345-50.
142. Shields AF, Grierson JR, Dohmen BM, Machulla HJ, Styanoff JC, Lawhorn-Crews JM, et al. Imaging proliferation in vivo with [F-18]FLT and positron emission tomography. *Nat Med.* 1998;4(11):1334-6.
143. Lee E, Kamlet AS, Powers DC, Neumann CN, Boursalian GB, Furuya T, et al. A fluoride-derived electrophilic late-stage fluorination reagent for PET imaging. *Science.* 2011;334(6056):639-42. PMID: 3229297.
144. Scheindlin S. The fight against tuberculosis. *Mol Interv.* 2006;6(3):124-30.

145. Zumla A, George A, Sharma V, Herbert RH, Oxley A, Oliver M. The WHO 2014 Global tuberculosis report-further to go. *Lancet Glob Health*. 2015;3(1):e10-2.
146. Lienhardt C, Glaziou P, Uplekar M, Lonnroth K, Getahun H, Raviglione M. Global tuberculosis control: lessons learnt and future prospects. *Nat Rev Microbiol*. 2012;10(6):407-16.
147. Vashishtha VM. WHO Global Tuberculosis Control Report 2009: Tuberculosis elimination is a distant dream. *Indian Pediatr*. 2009;46(5):401-2.
148. Diagnostic Standards and Classification of Tuberculosis in Adults and Children. This official statement of the American Thoracic Society and the Centers for Disease Control and Prevention was adopted by the ATS Board of Directors, July 1999. This statement was endorsed by the Council of the Infectious Disease Society of America, September 1999. *Am J Respir Crit Care Med*. 2000;161(4 Pt 1):1376-95.
149. Jain A, Mondal R. Extensively drug-resistant tuberculosis: current challenges and threats. *FEMS Immunol Med Microbiol*. 2008;53(2):145-50.
150. Banerjee A, Dubnau E, Quemard A, Balasubramanian V, Um KS, Wilson T, et al. *inhA*, a gene encoding a target for isoniazid and ethionamide in *Mycobacterium tuberculosis*. *Science*. 1994;263(5144):227-30.
151. Tonge PJ, Rawat R, Whitty A. The isoniazid-NAD adduct is a slow, tight-binding inhibitor of *InhA*, the *Mycobacterium tuberculosis* enoyl reductase: Adduct affinity and drug resistance. *P Natl Acad Sci USA*. 2003;100(24):13881-6.
152. Zhang Y, Heym B, Allen B, Young D, Cole S. The catalase-peroxidase gene and isoniazid resistance of *Mycobacterium tuberculosis*. *Nature*. 1992;358(6387):591-3.

153. Johnsson K, King DS, Schultz PG. Studies on the Mechanism of Action of Isoniazid and Ethionamide in the Chemotherapy of Tuberculosis. *J Am Chem Soc.* 1995;117(17):5009-10.
154. Basso LA, Zheng RJ, Blanchard JS. Kinetics of inactivation of WT and C243S mutant of *Mycobacterium tuberculosis* enoyl reductase by activated isoniazid. *J Am Chem Soc.* 1996;118(45):11301-2.
155. Heym B, Honore N, Truffot-Pernot C, Banerjee A, Schurra C, Jacobs WR, Jr., et al. Implications of multidrug resistance for the future of short-course chemotherapy of tuberculosis: a molecular study. *Lancet.* 1994;344(8918):293-8.
156. Stoeckle MY, Guan L, Riegler N, Weitzman I, Kreiswirth B, Kornblum J, et al. Catalase-peroxidase gene sequences in isoniazid-sensitive and -resistant strains of *Mycobacterium tuberculosis* from New York City. *J Infect Dis.* 1993;168(4):1063-5.
157. Musser JM, Kapur V, Williams DL, Kreiswirth BN, van Soolingen D, van Embden JD. Characterization of the catalase-peroxidase gene (*katG*) and *inhA* locus in isoniazid-resistant and -susceptible strains of *Mycobacterium tuberculosis* by automated DNA sequencing: restricted array of mutations associated with drug resistance. *J Infect Dis.* 1996;173(1):196-202.
158. Kaplan G, Post FA, Moreira AL, Wainwright H, Kreiswirth BN, Tanverdi M, et al. *Mycobacterium tuberculosis* growth at the cavity surface: a microenvironment with failed immunity. *Infect Immun.* 2003;71(12):7099-108. PMID: 308931.
159. Sullivan TJ, Truglio JJ, Boyne ME, Novichenok P, Zhang X, Stratton CF, et al. High affinity *InhA* inhibitors with activity against drug-resistant strains of *Mycobacterium tuberculosis*. *ACS Chem Biol.* 2006;1(1):43-53.

160. Lu H, England K, Ende CA, Truglio JJ, Luckner S, Reddy BG, et al. Slow-Onset Inhibition of the FabI Enoyl Reductase from *Francisella tularensis*: Residence Time and in Vivo Activity. *Acs Chem Biol*. 2009;4(3):221-31.
161. Luckner SR, Liu N, am Ende CW, Tonge PJ, Kisker C. A slow, tight binding inhibitor of InhA, the enoyl-acyl carrier protein reductase from *Mycobacterium tuberculosis*. *J Biol Chem*. 2010;285(19):14330-7. PMID: 2863195.
162. Vilcheze C, Wang F, Arai M, Hazbon MH, Colangeli R, Kremer L, et al. Transfer of a point mutation in *Mycobacterium tuberculosis inhA* resolves the target of isoniazid. *Nat Med*. 2006;12(9):1027-9.
163. Ward WH, Holdgate GA, Rowsell S, McLean EG, Paupit RA, Clayton E, et al. Kinetic and structural characteristics of the inhibition of enoyl (acyl carrier protein) reductase by triclosan. *Biochemistry*. 1999;38(38):12514-25.
164. Pan P, Knudson SE, Bommineni GR, Li HJ, Lai CT, Liu N, et al. Time-Dependent Diaryl Ether Inhibitors of InhA: Structure-Activity Relationship Studies of Enzyme Inhibition, Antibacterial Activity, and in vivo Efficacy. *ChemMedChem*. 2014.
165. Pasipanodya JG, Srivastava S, Gumbo T. Meta-Analysis of Clinical Studies Supports the Pharmacokinetic Variability Hypothesis for Acquired Drug Resistance and Failure of Antituberculosis Therapy. *Clin Infect Dis*. 2012;55(2):169-77.
166. Fowler JS, Volkow ND, Wang GJ, Ding YS, Dewey SL. PET and drug research and development. *J Nucl Med*. 1999;40(7):1154-63.
167. Hodgson HH. The Sandmeyer Reaction. *Chemical Reviews*. 1947;40(2):251-77.
168. Kettenbach K, Schieferstein H, Ross TL. F-18-Labeling Using Click Cycloadditions. *Biomed Res Int*. 2014.

169. England K, Ende CA, Lu H, Sullivan TJ, Marlenee NL, Bowen RA, et al. Substituted diphenyl ethers as a broad-spectrum platform for the development of chemotherapeutics for the treatment of tularaemia. *J Antimicrob Chemoth.* 2009;64(5):1052-61.
170. Pfaller MA, Jones RN, Doern GV, Sader HS, Kugler KC, Beach ML, et al. Survey of blood stream infections attributable to Gram-positive cocci: Frequency of occurrence and antimicrobial susceptibility of isolates collected in 1997 in the United States, Canada, and Latin America from the SENTRY Antimicrobial Surveillance Program. *Diagn Micr Infec Dis.* 1999;33(4):283-97.
171. Diekema DJ, Pfaller MA, Schmitz FJ, Smayevsky J, Bell J, Jones RN, et al. Survey of infections due to Staphylococcus species: Frequency of occurrence and antimicrobial susceptibility of isolates collected in the United States, Canada, Latin America, Europe, and the Western Pacific region for the SENTRY Antimicrobial Surveillance Program, 1997-1999. *Clin Infect Dis.* 2001;32:S114-S32.
172. Peacock SJ, de Silva I, Lowy FD. What determines nasal carriage of Staphylococcus aureus? *Trends Microbiol.* 2001;9(12):605-10.
173. Barber M. Methicillin-resistant staphylococci. *J Clin Pathol.* 1961;14:385-93. PMID: 480239.
174. Walsh C. Microbiology - Deconstructing vancomycin. *Science.* 1999;284(5413):442-3.
175. Sievert DM, Rudrik JT, Patel JB, McDonald LC, Wilkins MJ, Hageman JC. Vancomycin-resistant staphylococcus aureus in the United States, 2002-2006. *Clin Infect Dis.* 2008;46(5):668-74.

176. Payne DJ, Miller WH, Berry V, Brosky J, Burgess WJ, Chen E, et al. Discovery of a novel and potent class of FabI-directed antibacterial agents. *Antimicrob Agents Chemother.* 2002;46(10):3118-24. PMID: 128775.
177. Lu H, Tonge PJ. Inhibitors of FabI, an enzyme drug target in the bacterial fatty acid biosynthesis pathway. *Accounts Chem Res.* 2008;41(1):11-20.
178. Bamber AI, Neal TJ. An assessment of triclosan susceptibility in methicillin-resistant and methicillin-sensitive *Staphylococcus aureus*. *J Hosp Infect.* 1999;41(2):107-9.
179. Park HS, Yoon YM, Jung SJ, Kim CM, Kim JM, Kwak JH. Antistaphylococcal activities of CG400549, a new bacterial enoyl-acyl carrier protein reductase (FabI) inhibitor. *J Antimicrob Chemother.* 2007;60(3):568-74.
180. Escaich S, Prouvensier L, Saccomani M, Durant L, Oxoby M, Gerusz V, et al. The MUT056399 Inhibitor of FabI Is a New Antistaphylococcal Compound. *Antimicrob Agents Ch.* 2011;55(10):4692-7.
181. Tsuji BT, Harigaya Y, Lesse AJ, Forrest A, Ngo D. Activity of AFN-1252, a novel FabI inhibitor, against *Staphylococcus aureus* in an in vitro pharmacodynamic model simulating human pharmacokinetics. *J Chemotherapy.* 2013;25(1):32-5.
182. Chang A, Schiebel J, Yu W, Bommineni GR, Pan P, Baxter MV, et al. Rational optimization of drug-target residence time: insights from inhibitor binding to the *Staphylococcus aureus* FabI enzyme-product complex. *Biochemistry.* 2013;52(24):4217-28.
183. Dohyun Kim DA, Sung Won Kim, Jacob Hooker, Richard A. Ferrieri inventor Brookhaven Science Associates, LLC, assignee. C-11 Cyanide Production System. 2013.

184. Liu L, Xu YW, Shea C, Fowler JS, Hooker JM, Tonge PJ. Radiosynthesis and Bioimaging of the Tuberculosis Chemotherapeutics Isoniazid, Rifampicin and Pyrazinamide in Baboons. *J Med Chem*. 2010;53(7):2882-91.
185. Welling MM, Alberto R. Performance of a (99m)Tc-labelled 1-thio-beta-D-glucose 2,3,4,6-tetra-acetate analogue in the detection of infections and tumours in mice: a comparison with [(18)F]FDG. *Nucl Med Commun*. 2010;31(3):239-48.
186. Heath RJ. Bacterial fatty-acid biosynthesis: an antibacterial drug target waiting to be exploited. *Drug Discov Today*. 2001;6(14):715-.
187. am Ende CW, Knudson SE, Liu N, Childs J, Sullivan TJ, Boyne M, et al. Synthesis and in vitro antimycobacterial activity of B-ring modified diaryl ether InhA inhibitors. *Bioorg Med Chem Lett*. 2008;18(10):3029-33. PMID: 2491328.
188. Nutt R, Vento LJ, Ridinger MHT. In vivo molecular imaging biomarkers: Clinical pharmacology's new "PET"? *Clin Pharmacol Ther*. 2007;81(6):792-5.
189. Calafat AM, Ye X, Wong LY, Reidy JA, Needham LL. Urinary concentrations of triclosan in the U.S. population: 2003-2004. *Environ Health Perspect*. 2008;116(3):303-7. PMID: 2265044.
190. Wang LQ, Falany CN, James MO. Triclosan as a substrate and inhibitor of 3'-phosphoadenosine-5'-phosphosulfate-sulfotransferase and UDP-glucuronosyl transferase in human liver fractions. *Drug Metab Dispos*. 2004;32(10):1162-9.
191. Queckenberg C, Meins J, Wachall B, Doroshenko O, Tomalik-Scharte D, Bastian B, et al. Absorption, pharmacokinetics, and safety of triclosan after dermal administration. *Antimicrob Agents Chemother*. 2010;54(1):570-2. PMID: 2798550.

192. Sandborgh-Englund G, Adolfsson-Erici M, Odham G, Ekstrand J. Pharmacokinetics of triclosan following oral ingestion in humans. *J Toxicol Environ Health A*. 2006;69(20):1861-73.
193. Banevicius MA, Kaplan N, Hafkin B, Nicolau DP. Pharmacokinetics, pharmacodynamics and efficacy of novel FabI inhibitor AFN-1252 against MSSA and MRSA in the murine thigh infection model. *J Chemother*. 2013;25(1):26-31. PMID: 3558988.
194. Mckellar OA, Bruni SFS, Jones DG. Pharmacokinetic/pharmacodynamic relationships of antimicrobial drugs used in veterinary medicine. *J Vet Pharmacol Ther*. 2004;27(6):503-14.
195. Barre J, Didey F, Delion F, Tillement JP. Problems in therapeutic drug monitoring: free drug level monitoring. *Ther Drug Monit*. 1988;10(2):133-43.
196. Signore A, Glaudemans AW. The molecular imaging approach to image infections and inflammation by nuclear medicine techniques. *Ann Nucl Med*. 2011;25(10):681-700.
197. Zumla A, George A, Sharma V, Herbert N, Baroness Masham of I. WHO's 2013 global report on tuberculosis: successes, threats, and opportunities. *Lancet*. 2013;382(9907):1765-7.
198. Lillebaek T, Dirksen A, Baess I, Strunge B, Thomsen VO, Andersen AB. Molecular evidence of endogenous reactivation of *Mycobacterium tuberculosis* after 33 years of latent infection. *J Infect Dis*. 2002;185(3):401-4.
199. Bass JB, Jr., Farer LS, Hopewell PC, O'Brien R, Jacobs RF, Ruben F, et al. Treatment of tuberculosis and tuberculosis infection in adults and children. *American*

Thoracic Society and The Centers for Disease Control and Prevention. *Am J Respir Crit Care Med.* 1994;149(5):1359-74.

200. Treatment of Tuberculosis and Tuberculosis Infection in Adults and Children. *American Review of Respiratory Disease.* 1986;134(2):355-63.

201. Jenne JW, Beggs WH. Correlation of in-Vitro and in-Vivo Kinetics with Clinical Use of Isoniazid, Ethambutol, and Rifampin. *American Review of Respiratory Disease.* 1973;107(6):1013-21.

202. Ruslami R, Ganiem AR, Dian S, Apriani L, Achmad TH, van der Ven AJ, et al. Intensified regimen containing rifampicin and moxifloxacin for tuberculous meningitis: an open-label, randomised controlled phase 2 trial. *Lancet Infect Dis.* 2013;13(1):27-35.

203. McKenzie C. Antibiotic dosing in critical illness. *J Antimicrob Chemoth.* 2011;66:ii25-ii31.

204. Weinstein EA, Liu L, Ordonez AA, Wang H, Hooker JM, Tonge PJ, et al. Noninvasive determination of 2-[18F]-fluoroisonicotinic acid hydrazide pharmacokinetics by positron emission tomography in *Mycobacterium tuberculosis*-infected mice. *Antimicrob Agents Chemother.* 2012;56(12):6284-90. PMID: 3497161.

205. Chang KC, Leung CC, Yew WW, Leung ECC, Leung WM, Tam CM, et al. Pyrazinamide May Improve Fluoroquinolone-Based Treatment of Multidrug-Resistant Tuberculosis. *Antimicrob Agents Ch.* 2012;56(11):5465-75.

206. Diacon AH, Pym A, Grobusch MP, de los Rios JM, Gotuzzo E, Vasilyeva I, et al. Multidrug-resistant tuberculosis and culture conversion with bedaquiline. *N Engl J Med.* 2014;371(8):723-32.

207. Mitchison DA. The action of antituberculosis drugs in short-course chemotherapy. *Tubercle*. 1985;66(3):219-25.
208. Zhang Y, Mitchison D. The curious characteristics of pyrazinamide: a review. *Int J Tuberc Lung Dis*. 2003;7(1):6-21.
209. Gopal P, Dick T. Reactive dirty fragments: implications for tuberculosis drug discovery. *Curr Opin Microbiol*. 2014;21:7-12.
210. Konno K, Feldmann FM, McDermott W. Pyrazinamide susceptibility and amidase activity of tubercle bacilli. *Am Rev Respir Dis*. 1967;95(3):461-9.
211. Scorpio A, Zhang Y. Mutations in *pncA*, a gene encoding pyrazinamidase/nicotinamidase, cause resistance to the antituberculous drug pyrazinamide in tubercle bacillus. *Nat Med*. 1996;2(6):662-7.
212. Scorpio A, Lindholm-Levy P, Heifets L, Gilman R, Siddiqi S, Cynamon M, et al. Characterization of *pncA* mutations in pyrazinamide-resistant *Mycobacterium tuberculosis*. *Antimicrob Agents Chemother*. 1997;41(3):540-3. PMID: 163747.
213. Zhang Y, Wade MM, Scorpio A, Zhang H, Sun Z. Mode of action of pyrazinamide: disruption of *Mycobacterium tuberculosis* membrane transport and energetics by pyrazinoic acid. *J Antimicrob Chemother*. 2003;52(5):790-5.
214. Zimhony O, Cox JS, Welch JT, Vilcheze C, Jacobs WR. Pyrazinamide inhibits the eukaryotic-like fatty acid synthetase I (FASI) of *Mycobacterium tuberculosis*. *Nature Medicine*. 2000;6(9):1043-7.
215. Baughn AD, Deng J, Vilcheze C, Riestra A, Welch JT, Jacobs WR, Jr., et al. Mutually exclusive genotypes for pyrazinamide and 5-chloropyrazinamide resistance

- reveal a potential resistance-proofing strategy. *Antimicrob Agents Chemother.* 2010;54(12):5323-8. PMID: 2981270.
216. Ahmad Z, Tyagi S, Minkowsk A, Almeida D, Nuermberger EL, Peck KM, et al. Activity of 5-chloro-pyrazinamide in mice infected with *Mycobacterium tuberculosis* or *Mycobacterium bovis*. *Indian J Med Res.* 2012;136(5):808-14. PMID: 3573602.
217. Jordis SVBaU. Synthetic studies towards the antiviral pyrazine derivative T-705. 13th Electronic Conference on Synthetic Organic Chemistry. 2009.
218. Moorthy JN, Singhal N. Facile and highly selective conversion of nitriles to amides via indirect acid-catalyzed hydration using TFA or AcOH-H₂SO₄. *J Org Chem.* 2005;70(5):1926-9.
219. Alan R. Katritzky BP, Laszlo Urogdi. Efficient Conversion of Nitriles to Amides with Basic Hydrogen Peroxide in Dimethyl Sulfoxide. *Synthesis.* 1989;12:949-50.
220. Zhang Y, Scorpio A, Nikaido H, Sun Z. Role of acid pH and deficient efflux of pyrazinoic acid in unique susceptibility of *Mycobacterium tuberculosis* to pyrazinamide. *J Bacteriol.* 1999;181(7):2044-9. PMID: 93615.
221. Wayne LG. Simple pyrazinamidase and urease tests for routine identification of mycobacteria. *Am Rev Respir Dis.* 1974;109(1):147-51.
222. Singh P, Wesley C, Jadaun GP, Malonia SK, Das R, Upadhyay P, et al. Comparative evaluation of Lowenstein-Jensen proportion method, BacT/ALERT 3D system, and enzymatic pyrazinamidase assay for pyrazinamide susceptibility testing of *Mycobacterium tuberculosis*. *J Clin Microbiol.* 2007;45(1):76-80. PMID: 1828947.

223. Harper J, Skerry C, Davis SL, Tasneen R, Weir M, Kramnik I, et al. Mouse model of necrotic tuberculosis granulomas develops hypoxic lesions. *J Infect Dis*. 2012;205(4):595-602. PMID: 3266133.
224. Pan H, Yan BS, Rojas M, Shebzukhov YV, Zhou H, Kobzik L, et al. *Ipr1* gene mediates innate immunity to tuberculosis. *Nature*. 2005;434(7034):767-72. PMID: 1388092.
225. Mc DW, Tompsett R. Activation of pyrazinamide and nicotinamide in acidic environments in vitro. *Am Rev Tuberc*. 1954;70(4):748-54.
226. Shi W, Zhang X, Jiang X, Yuan H, Lee JS, Barry CE, 3rd, et al. Pyrazinamide inhibits trans-translation in *Mycobacterium tuberculosis*. *Science*. 2011;333(6049):1630-2. PMID: 3502614.
227. Zimhony O, Cox JS, Welch JT, Vilcheze C, Jacobs WR, Jr. Pyrazinamide inhibits the eukaryotic-like fatty acid synthetase I (FASI) of *Mycobacterium tuberculosis*. *Nat Med*. 2000;6(9):1043-7.
228. Boshoff HI, Mizrahi V, Barry CE, 3rd. Effects of pyrazinamide on fatty acid synthesis by whole mycobacterial cells and purified fatty acid synthase I. *J Bacteriol*. 2002;184(8):2167-72. PMID: 134955.
229. Dawson R, et al. P-931a-Pyrazinamide Increases the Early Bacteriocidal Activity of TMC207 and PA-824 in Patients with newly Diagnosed, Smear-positive Pulmonary Tuberculosis. *ICAAC*. 2011.
230. Laura E. Via RS, Danielle M. Weiner, Matthew D. Zimmerman, Brendan Prideaux, Scott M. Irwin, Eddie Lyon, Paul O'Brien, Pooja Gopal, Seokyoung Eum, Myungsun Lee, Jean-Philippe Lanoix, Noton K. Dutta, TaeSun Shim, Jeong Su Cho,

Wooshik Kim, Petros C. Karakousis, Anne Lenaerts, Eric Nuermberger, Clifton E. Barry, and Véronique Dartois. Host-Mediated Bioactivation of Pyrazinamide: Implications for Efficacy, Resistance, and Therapeutic Alternatives. *ACS Infect Dis.*, 2015.

231. Schmidt S, Banks R, Kumar V, Rand KH, Derendorf H. Clinical microdialysis in skin and soft tissues: an update. *J Clin Pharmacol.* 2008;48(3):351-64.

232. Cynamon MH, Speirs RJ, Welch JT. In vitro antimycobacterial activity of 5-chloropyrazinamide. *Antimicrob Agents Chemother.* 1998;42(2):462-3. PMID: 105437.

233. Shen CT, Qiu ZL, Han TT, Luo QY. Performance of 18F-fluoride PET or PET/CT for the detection of bone metastases: a meta-analysis. *Clin Nucl Med.* 2015;40(2):103-10.

234. Tiple DN, Zoghbi SS, Liow JS, Green MV, Seidel J, Ichise M, et al. PET imaging of brain 5-HT_{1A} receptors in rat in vivo with 18F-FCWAY and improvement by successful inhibition of radioligand defluorination with miconazole. *J Nucl Med.* 2006;47(2):345-53.

235. Signore A, Mather SJ, Piaggio G, Malviya G, Dierckx RA. Molecular imaging of inflammation/infection: nuclear medicine and optical imaging agents and methods. *Chem Rev.* 2010;110(5):3112-45.

236. del Rosal T, Goycochea WA, Mendez-Echevarria A, Garcia-Fernandez de Villalta M, Baquero-Artigao F, Coronado M, et al. (1)(8)F-FDG PET/CT in the diagnosis of occult bacterial infections in children. *Eur J Pediatr.* 2013;172(8):1111-5.

237. Simons KS, Pickkers P, Bleeker-Rovers CP, Oyen WJ, van der Hoeven JG. F-18-fluorodeoxyglucose positron emission tomography combined with CT in critically ill

- patients with suspected infection. *Intensive Care Med.* 2010;36(3):504-11. PMID: 2820225.
238. Heysell SK, Thomas TA, Sifri CD, Rehm PK, Houpt ER. 18-Fluorodeoxyglucose positron emission tomography for tuberculosis diagnosis and management: a case series. *BMC Pulm Med.* 2013;13:14. PMID: 3637578.
239. Seldes RM, Winiarsky R, Jordan LC, Baldini T, Brause B, Zodda F, et al. Liquid gentamicin in bone cement: a laboratory study of a potentially more cost-effective cement spacer. *J Bone Joint Surg Am.* 2005;87(2):268-72.
240. Martinez V, Castilla-Lievre MA, Guillet-Caruba C, Grenier G, Fior R, Desarnaud S, et al. (18)F-FDG PET/CT in tuberculosis: an early non-invasive marker of therapeutic response. *Int J Tuberc Lung Dis.* 2012;16(9):1180-5.
241. Wegkamp A, van Oorschot W, de Vos WM, Smid EJ. Characterization of the role of para-aminobenzoic acid biosynthesis in folate production by *Lactococcus lactis*. *Appl Environ Microbiol.* 2007;73(8):2673-81. PMID: 1855612.
242. Hitchings GH. Functions of Tetrahydrofolate and the Role of Dihydrofolate Reductase in Cellular Metabolism. Inhibition of Folate Metabolism in Chemotherapy. 1983;64:11-23.
243. Green JM, Merkel WK, Nichols BP. Characterization and sequence of *Escherichia coli* pabC, the gene encoding aminodeoxychorismate lyase, a pyridoxal phosphate-containing enzyme. *J Bacteriol.* 1992;174(16):5317-23. PMID: 206368.
244. Fox W, Ellard GA, Mitchison DA. Studies on the treatment of tuberculosis undertaken by the British Medical Research Council tuberculosis units, 1946-1986, with relevant subsequent publications. *Int J Tuberc Lung Dis.* 1999;3(10 Suppl 2):S231-79.

245. Chakraborty S, Gruber T, Barry CE, Boshoff HI, Rhee KY. Para-Aminosalicylic Acid Acts as an Alternative Substrate of Folate Metabolism in Mycobacterium tuberculosis. *Science*. 2013;339(6115):88-91.
246. Zheng J, Rubin EJ, Bifani P, Mathys V, Lim V, Au M, et al. para-Aminosalicylic Acid Is a Prodrug Targeting Dihydrofolate Reductase in Mycobacterium tuberculosis. *Journal of Biological Chemistry*. 2013;288(32):23447-56.
247. Fernley RT, Iliades P, Macreadie I. A rapid assay for dihydropteroate synthase activity suitable for identification of inhibitors. *Anal Biochem*. 2007;360(2):227-34.
248. Todar K. *Todar's online textbook of bacteriology*.